Exploring strategies to tune the structure and properties of metallic glasses

By

Vrishank R. Jambur

A dissertation submitted in partial fulfillment of

the requirements of the degree of

Doctor of Philosophy

(Materials Science and Engineering)

at the

UNIVERSITY OF WISCONSIN – MADISON

2023

Date of final oral examination: 08/07/2023

This dissertation is approved by the following members of the Final Oral Committee:

Izabela Szlufarska, Professor, Materials Science and Engineering
Paul Voyles, Professor, Materials Science and Engineering
John Perepezko, Professor, Materials Science and Engineering
Dane Morgan, Professor, Materials Science and Engineering
Bu Wang, Assistant Professor, Civil and Environmental Engineering

Abstract

Metallic glasses have garnered significant attention due to their unique properties, offering promising applications in various fields. However, their widespread use has been limited by factors such as a limited composition space with good glass forming ability and poor ductility. In order to optimize their performance, understanding the intricate relationships between their structure, mechanical properties, and processing methods is of the highest importance. This thesis delves into different strategies to fine-tune the structure and properties of metallic glasses through the use of minor alloying and vapor deposition techniques. In the third chapter, we focus on a novel approach to controlling the properties of thin film metallic glasses through ion beam assisted deposition. Our results demonstrate the potential of ion beam-assisted deposition as a viable and promising method for engineering metallic glasses with increased hardness and kinetic stability. We also highlight the key role of surface mobility in allowing glasses to access more stable states through the vapor deposition processes. Expanding the scope of our study, the fourth chapter explores the application of vapor deposition to oxide glasses. We investigate how vapor deposition can be effectively utilized to control the properties of amorphous SiO_2 films, providing valuable insights into the structure-mechanical property relationships in this industrially important glass with several anomalous thermo-mechanical behaviors. In the fifth chapter, we investigate the influence of minor alloying on the mechanical properties of metallic glasses. Contrary to conventional approaches that focus solely on topological ordering, our research reveals that chemical bonding plays an equally important role in determining the mechanical behavior of metallic glasses. By examining the impact of various minor alloying elements on mechanical properties, we gain a deeper understanding of the interplay between chemical and topological factors in controlling the mechanical properties of glasses. Continuing the exploration of structure – mechanical property correlations, the last chapter delves into factors determining the plasticity of metallic glasses, where we find that plastic deformation in metallic glasses is influenced by several structural features that span across different length scales. Through these interconnected chapters, this thesis presents a comprehensive understanding of diverse strategies to tune the structure and properties of metallic glasses. This work paves the way for further advancements in the design and development of metallic glasses and other glassy materials with tailored properties, opening up new avenues for exciting applications in the future.

Acknowledgements

My time at UW Madison has not only helped me develop my skills as a researcher but also facilitated my personal growth, and I am immensely thankful to all the people who have been part of my journey over the past five years. Firstly, I would like to express my deepest gratitude to my advisor, Prof. Izabela Szlufarska, for providing me with the opportunity to travel halfway across the world to attend this prestigious university and learn so much along the way. Prof. Szlufarska has not only been an exceptional research mentor but also a very understanding and constant source of support and motivation throughout all the ups and downs of my Ph.D. It was Prof. Szlufarska's guidance that helped me secure an internship as well as my first job in the industry, and for that, I will always be thankful. I feel truly lucky to have had Prof. Szlufarska as my Ph.D. advisor.

Next, I would like to express my heartfelt gratitude to the members of my dissertation committee, with whom I have had the privilege to interact and collaborate. Specifically, I extend my thanks to Prof. Paul Voyles and Prof. John Perepezko, who have been valuable collaborators on various projects and generously allowed me to utilize the facilities in their labs. Their patient guidance and support were instrumental in advancing my thesis. Additionally, I am immensely thankful to Prof. Dane Morgan for engaging in several thought-provoking discussions and providing valuable advice during group meetings. His insights spanned beyond research and encompassed communication and presentation skills, which have helped in my professional growth. Furthermore, I wish to convey my appreciation to Prof. Bu Wang for the enriching discussions and valuable inputs, particularly pertaining to my work on amorphous silica.

I would also like to extend my heartfelt gratitude to all my colleagues at CMG and the UW MRSEC for their constant availability and willingness to help, which created a friendly and positive atmosphere to work in. In particular, I am thankful to Dr. Chaiyapat Tangpatjaroen, who served as my mentor during the initial days of my Ph.D. and trained me with several valuable skills for my research. Additionally, I am immensely grateful to Lane Schultz, Dr. Ajay Annamareddy, Dr. Jianqi Xi, Dr. Sachin Muley, Shuguang Wei, Carter Francis, and Dr. Zijian Wang for always being ready to lend a helping hand. I am also very grateful to the staff at NIAC, especially Dr. Julie Morasch, for their invaluable assistance in training me on how to use the instruments for various characterization methods and their willingness to assist me whenever I encountered challenges during my experiments.

Next, I would like to express my gratitude to the friends I made along the way, who helped make Madison feel like home. I am thankful to Hemant, Dipul, Mohan, Deepankar, Ankur, Saketh, Sabari, Veda, Namita, and Siddanth for their companionship during my time in Madison. I would also like to extend my heartfelt gratitude to my friends Shashank, Aditya, and Mriganabh, who have been nothing short of a second family away from home. I am thankful to have them by my side, and I will always cherish the bond we have.

Finally, I would like to express my deepest gratitude to my family, whose unwavering love and support have been the foundation of my journey. My aunt Smitha and uncle Shiva have treated me like a son since the day I landed in the USA for my Ph.D. To my wife Nandini, I owe gratitude for standing by my side and providing unwavering support through the most challenging phase of my Ph.D. I am blessed to have you in my life. To my parents, grandparents, and sister, I am most grateful for the immeasurable love and faith you have shown in me. You have always believed in my potential, encouraged me to be ambitious, and supported every decision I have made in my life. Your guidance and unwavering support have been the driving force behind my achievements.

Table of Contents

1. Introduction

Glasses have been an essential part of human civilization since ancient times, presenting a diverse array of applications across various industries. The unique properties of glasses arise from their amorphous structure, achieved through the process of vitrification, where a liquid is rapidly cooled to suppress kinetics and prevent crystallization. Characterizing the amorphous structure of glasses and its direct influence on their properties has long been a longstanding challenge in materials science. However, the knowledge of these structure-property correlations is critical when it comes to designing compositions and developing processing techniques for any material.

This thesis embarks on an in-depth exploration of the structure-property-processing relationships, mainly focusing on a specific type of glass - metallic glass (MG). First discovered in the 1960s [1], MGs have garnered significant attention owing to their exceptional mechanical properties (Fig.1.1) and processing advantages, such as high specific strength, elevated elastic limits, and thermoplastic forming capabilities [2,3]. Despite their potential, widespread utilization of MGs remains limited, primarily due to challenges associated with their glass-forming ability [4] for producing bulk glasses and their inherent brittleness [5].

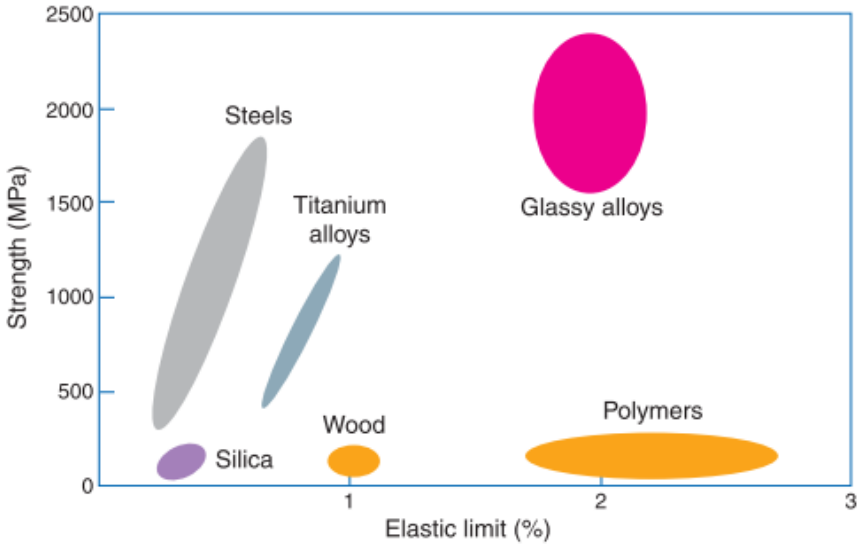

Fig. 1.1 Amorphous metallic alloys or metallic glasses have a unique combination of high strength and elasticity. Image taken from [2].

Unlike organic and most other inorganic glasses, MGs are composed of highly mobile atoms, necessitating extraordinarily high cooling rates to attain the glassy state. This requirement restricts the size of components that can be made using metallic glasses, with only a narrow range of compositions exhibiting sufficiently slow kinetics to form glass structures under reasonable cooling rates [4]. Nevertheless, one promising avenue for exploring the full composition space and capitalizing on the unique properties of amorphous structures is the application of metallic glass films and coatings [6]. The process of Physical Vapor Deposition (PVD) offers an excellent platform to synthesize films and coatings, allowing fine-tuning of their structures and properties through various controllable parameters.

Another crucial aspect impeding the broader application of metallic glasses lies in their poor ductility, due to their deformation mechanism involving localized flow in shear bands [5]. To overcome this limitation, a thorough understanding of the influence of the structure on the deformation behavior is necessary to formulate strategies for enhancing ductility. Although metallic glasses lack long-range order, they do possess distinguishable features at the scale of the first few neighboring atomic shells, characterized as short-range order (SRO) and medium-range order (MRO), which have a strong influence on their properties [7]. In the context of multi-component metallic glass systems, the chemical interaction between different elements must also be considered while establishing structure-property correlations [8,9].

An alternative perspective on metallic glass structures and their properties can be viewed through the lens of the potential energy landscape (PEL) [10,11]. Each metallic glass composition represents a metastable state corresponding to a basin in a complex PEL comprising numerous peaks and basins (Fig.1.2). These basins represent distinct metastable configurations of atoms, with the depth signifying the thermodynamic stability of the state. The height of the peaks represents the kinetic barrier to transition from one basin to another, providing valuable insights into the material's behavior during processing. The PEL offers a framework to explore various structural configurations of metallic glasses, enabling the tailoring of specific properties.

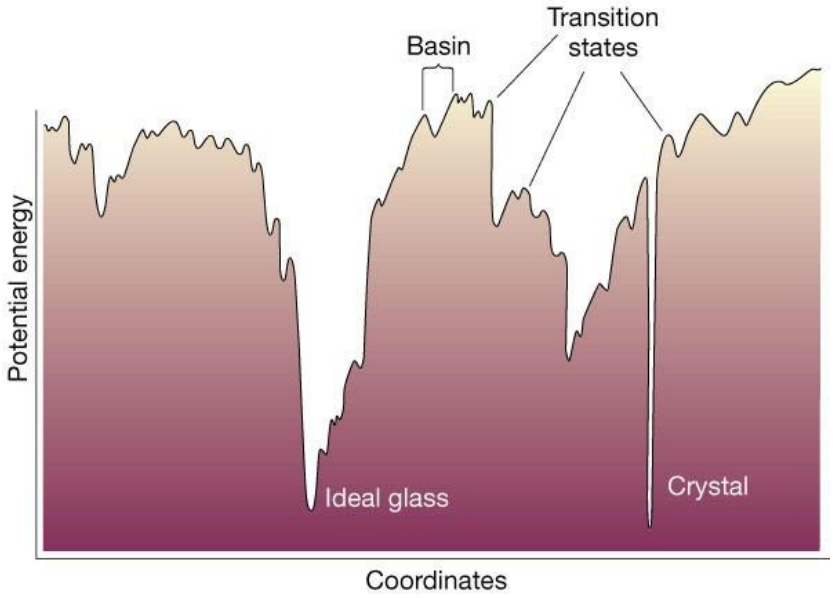

Fig.1.2 Schematic figure of the potential energy landscape taken from [12].

In this thesis, the third and the fourth chapters focus on harnessing the potential of physical vapor deposition to explore the PEL of metallic glasses and amorphous SiO_2, demonstrating how processing parameters can be manipulated to access states with desirable properties. The fifth chapter delves into the intricate relationship between the structure and mechanical properties of metallic glasses, particularly in the context of minor alloying. Finally, the last chapter examines how processing techniques and minor alloying can be effectively employed to address the challenge of poor ductility in metallic glasses.

2. Experimental and simulation techniques

2.1 Physical Vapor Deposition

Physical vapor deposition (PVD) processes involve the deposition of thin films by vaporizing material from a solid or liquid source, transporting it through a vacuum or low-pressure gas environment to a substrate, where it condenses. PVD can create films with thicknesses ranging from a few nanometers to several microns, allowing for multilayer coatings, graded compositions, and freestanding structures on substrates of various sizes and shapes. PVD methods include vacuum deposition, sputter deposition, arc vapor deposition, and ion plating [13]. The amorphous SiO_2 films studied in chapter 4 were prepared by electron beam evaporation which is a vacuum deposition technique. Vacuum deposition achieves vaporization of the target with no gas collision and is often used for optical coatings, barrier films, conducting layers, and protective coatings. On the other hand, sputter deposition involves non-thermal vaporization by ion bombardment, allowing for various material sources and applications such as semiconductor metallization, glass coatings, and magnetic films.

One type of sputter deposition technique is DC magnetron sputtering. Here, a voltage is applied to a cathode made of the target material to generate a glow discharge in the low pressure gas environment. This discharge causes the gas ions to accelerate towards the cathode with high energy, leading to collisions with the cathode surface. These collisions dislodge atoms or molecules from the cathode, resulting in the ejection of material in the form of sputtered particles. These particles then travel through the vacuum chamber and condense on the substrate, forming a thin film. The magnetron is used to enhance the sputtering process. It’s magnetic field traps electrons near the cathode's surface, creating a dense plasma with higher ionization efficiency and increased sputtering rates. This allows for operation at lower gas pressures, improving control over film characteristics [14].

Ion beam assisted deposition (IBAD) is a PVD technique that involves the bombardment of the film during growth to modify its properties. IBAD is generally carried out in conjunction with vacuum deposition techniques where low pressures are conducive to the propagation of the ion beam towards the substrate [15]. However, we have used a DC magnetron sputtering system that has been retrofitted with a single

beam ion source from Scion Plasma that is capable of operating over a wide range of pressures. This setup was successfully used to synthesize the metallic glass films studied in chapter 3.

The DC magnetron sputtering system used in this work was designed and assembled by Dr. Sachin Muley and the ion source was installed by John Sunderland, from Prof, Paul Voyles' group.

2.2 Nanoindentation

The work in this thesis involved the use of a variety of techniques for structural, mechanical, and compositional characterization of materials including nanoindentation, atomic force microscopy (AFM), X-ray diffraction (XRD), scanning electron microscopy (SEM), energy dispersive spectroscopy (EDS), and X-ray photoelectron spectroscopy (XPS). Of these techniques, nanoindentation has been used most extensively. The following is a brief summary of the basic principles and applications of this versatile technique.

Nanoindentation is a technique used to evaluate mechanical properties of films and surfaces at nano and micro scales. It involves applying controlled mechanical loads using a small, hard indenter of specified geometry (e.g., spherical, Berkovich, spherical, cube corner, etc.) to the sample. The loads typically range from a few μN to mN and are applied to create a load-displacement (P-h) curve as the indenter penetrates the material. The load-displacement characteristics can reveal valuable information about the material's mechanical properties. The most common use of nanoindentation is for measurement of elastic modulus and hardness using the method developed by Oliver and Pharr [16]. This method involves measuring the slope of the unloading curve at the peak load (P_{max}) to determine the stiffness (S). From the indentation depth at peak load (h_{max}), the contact depth at maximum load (h_c) can be calculated using the expression $h_c = h_{max} - \epsilon \frac{P_{max}}{S}$, where ε is a geometric factor associated with the indenter shape. The contact area A_c is estimated from h_c using a calibration curve. The hardness (H) is then calculated as $H = \frac{P_{max}}{A_c}$. The reduced Young's modulus (E_r) which accounts for the elastic deformation of both the sample and indenter and can be expressed as $E_r = \frac{1}{2}\sqrt{\frac{\pi}{A_c}}S$. E_r is related to the Young's modulus of the sample (E_s) and indenter (E_i) by the relationship $\frac{1}{E_r} = \frac{(1-\vartheta_s^2)}{E_s} + \frac{(1-\vartheta_i^2)}{E_i}$. Additionally, during the loading process, abrupt

increases in displacement called "pop-in" events may occur, attributed to nucleation of dislocations or shear bands, crack formation, or phase transformation. A statistical analysis of the features of pop-ins such as the load at which they occur, and the magnitude of the displacement burst can provide insights into the yielding and plastic deformation mechanisms in materials [17]. In addition to these basic measurements, modern instrumented indenters come with the ability to control temperature and environment allowing us to test the behavior of materials over a wide range of operating conditions. The experiments can also be automated to perform high throughput mechanical characterization. Lastly it is a versatile technique that requires minimal sample preparation and has very few restrictions on sample shapes and dimensions. All the nanoindentation experiments described in this thesis were carried out on a Hysitron TI – 950 Tribiondenter.

2.3 Molecular Dynamics Simulations

Molecular Dynamics (MD) is a powerful simulation technique used to study the behavior and dynamics of materials at the atomic level. In classical MD simulations, the positions, velocities, and interactions of individual atoms are numerically integrated over time based on Newton's equations of motion. By iteratively updating these atomic positions and velocities, MD simulations can accurately predict the time-evolution of a system under the influence of interatomic forces. In this thesis, MD simulations have been used to understand the mechanisms of deformation in a variety of amorphous materials including several metallic glasses and amorphous SiO_2. These simulations are a very useful tool to understand the influence of atomic level structure on the mechanical behavior of materials [18] [19] [20]. In materials such as glasses where the featureless amorphous structures are difficult to characterize experimentally, MD simulations along with tools such as Voronoi tessellation [21] can be used as a means to connect atomic level structure to experimentally observed properties to establish valuable structure-property correlations Further, MD codes can be parallelized and executed efficiently on multiple computers to allow simulations of large systems over longer time scales, bridging the gap to experiments to some extent. LAMMPS is a specialized MD code designed for efficient execution on parallel computers [22]. All the MD simulations in this thesis have been performed on LAMMPS.

3. Ion beam assisted deposition of metallic glasses

This chapter is based on work done in collaboration with Prof. Paul Voyles and Prof. John Perepezko groups. A manuscript is in preparation and is to be submitted for publication.

3.1 Introduction

Thin film metallic glasses (TFMGs) are excellent candidates to be used as coatings in a variety of applications such as biomedical implants, surgical equipment, semiconductor packaging and flexible electronics due to their good biocompatibility, antimicrobial properties, high strength, and high elastic limit along with resistance to wear, fatigue, and corrosion [6,23,24]. TFMGs allow us to exploit the unique properties associated with the amorphous structure of metallic glasses (MGs) over a large composition space without having to worry about the glass forming ability as in the case of bulk metallic glasses.

Although the first TFMGs were synthesized by solid state amorphization of multi-layer films [25], physical vapor deposition (PVD) has emerged as the preferred synthesis route. The interest in PVD synthesized TFMGs increased considerably after Swallen *et al.* [26] demonstrated that PVD could yield organic glasses with enhanced stability. They found higher kinetic and thermodynamic stability in organic glasses deposited at a substrate temperature slightly below the glass transition temperature of an ordinary melt quenched glass. These glasses were referred to as “Ultrastable” because such high stability is practically unattainable in conventional liquid cooled glasses. Following this discovery, there were several reports of the use of PVD to synthesize TFMGs having increased stability[27–32]. When it comes to the practical applications of TFMGs as coatings, increased stability in the form higher glass transition temperatures and hardness is particularly useful since it would allow increased operating temperatures as well as improve wear and fatigue resistance.

The PVD process has many tunable parameters that can affect the properties of the deposited film. However, the only process parameters that have been shown to influence stability are the substrate temperature and the deposition rate. In general, higher substrate temperatures (around 0.8 times T_g of the ordinary glass) or lower deposition rates have been found to result in MGs with higher stability. Swallen *et al.* [26] explained that all the atoms or molecules in the film would have been in a mobile surface layer [33–

38] at some point during the deposition process, where they would have had the ability to move around and find more stable configurations before being buried under the surface. Elevated deposition temperatures enhance surface mobility while lower deposition rates increase the surface residence time, allowing surface atoms or molecules to find highly stable configurations and resulting in ultrastability. Either way, the key to achieving ultrastable glasses is believed to be the higher mobility of the atoms or molecules at the surface. This reasoning was backed by Berthier *et al.* [39] who used molecular dynamics simulations to separate the surface dynamics from bulk dynamics in a Lennard-Jones glass and directly demonstrated how enhanced surface mobility is responsible for the ultrastability of vapor deposited glasses.

Considering the importance of surface mobility in controlling stability, we have identified a new route to synthesize TFMGs using Ion Beam Assisted Deposition (IBAD). This process involves the bombardment of the growing film with ions in order to modify its structure and properties. IBAD is commonly used to tune residual stresses, substrate adhesion, surface roughness, hardness, refractive index, magnetic anisotropy, etc. [40] in crystalline films. This process is different from what Luo *et al.* [30] refer to as IBAD. In their method, the ion beam is directed at a target from which atoms are sputtered towards the substrate at very low deposition rates. We have used ion beams directed at the surface of a growing film according to the conventional definition of IBAD and obtained TFMGs with increased kinetic stability and hardness. Our approach is also different from that of Kobata and Miura [41] who used a technique called unbalanced magnetron sputtering to irradiate the surface of a growing metallic glass film. While they implant Ar^+ ions into the TFMG to change its composition and properties, we irradiate the growing film with relatively low energy Ar^+ ions to transfer kinetic energy to the surface atoms and increase their mobility, while avoiding implantation of the incident ions. In comparison to other approaches to enhance the stability of TFMGs, IBAD offers some key advantages such as, *(i)* not needing to heat the substrate, and *(ii)* not needing to use extremely low deposition rates and therefore reducing the time needed to grow films by orders of magnitude.

3.2 Materials and Methods

MG films were prepared using a DC magnetron sputtering system retrofitted with a single beam ion source acquired from Scion Plasma. The films were grown under three distinct conditions: (1) without ion beam irradiation (*No IB*), (2) with the ion source activated at an ion energy of 90eV (*90eV IB*), and (3) with the ion source activated at an ion energy of 180eV (*180eV IB*). The angle of ion incidence was maintained constant at 70° with respect to the normal. The sputtering process employed a single alloy target of composition $Pd_{77.5}Cu_6Si_{16.5}$, obtained from ACI Alloys Inc. The sputtering power remained fixed at 50W, and the deposition was conducted at room temperature for a duration of 100 minutes to achieve film thickness in the range of 1.2-1.5 μm. The base pressure in the deposition chamber was below $2*10^{-7}$ Torr and the operating pressure of the Ar process gas was maintained at $3.0*10^{-3}$ Torr. Two types of substrates were utilized for film growth. NaCl discs, with a diameter of 25mm, served as the substrates for films employed in differential scanning calorimetry (DSC) experiments. Additionally, Si wafers were cut into squares measuring 10 x 10 mm^2 and used as substrates for films used in nanoindentation and other characterization techniques. The quenched *Ribbon* sample, prepared by Dr. Zijian Wang, was made by melt-spinning on a Cu wheel in an Ar atmosphere.

A Perkin Elmer Diamond Differential Scanning Calorimeter (DSC) was employed to examine the thermal properties of the films and *Ribbon* sample under 20 mL/min flowing pure Ar gas. Measurements were done *via* a 6-step protocol: 1. Isothermal hold at 50°C for 1min; 2. Heat to 550 °C at 20 °C /min; 3. Isothermal hold at 550 °C for 1min; 4. Cool to 50 °C at 100 °C /min; 5. Isothermal hold at 50 °C for 1min; 6. Heating to 550 °C at 20 °C /min. Final heat flow of the sample as a function of temperature is obtained by subtracting the heat flow curve of step 6 form that of step 2. The DSC experiments were performed by Dr. Zijian Wang.

The composition of the films was measured using X-ray photoelectron spectroscopy (XPS) performed on a Thermo Scientific K alpha system using an Al K-α source. To remove the oxidized surface layer, the sample was ion-milled to a depth of 10nm using Ar^+ ions before measuring the composition. The XPS peak fitting and analysis was carried out using the Thermo Scientific Avantage Software. X-ray diffraction (XRD) was performed on a Bruker D8 Discover instrument with a Cu K-α source. The surface

morphology of the films was characterized by atomic force microscopy (AFM) on a Bruker Icon instrument. Data was acquired in the tapping mode with a TESPA-V2 tip. Nanoindentation was performed on a Hysitron TI 950 Triboindenter equipped with a diamond Berkovich probe and a nanoDMA-3 transducer. 30 indents were performed on each sample in the load controlled mode with a loading rate of 1000μN/s. The maximum load was selected to ensure that the indent depth didn't exceed 10% of the film thickness in order to avoid substrate effects on the measured nanomechanical properties. The elastic modulus and hardness were calculated from the load-displacement data using the Oliver-Pharr method [16].

Threshold displacement energies (E_{TD}) for Pd and Si surface atoms were calculated by classical molecular dynamics (MD) simulations using the LAMMPS software package [22] and a binary EAM potential [42]. A melt-quenched glass with composition $Pd_{82}Si_{18}$ with dimensions 1.4 x 1.4 x 1.4 nm^3 was obtained using the procedure described in [9]. The quenched glass was used to calculate the E_{TD} with the following steps. First, the system was equilibrated to a temperature of 300 K in the NVE ensemble with periodic boundary conditions in two directions and a free surface along one direction. Next, atoms on the free surface were selected as primary knock on atoms (PKAs) at random and assigned kinetic energies. The system was then allowed to equilibrate again in the NVE ensemble for 1ps and the displacement of the PKA was determined. A displacement cutoff equal to the nearest neighbor distance from the pair distribution function was used to determine whether the PKA was permanently displaced. The assigned initial kinetic energy was increased in increments of 5eV to first determine a coarse E_{TD}. Then, the initial kinetic energy was increased in increments of 1eV starting from the coarse E_{TD} to determine a more accurate value of the E_{TD}. The reported E_{TD} is an average of 20-30 runs with different PKAs for each atom type. PKA energies for varying incident ion energies were determined using the SRIM package [43].

3.3 Results and Discussion

The compositions of the films and the quenched *Ribbon* sample were measured using XPS (Table 3.1) and were confirmed to be close to the nominal composition of $Pd_{77.5}Cu_6Si_{16.5}$ (within XPS accuracy of 5% [44]). Absence of Ar in the *90eV IB* and *180eV IB* films indicates that the ion energies chosen for IBAD were low enough to avoid implantation of Ar^+ ions in the films.

Sample	Pd (at. %)	Cu (at. %)	Si (at. %)
Ribbon	75.3 ± 0.8	6.5 ± 0.3	18.2 ± 0.5
No IB film	75.4 ± 0.5	5.7 ± 0.3	18.9 ± 0.5
90eV IB film	77.1 ± 0.8	5.2 ± 0.1	17.7 ± 0.8
180eV IB film	75.9 ± 0.4	5.4 ± 0.2	18.7 ± 0.5

Table 3.1 XPS measured compositions of as deposited films and ribbon.

Diffraction patterns obtained from a laboratory XRD setup are shown in Fig.3.1. All the samples show a single broad diffraction peak that indicates a fully amorphous structure. Although the positions of the diffraction peaks are all within a range of less than 1°, closer inspection reveals that the amorphous diffraction peak also referred to as the first diffraction peak (FDP) occurs at a higher scattering vector magnitude ($q = 4\pi*\sin\theta/\lambda$, where λ is the wavelength of the incident x-ray) in the *Ribbon* sample ($q = 2.85$ $Å^{-1}$) as compared to the vapor deposited films. Among the films, the position of the peak shifts to slightly lower q values going from the *No IB* film ($q = 2.83$ $Å^{-1}$) to the *90eV IB* film ($q = 2.81$ $Å^{-1}$) and the *180eV IB* film ($q = 2.81$ $Å^{-1}$). The Ehrenfest relationship [45] ($q \propto 1/r$, where r is the shortest interatomic distance) would suggest that the *Ribbon* sample with the FDP occurring at the highest q has the lowest interatomic spacing in the nearest neighbor shell and therefore a lower average atomic volume or higher density. However, it has been shown that in the case of multicomponent systems, the position of the FDP in the XRD pattern is not always inversely proportional to the average atomic volume [46]. Since the position of the FDP in the XRD pattern is only sensitive to the heaviest atoms in the system, it does not consider the separation distances between atom pairs consisting of lighter atoms and does not reflect the average atomic spacing. Therefore, it is not possible to draw conclusions on density changes based on the position of the FDP. Nonetheless, it is still safe to say that the differences in the position of the FDP indicate slight variations in the atomic level topological and chemical ordering in the samples.

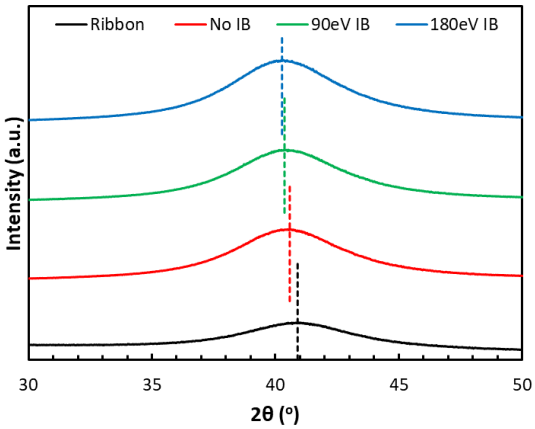

Fig. 3.1 XRD patterns of as deposited films and ribbon.

Fig.3.2a-c show the surface morphology of the films obtained from AFM. The *No IB* film has a roughness of 1.7nm and has a nanostructure consisting of grains with diameter in the range of 20-40nm. The *90eV IB* and *180eV IB* films have atomically smooth surfaces with roughness of 0.18nm and 0.23nm respectively and appear to have a homogenous surface with no distinct features. Such a transition from a nanostructured to a homogenous surface morphology in vapor deposited films is generally attributed to increased mobility of surface atoms [47–49]. The nanostructured surface morphology in the *No IB* film is a consequence of columnar growth also known as the Volmer-Weber or island growth mode [50]. This film growth mode occurs when the deposited atoms prefer to bind with each other rather than the substrate atoms, resulting in high interfacial energies between the film and substrate. Consequently, the adatoms arriving at the substrate form islands to minimize the interfacial area. As the islands grow, the subsequently arriving adatoms will have a higher probability of being deposited on top of the relatively tall islands which will continue to grow at the expense of the shorter islands in their shadow. This is called the shadowing effect and results in the growth of columnar regions with relatively high atomic densities separated by boundaries with low atomic density. However, if the atoms arriving at the surface on top of the taller columns have sufficient mobility, they will be able to diffuse to the surrounding areas with low atomic densities resulting in a smooth surface [49]. Based on this reasoning, the smooth surfaces seen in the *90eV IB* and the *180eV IB* films can be explained as a consequence of increased surface mobility. This agrees with the hypothesis that low energy ion irradiation imparts mobility to the surface atoms on the growing film.

Elastic modulus measured by nanoindentation (Fig.3.3a) shows a 33% increase from the quenched *Ribbon* sample to the *No IB* film. The ion beam doesn't seem to have any obvious effect on the elastic modulus of the films with the *90eV IB* film showing a 4.4% decrease with respect to the *No IB* film while the *180eV IB* film shows almost no change. A higher elastic modulus is generally a consequence of a shorter average interatomic distances and a denser glass structure [32]. This suggests that the films have a higher density than the *Ribbon* sample and the density doesn't change much with the use of IBAD. Comparing nanoindentation hardness (Fig.3.3b), we see a gradual increase going from the *Ribbon* sample to the *No IB* film followed by the *90eV IB* film and then the *180eV IB* film. Overall, there is an 11% increase in hardness from the *Ribbon* to the *180eV IB* film. Among films, there is a 5.3% increase in hardness from the *No IB* to the *180eV IB* film. Unlike the elastic modulus, the hardness which is a measure of a material's resistance to deformation is influenced not only by the interatomic distances but also other factors like the surface roughness, morphology, and microstructure. In the case of the films, it is clear that the surface morphology changes from a nanograined, heterogenous surface to a smooth, homogenous surface with the use of the ion beam during deposition. Such a change in morphology has been shown to result in increased hardness in metallic glass films [51]. In order to further probe the differences in the mechanical behaviors of the samples, we examine the nanoindentation load-displacement curves. These curves usually contain serrations or pop-ins that are believed to correspond to the activation of shear bands beneath the indenter [52]. During load controlled nanoindentation, the pop-ins occur in the form of sudden bursts of displacements, and the first pop-in corresponds to the onset of plastic deformation [53]. The load at the first pop-in can be considered the threshold load for the activation of shear bands in metallic glasses [54]. Fig.3.3c shows the average load at the first pop-in for the four samples in this study. The *Ribbon* sample has the lowest threshold load for the activation of shear bands, reflected in its low hardness. Among the films, the *No IB* film has the lowest load at the first pop-in. This can be understood by considering the morphology of the *No IB* film that consists of nanograins separated by boundaries containing loosely packed atoms with excess free volume. These boundary regions allow the easy activation of shear bands and offer lower resistance to plastic deformation, resulting in lower hardness compared to the films grown using IBAD where the nanograined structure is eliminated due to enhanced surface mobility during film growth. Further, the *90eV IB* film has a higher threshold for activation of shear bands compared to the *180eV IB* film, which

is surprising considering that it has lower hardness. This means that the *180eV IB* film is more resistant to plastic deformation in spite of allowing easier activation of shear bands compared to the *90eV IB* film. A possible explanation for this is that the *180eV IB* film could be more heterogenous at the atomic scale compared to the *90eV IB* film due to differences in local structural and chemical ordering. This heterogenous structure will consist of relatively softer regions that will allow easy activation of embryonic shear bands which will then be constrained by the surrounding regions that are stiffer. In this way, the *180eV IB* film can have a lower threshold for activation of shear bands and at the same time offer a greater resistance to plastic deformation, resulting in higher hardness compared to the *90eV IB* film.

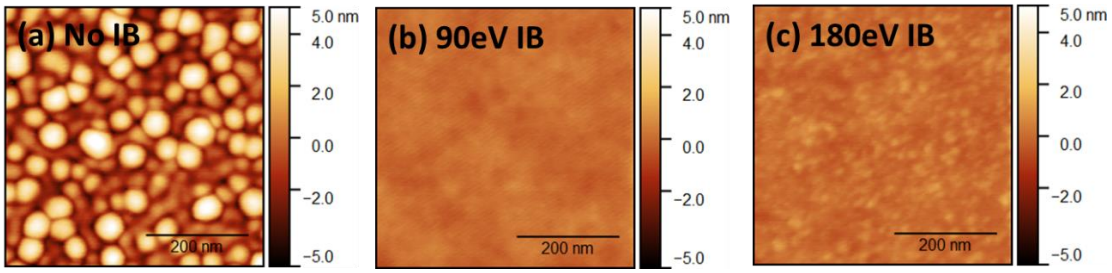

Fig. 3.2 AFM image of surface morphologies of (a) No IB, (b) 90eV IB, and (c) 180eV IB films in as deposited state.

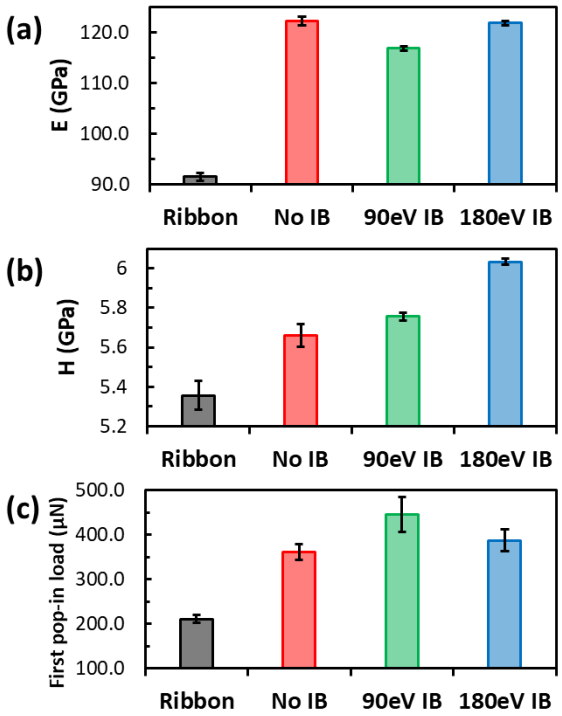

Fig. 3.3 (a) Elastic modulus, (b) Hardness, (c) Load at first pop-in measured by nanoindentation.

Heat flow traces from the DSC heating scan of all the samples are shown in Fig.3.4a. All of the traces exhibit an endothermic step corresponding to the glass transition around 360^{o}C and an exothermic peak corresponding to crystallization at around 400^{o}C, agreeing with reported values in literature [55]. However, there is a striking difference between the DSC traces of the *Ribbon* sample and the films prior to the glass transition. The *Ribbon* has a relatively flat heat flow curve prior to the onset of glass transition while the films appear to be undergoing an exothermic change as seen by the downward sloping heat flow curve. Such an exothermic change usually corresponds to relaxation of the glass towards a more stable thermodynamic state [56]. This would suggest that the as deposited state of the films is thermodynamically less stable compared to the *Ribbon* sample which does not exhibit an exothermic slope prior to the glass transition. Lower thermodynamic stability in MGs is sometimes associated with less dense structures and lower elastic moduli [32]. This would be in contradiction to the significantly higher nanoindentation elastic modulus seen in the films compared to the *Ribbon* sample. However, Yu *et al*. [27] who were among the first to report ultrastability in MGs also observed that the ultrastable MG with the higher elastic modulus had a higher enthalpy and was less thermodynamically stable than the quenched MG. In their study, they referred to the ultrastable MG as the one that had the higher kinetic stability (higher glass transition temperature), rather than thermodynamic stability and concluded that the kinetic stability of metallic glasses is not always coupled with their thermodynamic stability. While our results seem be similar to that of Yu *et al*. [27], we should note that the inference about the thermodynamic stability of our samples is only speculative since it is not possible to draw reliable conclusions about the relative thermodynamic stabilities from just comparing the heat flow curves, without establishing a baseline and calculating the difference in enthalpies with respect to a common reference state. Another plausible explanation could be that the observed exothermic behavior in the DSC traces of the films is from residual stresses developed in the films during the deposition process. It is not surprising that the films will develop large amounts residual stresses given their sizeable thickness [24]. The idea that the films possess residual stresses is supported by the observed curling up of the films on being separated from the substrate (Fig.3.5).

The glass transition temperature reported for MGs in literature usually corresponds to the onset of the glass transition on heating. However, the steep curvature in the DSC traces of our films makes it tricky to measure the onset T_g. Instead, we report the midpoint glass transition temperature which corresponds

to the midpoint in the endothermic step in the glass transition and can be determined without ambiguity from the peak in the derivative of the heat flow curve (Fig.3.4b-e). We see that the T_g of the *Ribbon* sample (T_g = 367°C) and that of the *No IB* (T_g = 366°C) and *90eV IB* (T_g = 368°C) films all lie within a range of 2°C and can be considered to have almost identical kinetic stability. Only the *180eV IB* (T_g = 372°C) film appears to show a slightly higher T_g indicating a modest increase in kinetic stability with respect to the other samples.

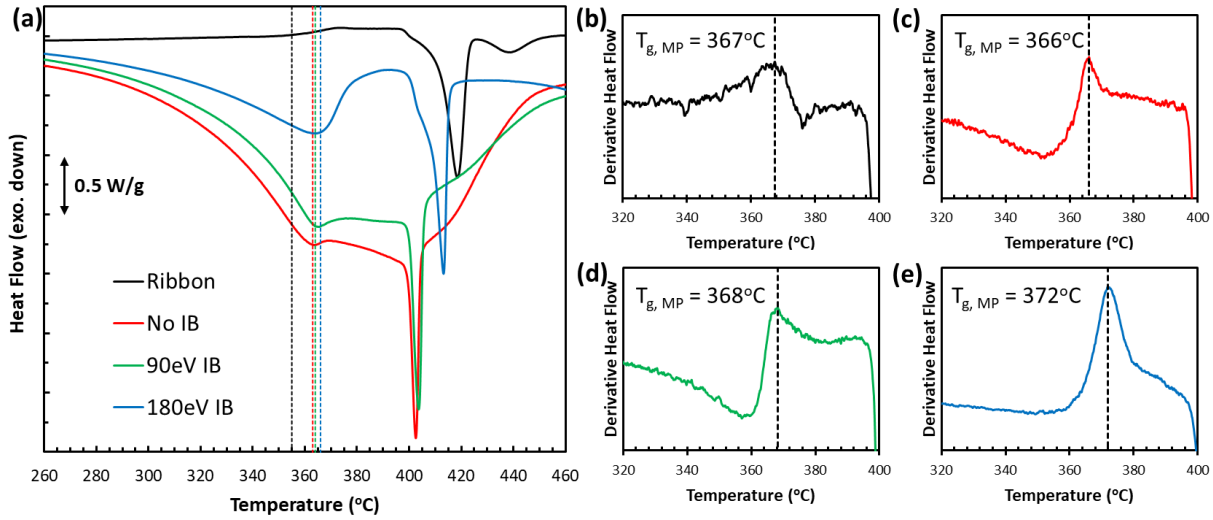

Fig. 3.4 (a) DSC heat flow traces from heating scans; Derivative of heat flow traces for (b) Ribbon, (c) No IB, (d) 90eV IB, (e) 180eV IB films in as deposited state. Data from Dr. Zijian Wang.

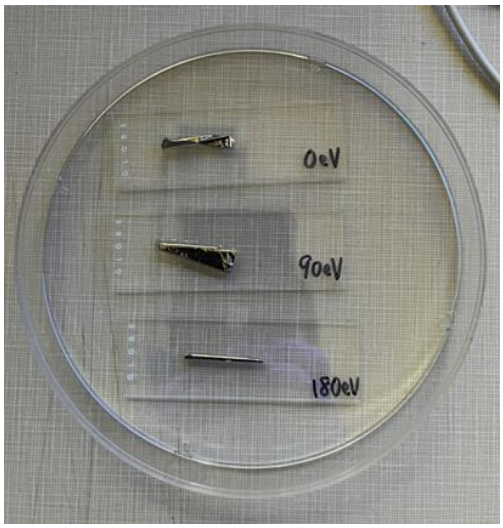

Fig. 3.5 Curling up of the films after being separated from NaCl substrate. Photograph from Dr. Zijian Wang.

The crystallization peaks of all the samples have onset temperatures (T_x) very close to each other, the *Ribbon* sample (T_x = 398°C), *No IB* film (T_x = 400°C), and the *90 eV IB* (T_x = 399°C) film are again within a range of 2°C with the 180 eV *IB* (T_x = 402°C) only marginally higher. However, the peak crystallization temperatures show a larger variation between the samples. The *Ribbon* sample (T_{xp} = 419°C) has the highest T_{xp} followed by the *180eV IB* sample (T_{xp} = 414°C). The *No IB* film (T_{xp} = 403°C) and the *90eV IB* film (T_{xp} = 404°C) have the lowest T_{xp} and the narrowest crystallization peaks. The differences in the T_{xp} of the samples indicate differences in crystallization pathways, which is confirmed by the diffraction patterns obtained after crystallization (Fig.3.6). The *Ribbon* sample with the highest T_{xp} has the most distinct diffraction peaks among the samples. However, this is not unexpected since melt-quenched MGs with the same composition as vapor deposited MGs have been shown to select different crystallization pathways due differences in their topological and chemical medium range orders [57]. What is more surprising is the difference in the diffraction patterns of the films, with the *180eV IB* film having clearly different peaks compared to the *No IB* and *90eV IB* films which have almost identical diffraction patterns. This means that the use of higher energy ions during IBAD alters the structure or the composition of the glass in a way that results in a different crystallization pathway. While ion irradiation has been shown to result in segregation and crystallization in MGs [58,59], such processes usually require the use of heavy ions with high energies. Further, we have already confirmed that our samples are fully amorphous using XRD to rule out the possibility of crystallization induced by the ion beam. In addition, we have also checked for elemental segregation at different length scales using SEM as well as TEM EDS mapping (Fig.3.7 and Fig.3.8). The EDS maps at the micrometer and nanometer length scales show no evidence of segregation in any of the films. All these results suggest that the reason for the different crystallization pathway in the *180eV IB* film could be changes in the topological and chemical medium or short range orders at length scales that cannot be observed in the XRD or EDS experiments.

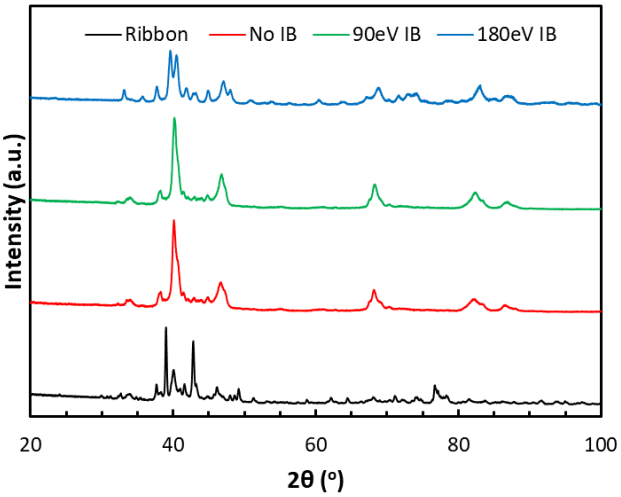

Fig. 3.6 XRD patterns of samples after crystallization.

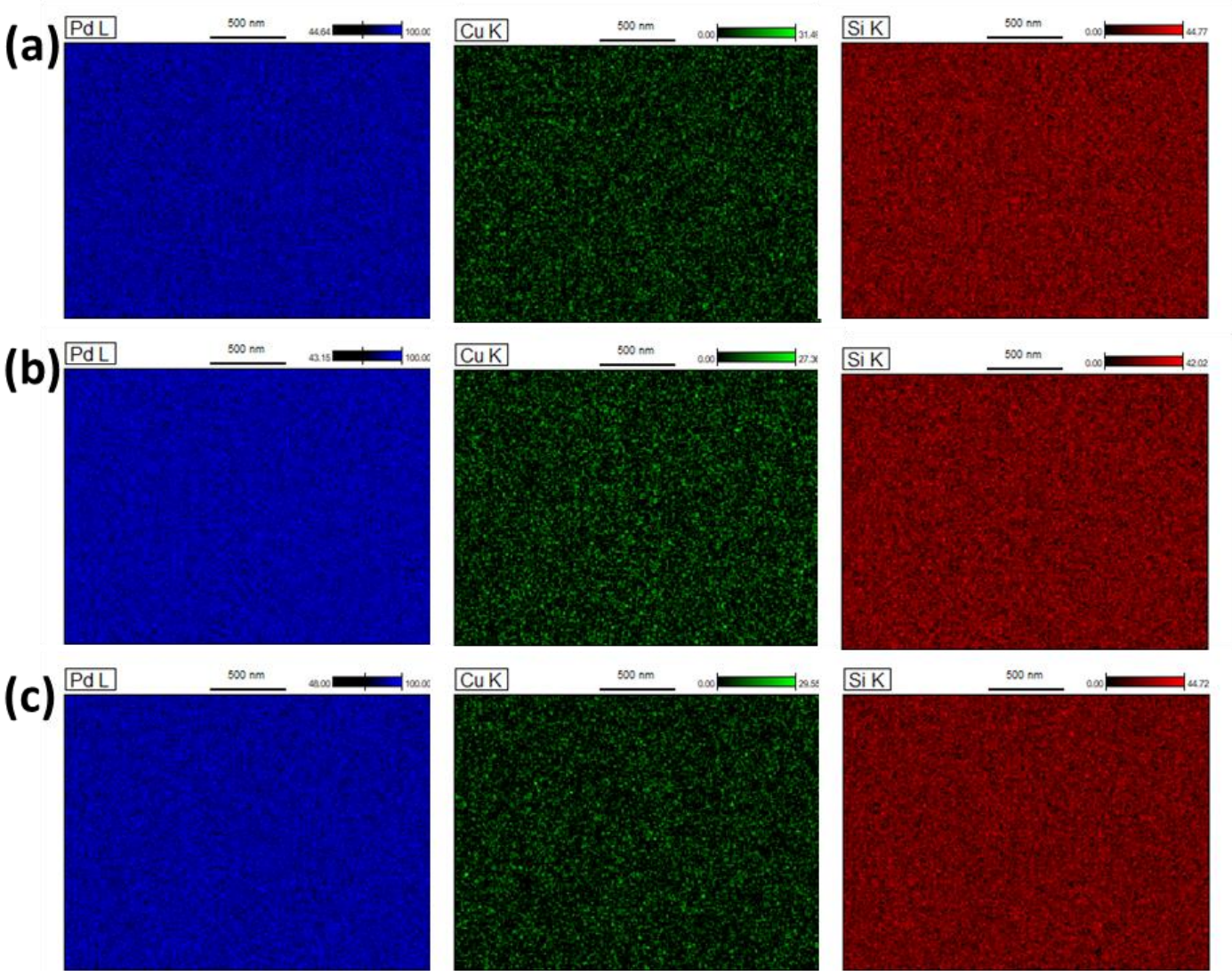

Fig. 3.7 SEM EDS elemental maps for (a) No IB, (b) 90eV IB, and (c)180eV IB films showing no microstructural chemical segregation.

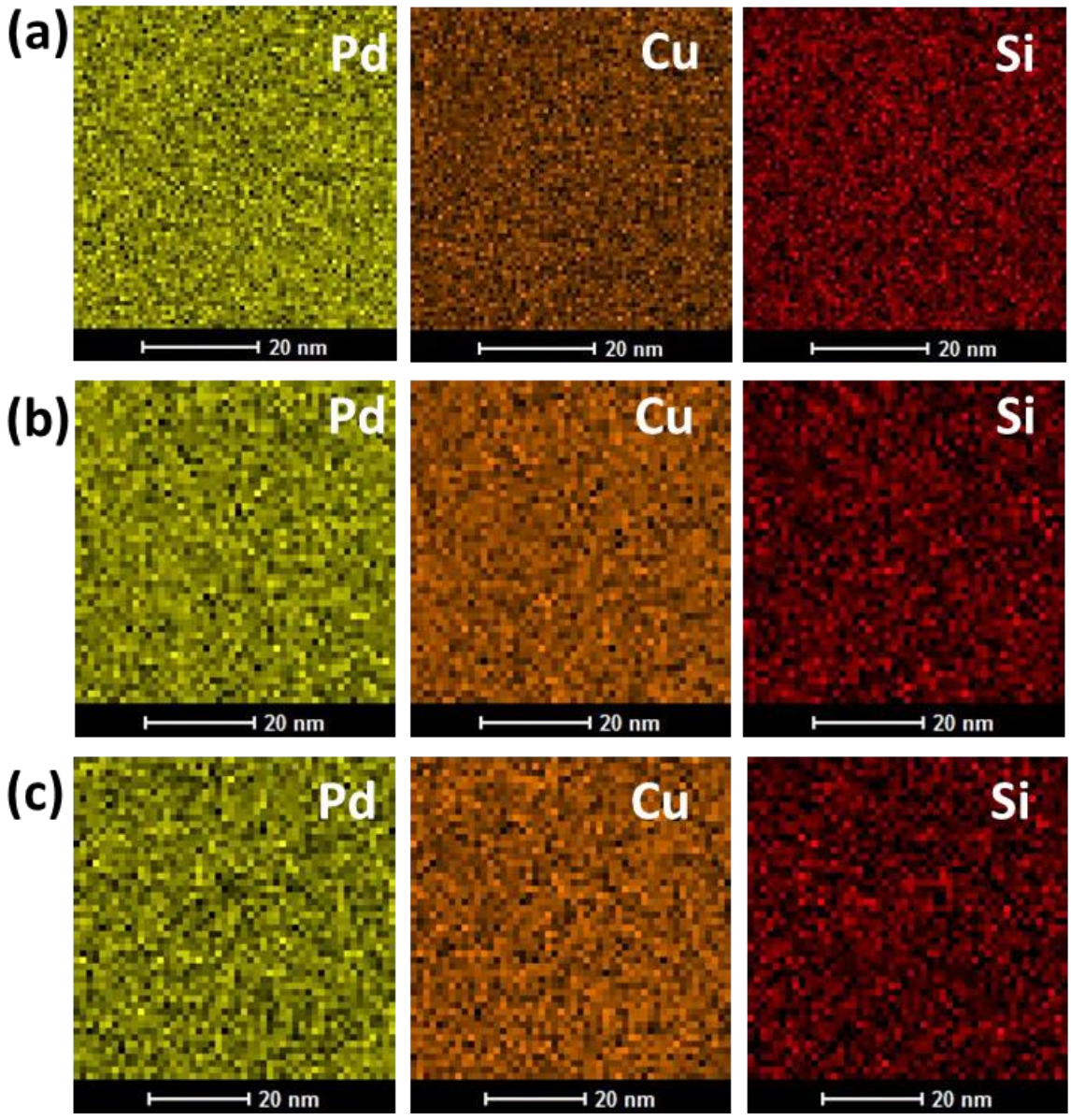

Fig. 3.8 TEM EDS elemental maps for (a) No IB, (b) 90eV IB, and (c)180eV IB films showing no nanoscale chemical segregation. Images from Dr. Soohyun Im.

In order to understand the reason behind the differences in the crystallization behaviors of the films prepared under different ion beam energies, we look at interactions between the incident ions and the film adatoms. During the IBAD process, the Ar^+ ions incident on the surface of the growing film will undergo collisions with the atoms on the surface and transfer kinetic energy. The atoms that undergo collisions with the incident ions are called primary knock on atoms (PKAs), and the energy transferred to the PKAs depends on their distance from the surface. Fig.3.9a and Fig.3.9b show the energy absorbed by the PKAs as a function of their depth from the surface for incident ion energies of 90eV and 180eV respectively. It can be seen in both cases that the energy of the incident ions is almost entirely transferred to atoms at the surface layer. Further, we see that Pd atoms absorb the largest fraction of the incident ion energy followed by the Si and Cu atoms. The PKAs can behave in different ways depending on the amount of kinetic energy they receive. The minimum kinetic energy needed to permanently displace the PKAs from their initial position is called the threshold displacement energy (E_{TD}). If the kinetic energy transferred to the PKA is less than the E_{TD}, the atom will not be displaced but will undergo oscillations around its equilibrium position which may result in local heating. On the other hand, energy absorbed by the PKA is higher than its E_{TD}, the atom will be displaced resulting in a collision cascade. In Fig.9, the E_{TD} for Pd and Si atoms are compared with the PKA energies. The dotted lines represent the E_{TD} for atoms in the bulk [43] and the dashed lines represent the E_{TD} for the same atoms when they are present on the surface. We observe that the E_{TD} for the surfaces atoms is much lower than that for atoms in the bulk, which makes sense considering that the atoms at the surface have fewer bonds that will require lower energy to be broken before the atom is displaced. Comparing Fig.3.9a and Fig.3.9b, we see that the 90eV ions don't have sufficient energy to displace the Si atoms and barely exceed the E_{TD} for the surface Pd atoms. Upon increasing the ion energy to 180eV, we see that the incident ions easily exceed the E_{TD} Pd atoms as well as surface Si atoms. This means that the mode of interaction between the ion beam and the film changes with increasing ion beam energy. At low ion energies, the incident ions don't have sufficient energy to displace the surface atoms but may cause local heating through vibrations of the PKA and surrounding atoms. The smoothening of the surface in the *90ev IB* film suggests that the local heating caused by the low energy ions may be sufficient to improve the mobility of the surface atoms enough to eliminate the columnar structure seen in the *No IB* film. At higher ion energies, the incident ions are capable of displacing the surface atoms and causing

collision cascades, resulting not only in the smoothening of the surface but possibly changes in the topological and chemical medium or short range orders, as evidenced by the different crystallization pathways in the *180eV IB* film and the *No IB* film. It is interesting to note that Giordano and Ruta [60] have reported the presence of an additional secondary relaxation process in a glass of the same composition as ours. This additional secondary relaxation is said to be related to the onset of nucleation or phase separation prior to crystallization was found to take place upon annealing at high temperatures. It is possible that the higher energy ions used in IBAD activate the same or a similar relaxation process leading to the structural or chemical ordering as a precursor to crystallization. Such a process may result in heterogeneities at the atomic scale as mentioned in the discussion on nanoindentation results as well as a different crystallization pathway as expected based on the diffraction patterns of the crystalized films. Verification of such a hypothesis requires additional structural characterization that is outside the scope of this thesis but may be an interesting topic to explore going forward.

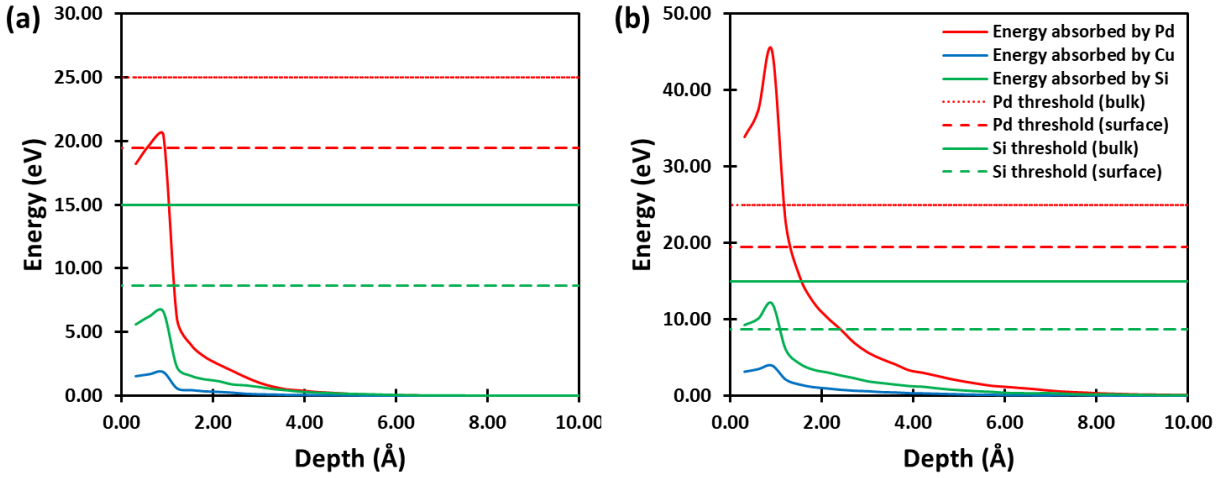

Fig. 3.9 Energy absorbed by primary knock-on atom (PKA) (solid) for ion beam energy of (a) 90eV and (b) 180eV compared with threshold displacement energy (E_{TD}) of bulk atoms (dotted) and surface atoms (dashed).

3.4 Conclusions and Outlook

We have demonstrated IBAD to be a promising technique to synthesize TFMGs and control their properties. We have atomically smooth surfaces along with enhancements in the kinetic stability and hardness of TFMGs grown using IBAD. By employing higher energies, IBAD has also appeared to significantly alter the atomic level structure in TFMGs, resulting in the selection of different crystallization pathways upon heating. From an applications standpoint, this process holds significant potential for TFMGs with exceptional kinetic stability and hardness, making them ideal candidates for coatings in several engineering applications, provided that the IBAD parameters, such as ion energies and incidence angles are optimized. From a scientific perspective, we have decoupled the surface mobility from bulk mobility, and provided further evidence to hypothesis that increased surface mobility plays a crucial role in the heightened stability of vapor-deposited glasses. Moving forward, there remains an interesting avenue to explore the unique secondary relaxation process observed in the Pd-Cu-Si based MG by employing IBAD-synthesized films. This research presents a comprehensive contribution to the understanding the synthesis of TFMGs by vapor deposition, opening up exciting possibilities for future investigations and practical applications.

4. E-beam vapor deposition of amorphous silica

This chapter is adapted from the paper: V. Jambur, M. Molina-Ruiz, T. Dauer, D. Horton-Bailey, R. Vallery, D. Gidley, T. H. Metcalf, X. Liu, F. Hellman, I. Szlufarska, Temperature effects on the structure and mechanical properties of vapor deposited a-SiO_2, Journal of Non-Crystalline Solids, 587, p.121588 (2022).

4.1 Introduction

Amorphous SiO_2 (a-SiO_2) is known to exhibit many anomalous thermo-mechanical behaviors; its elastic modulus increases with increasing temperature [61], the bulk modulus goes through a minimum at around 2 GPa during compression [62], and it has a negative thermal expansion coefficient at low temperatures in the range of 140 K to 210 K [63]. Molecular dynamics (MD) studies have linked the anomalous behaviors to local, reversible polyamorphic transitions in the network structure of a-SiO_2 [64]. These transitions involve changes in the medium range order and affect the ring geometry in the a-SiO_2 network while the short-range structure (bond lengths, bond angles, and coordination numbers) remains unchanged. However, there is currently lack of experimental evidence for these local reversible transitions due to the difficulty in characterizing the topological changes in the medium range structure of a-SiO_2. In addition to the aforementioned anomalies in the elastic response, a-SiO_2 has been found to undergo irreversible densification when subjected to high pressure [65]. Experimental [66,67] and theoretical [65,68] studies on this pressure induced transformation have shown that the densification of the a-SiO_2 network structure is accompanied by the formation of smaller network rings.

a-SiO_2 films and coatings have found key applications in many industries including semiconductors [69], optical systems [70], and photovoltaics [71] to name a few. While sol-gel synthesis [72] and chemical vapor deposition (CVD) [73] are the most commonly used methods to synthesize a-SiO_2 films, physical vapor deposition (PVD) is an environmentally friendly alternative that does not require dangerous reactants or high temperatures [74]. In addition, the enhanced surface mobility achieved in some vapor deposited glasses allows those systems to easily explore the energy landscape and find more stable configurations [75] that cannot be accessed through conventional melt-quench techniques that are used to synthesize bulk glasses. This means that the process parameters in PVD can be tuned to obtain glasses with optimized

properties. For any application, it is generally desirable to have films with higher elastic modulus and hardness in order to provide mechanical integrity and to ensure durability. In the case of organic and metallic glasses, PVD process parameters like deposition rate and substrate temperature have been tuned to yield denser films with high elastic modulus and hardness [32,76]. However, there is still a lack of a systematic understanding of the influence of PVD process parameters on the structure and mechanical properties of a-SiO_2 films.

In this work, e-beam evaporation, a PVD technique, was used to prepare a-SiO_2 films over a range of temperatures from 60 °C to 900 °C. In doing so, we were able to sample a wide range of a-SiO_2 structures and study their influence on mechanical behavior. We also obtained new insights on the thermally induced structural transitions and anomalous thermomechanical behaviors in a-SiO_2. Structural changes in terms of the density and porosity were measured using characterization techniques such as Rutherford backscattering spectrometry (RBS), profilometry, and positron annihilation lifetime spectroscopy (PALS), while mechanical characterization was carried out using nanoindentation and double-paddle oscillator. The experimental observations were then interpreted with the help of MD simulations.

4.2 Materials and Methods

a-SiO_2 films were prepared by e-beam evaporation of 99.999% SiO_2 pieces. The base pressure was ~1×10^{-8} Torr, films were grown at 0.5 Å/s, with substrate temperatures ranging from 60 °C to 900 °C. Some films were capped with a thin (5 nm) Al layer to prevent water absorption [77]. Films thickness was measured by a KLA Tencor ASIQ profilometer, ranging from 800 nm to 1000 nm for nanoindentation measurements, and from 200 nm to 600 nm for ion beam analysis (IBS) and PALS measurements.

IBS was performed in the films by means of RBS and elastic recoil detection analysis (ERDA) in a NEC model 5SDH Pelletron tandem accelerator, with a beam energy of 3040 keV. RBS was used to determine the film's stoichiometry, and in combination with profilometry, the film's density. The density is calculated as the ratio between surface aerial atomic density (obtained by RBS) and the film thickness (obtained by profilometry). ERDA was used to quantify hydrogen presence in the films associated with water absorption. Film growth and density measurements were performed by Dr. Manel Molina-Ruiz.

Positron Annihilation Lifetime Spectroscopy (PALS) is a well-established technique for probing free volume voids in insulating materials [78,79]. In general, positrons from a radioactive source are stopped in the target material where a fraction capture an electron and form the long-lived triplet state of positronium (the hydrogen-like bound state of the electron and its antiparticle, the positron). Positronium preferentially traps in free-volume voids with the measured annihilation lifetime being related to the average void size. In this experiment, with films ranging from 200 nm to 600 nm in thickness, we employed an electrostatically focused beam of mono-energetic positrons in high vacuum [80] to restrict implantation to the target film and to avoid implantation in the supporting substrate. A positron beam implantation energy of 3.2 keV was determined to be optimal for these films.

The beam spectrometer uses a fast-timing system with a time resolution of 0.4 ns to measure the time difference between the implementation of positrons into the film and the eventual annihilation of the positronium. Data is acquired over one day with approximately 3 million events in the time histogram. The histogram is then fit to either a discrete set of positron and positronium lifetimes (and corresponding fractional intensities) [81] or a continuum distribution of lifetimes using the Laplace inversion program CONTIN [82]. Finally, using well-established methods [83], we convert the fitted lifetime continuum distribution into a pore diameter distribution for simple pore model shapes. The PALS experiments were done by Prof. David Gidley and Prof. Richard Vallery.

Nanoindentation experiments were carried out using a Hysitron TI-950 Triboindenter with a Berkovich probe. Films grown at 60 °C, 600 °C, 800 °C, and bulk a-SiO_2 sample were indented to peak loads in the range 300 μN to 400 μN at a constant loading rate of 200 μN/s. The peak loads were selected such that the maximum depths of the indents were less than 10% of the film thickness to avoid substrate effects. The samples were indented in an N_2 atmosphere at temperatures of 25 °C, 100 °C, 200 °C, 300 °C, and 400 °C to study the temperature dependance of their mechanical properties. After cooling back down to 25 °C, the samples were indented again to check if the changes in mechanical properties with increasing temperature were reversible. 15 indents were performed at each temperature. A Hysitron xSol stage was used to control the temperature of the samples during indentation. The hardness H and the reduced elastic modulus E were calculated from the load vs. displacement data using the Oliver-Pharr method [16].

Double-paddle oscillators (DPOs), made of 300 μm thick (100) high resistivity silicon, were used to measure the rigidity modulus or shear modulus G of 300 nm thick a-SiO_2 films grown at different temperatures. DPOs have an exceptionally small damping of the second antisymmetric mode that, operating at a resonant frequency of ~5500 Hz, yield very high quality factors at low temperature (Q ~ 10^8) [84]. Films were measured from 300 mK to room-temperature, and G was determined at room-temperature from the shift on the DPO resonance frequency after the film was deposited on [85]. The shear modulus measurements were carried out by Dr. Thomas Metcalf and Dr. Xiao Liu.

MD simulations were performed using the LAMMPS simulation package [22]. a-SiO_2 structures with varying densities were obtained by melting β-cristobalite at 8000 K and quenching to 300 K with a range of quench rates from 0.385 K/ps to 7700 K/ps. The details of the melt-quench procedure can be found in Ref.[86]. The interatomic forces were calculated using a Vashishta potential [87] which has been used extensively for studies of structure and mechanical properties of a-SiO_2 [86–90]. The evolution of the structure with temperature and the influence of ring size distributions on the thermally induced local reversible transitions in a-SiO_2 was then investigated by heating the melt-quenched structures in the constant pressure-constant temperature (NPT) ensemble.

4.3 Results and Discussion

Fig.4.1 shows the measured densities of a-SiO_2 films as a function of growth temperature (T_{Gr}). The density increases with increasing T_{Gr}, from 89% to 97% of the bulk a-SiO_2 density prepared by the conventional melt-quench method. ERDA measurements show that the H concentration in these films, due to water absorption, reduces from 6.2 at. % H to 1.7 at. % H for films grown at 60 °C and 900 °C, respectively. This reduction is attributed to a lower diffusivity of water molecules in the a-SiO_2 network as it becomes denser. One of the factors that affects the density of a-SiO_2 is the medium-range order, and it is usually characterized by the size distribution of rings in the network structure [91]. These rings are largely invisible to most experimental characterization tools, which makes it challenging to determine the ring statistics [92,93]. The other factor that influences the density of a-SiO_2 is porosity due to the presence of voids, particularly nanovoids, in the structure [94]. The sizes of voids and relative porosities in the a-SiO_2

films can be compared using PALS which is an excellent tool to probe the free volume in the form of nanovoids in materials.

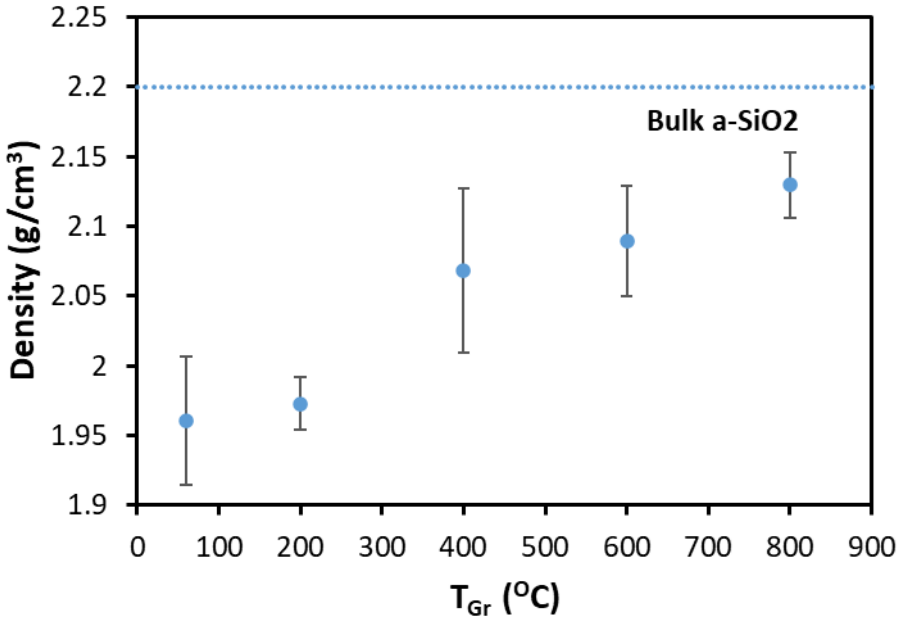

Fig. 4.1 Density of a-SiO_2 films determined using RBS in combination with profilometry. Bulk a-SiO_2 density from Ref.[95]*. Data from Dr. Manel Molina-Ruiz.*

Positronium lifetimes obtained by continuum fitting of PALS spectra using the program CONTIN are shown in Fig.4.2a. These distributions can be thought of as the normalized fraction of positronium decays that occur with lifetime τ between τ and τ+dτ. The area under the red curve for the a-SiO_2 film with T_{Gr} of 900 °C is arbitrarily taken to be unity and for sample comparison purposes the areas under the green (T_{Gr}=600 °C) and blue (T_{Gr}=60 °C) curves have been adjusted down from unity by the ratio of each spectrum's total positronium (Ps) formation intensity to that of the 900 °C grown sample. These ratios are 0.89 and 0.81, respectively. The area under each curve is thus a relative measure of the number of positronium annihilations in each spectrum which, together with positronium lifetime (related to pore size), can be used to estimate the relative porosity and pore size distribution for each sample.

Once we assume a pore shape model (in this case spherical pores for simplicity) we can convert each lifetime distribution into a corresponding pore size distribution (PSD). Using the techniques developed in Ref. [83], we have modified CONTIN to fit the lifetime histogram directly into a pore diameter distribution

as shown in Fig.4.2b. The fitting program includes the lifetime to pore diameter conversion plus one further refinement in that it incorporates and compensates for a pore size dependence in the trapping probability of Ps. Since Ps diffuses into pores through the pore surface, larger pores should have a higher Ps trapping probability than smaller pores and therefore larger pores, which have longer lifetimes, are over-represented in the lifetime distribution. The PSD fits shown in Fig.4.2b assume a trapping probability that is proportional to the surface area of a pore, which partially compensates for the increased volume with diameter in terms of relative porosity contribution. The three PSDs in Fig.4.2b are plausible fits to a spherical pore diameter distribution. As with the lifetime distributions, the area under the T_{Gr}=900 °C spectrum (nominally the porosity) is normalized to unity and the other PSDs are appropriately normalized (0.76 and 0.79 for T_{Gr}=60 °C and T_{Gr}=600 °C, respectively) as a good approximation for comparison of *relative* porosity. Even though it is challenging to determine *absolute* porosity in PALS, the technique is very useful for relative porosity comparisons of chemically similar materials such as the a-SiO_2 films in this study.

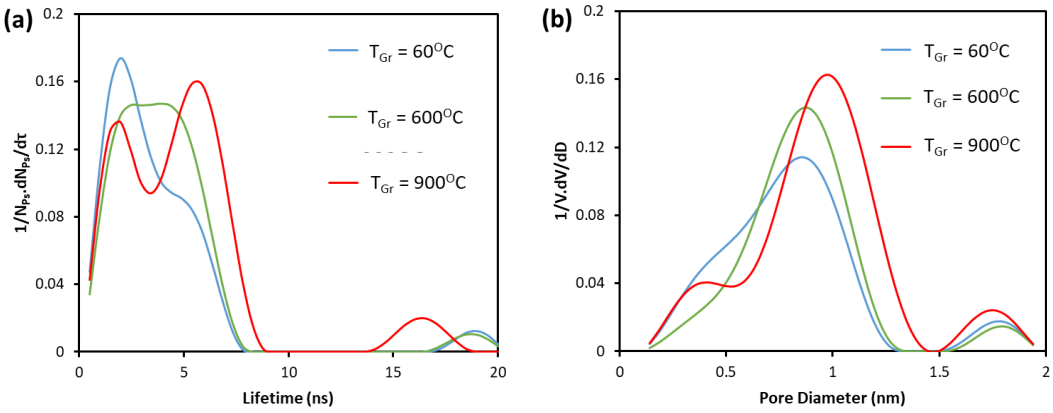

Fig. 4.2 (a) Positronium lifetime distributions for a-SiO_2 films grown at different temperatures fitted with the program Contin. (b) The relative pore volume distribution for a-SiO_2 films grown at different temperatures. Data from Dr. Richard Vallery and Dr. David Gidley.

As presented in Fig.4.2b, the spherical pore diameter ranges from about 0.2 nm to 2.0 nm. One of the limitations of CONTIN is that, technically, we cannot definitively distinguish whether there are 3 sharply defined void sizes or whether the film really has a broad continuum, however, in amorphous materials we would favor the latter interpretation. All three samples clearly have a dominant pore diameter D near 1.0

nm and well-resolved large diameter pores near 1.8 nm that, despite the larger volume, contribute less than 7% to the overall film porosity.

The trend of increasing positronium lifetime with increasing T_{Gr} is clear in Fig.4.2a. Although the trend in the pore diameter with respect to T_{Gr} in Fig.4.2b is not as clear, based on the normalized areas under the pore diameter distribution, there is still a trend of increasing pore volume fraction (or higher relative porosity) with increasing T_{Gr}. Specifically, the normalized areas are 0.76, 0.79, and 1.0 for T_{Gr} of 60 °C, 600 °C, and 900 °C, respectively. These trends both indicate that higher T_{Gr} leads to a higher porosity. The one caveat to this conclusion is that the fitted positronium intensity is more open to alternative interpretation than is the lifetime to pore size conversion. Positronium intensity can be strongly affected by film chemistry, which is independent of porosity, but in this case the films are chemically equivalent regardless of the different amounts of absorbed water found in films grown at different temperatures. For this reason, an equivalent set of Al capped films without absorbed water [77] was also measured with PALS. We obtained the same trends, which demonstrates that absorbed water does not alter the annihilation of Ps within the a-SiO_2 films. Therefore, it is reasonable to conclude that pore size and total pore volume increase with increasing growth temperature in PVD a-SiO_2 films.

The results from PALS may seem counterintuitive at first since one would expect lower porosity in the films with higher T_{Gr} due to the higher density measured in equivalent films. However, these results are similar to those reported by Ono *et al.*[96] in a PALS study on bulk a-SiO_2 glasses with varying densities associated with different quench rates. The authors found larger voids and increased volume of empty space in samples with a higher density. In a different study on the Raman spectra of bulk a-SiO_2, samples with higher densities, were found to have a higher fraction of smaller 3- and 4-membered network rings [97]. Based on this Raman study, Ono *et al.*[96] concluded that the presence of a denser network with a higher fraction of small 3- and 4-membered network rings compensated for the larger voids and resulted in a higher density in the samples. Similarly, we conclude that the a-SiO_2 network in our films becomes denser as T_{Gr} increases, which explains the increase in density, in spite of the (counterintuitive) increasing porosity. That means, the films with higher T_{Gr} have higher densities and a higher fraction of smaller rings in their network, despite having higher porosity.

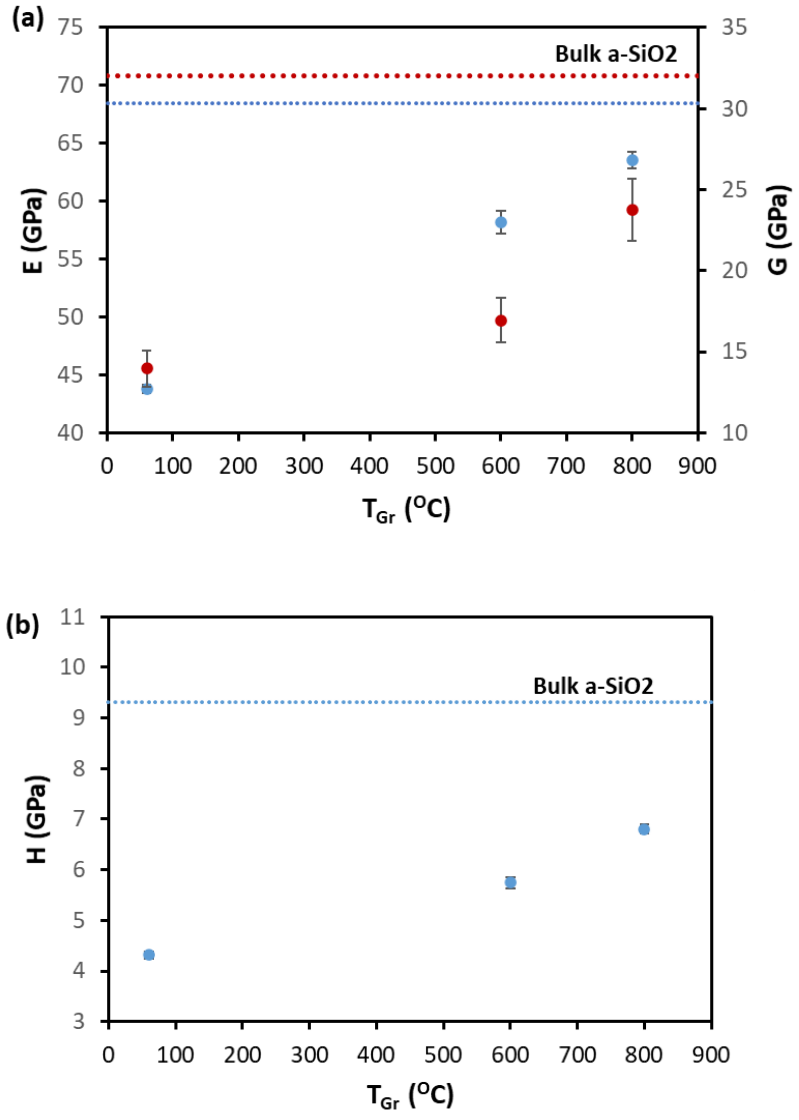

Fig. 4.3 (a) Elastic modulus E (blue) and shear modulus G (red) and (b) Hardness H of a-SiO_2 films as a function of growth temperature. E, G, and H were measured experimentally using nanoindentation and DPOs. Dotted lines indicate elastic modulus and hardness of bulk a-SiO_2 measured from nanoindentation and shear modulus from Ref.[98]. *Shear modulus data from Dr. Tom Metcalf and Dr. Xiao Liu.*

Elastic modulus E, shear modulus G, and hardness H of the a-SiO_2 films measured using nanoindentation and DPOs are shown in Fig.4.3a and Fig.4.3b. We observe that both moduli and the hardness of the a-SiO_2 films increase with increasing T_{Gr} but remain lower than that of bulk a-SiO_2. In order to explain this trend, we first consider the effect of porosity. It has been shown in spin coated silica films that the Young's modulus decreases with increasing porosity [99]. However, we see the opposite behavior

in our samples. That is, the films with a higher T_{Gr} have higher moduli despite having higher porosity. This result can be explained when we consider that the density of the films also increases with T_{Gr}, and the a-SiO_2 network becomes denser. The compactly packed rings in the denser network are more constrained and are expected to be more difficult to deform as compared to the larger network rings present in the films grown at lower temperatures, yielding higher elastic and shear moduli and hardness.

The elastic modulus of the a-SiO_2 films as well as the bulk a-SiO_2 sample as a function of the indentation temperature (T_{In}) is plotted in Fig.4.4a. Here, we find that the elastic modulus increases with increasing T_{In} in both the films and the bulk a-SiO_2. This kind of behavior is typical of a-SiO_2 and has been attributed to local, reversible transitions that take place in the silica network with increasing temperature[64]. These transitions resemble the alpha to beta transformation in cristobalite and involve rotation of Si-O-Si bonds about the Si-Si axis. The reversible transitions cause changes in the shape of the rings in the network structure of silica. The soft, asymmetric rings at lower temperatures transform into rigid, symmetric rings after the rotation of the Si-O-Si bonds. As a result, the ability to pivot about the Si-O bond is eliminated and subsequent elastic strains can only be accommodated by bending or stretching of bonds. These processes lead to an increase in the elastic modulus. Indentation of the samples after they had cooled down to room temperature showed that the elastic modulus returned to its initial value (Figure 5), confirming that the structural changes with increasing temperature were indeed reversible.

In contrast to the elastic modulus, hardness decreases with increasing T_{In} for all the samples (Fig.4.4b). This result is rather surprising since the network structure of silica becomes stiffer with increasing temperature due to the local reversible transitions. The reason for this trend in hardness is that hardness is defined as the resistance to indentation and depends on both elastic and plastic deformation in the material. While the changes in ring geometry affect the elastic response of a-SiO_2, plastic deformation is controlled by other factors. Specifically, during indentation, the plastic deformation in a-SiO_2 is dominated by densification [100]. This is in essence a displacive transformation involving the breaking and formation of new Si-O bonds, where the network structure collapses and becomes denser. The higher temperatures that induce local reversible transitions that make the a-SiO_2 network rings stiffer, also accelerate re-bonding and promote densification. The fact that the hardness is decreasing with T_{In} tells us that the accelerated

densification, which causes increased plastic deformation, has a larger impact on the overall deformation of the material compared to the local reversible transitions that increase resistance to elastic deformation.

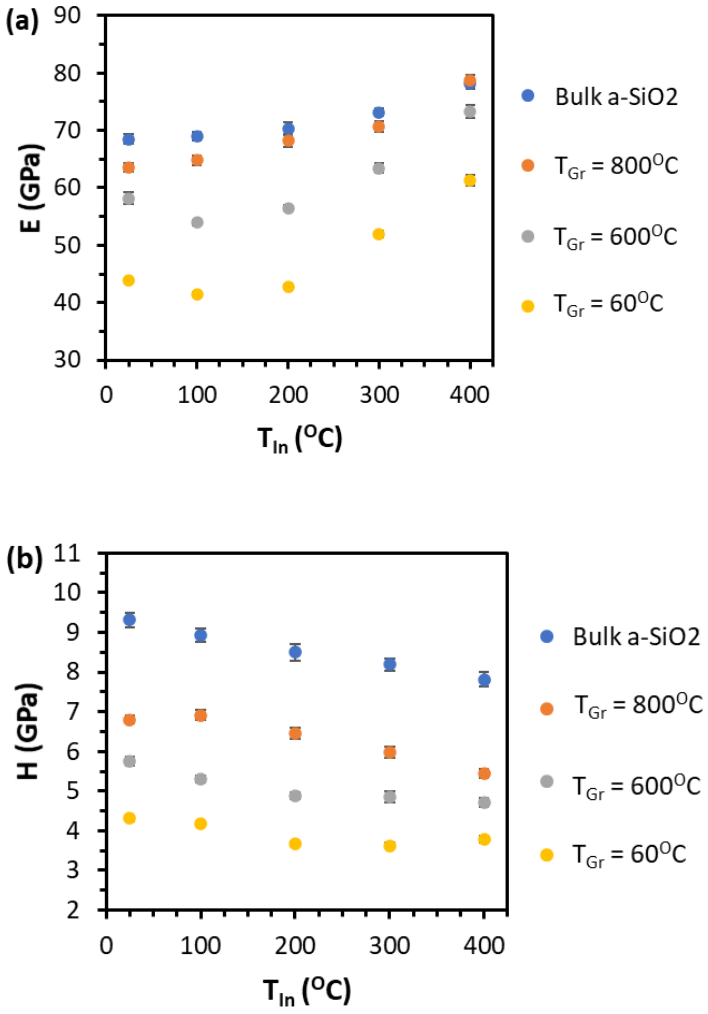

Fig.4.4 Experimentally measured change in the (a) elastic modulus and (b) hardness with indentation temperature T_{In} for a-SiO_2 films grown at different temperatures (T_{Gr}) and a bulk a-SiO_2 sample.

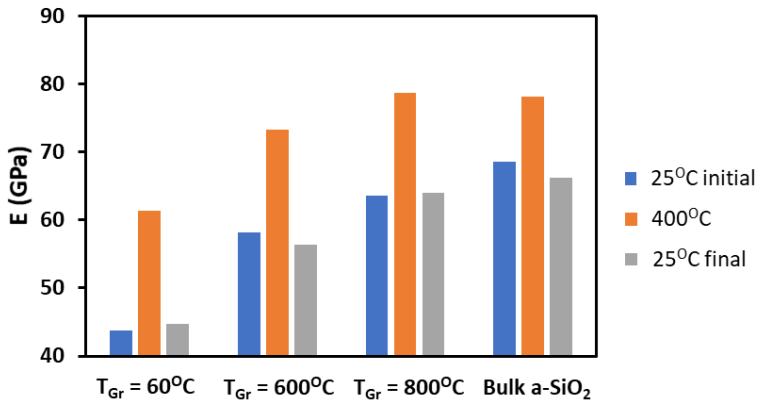

Fig. 4.5 Comparison of the elastic modulus before heating, after heating to 400 °C, and after cooling back down to room temperature.

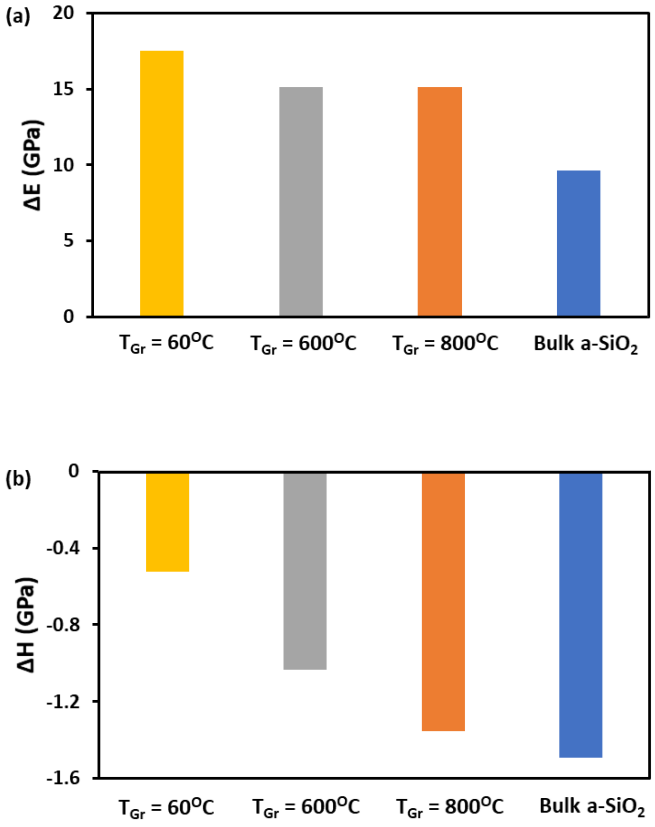

Fig.4.6 Experimentally measured changes in (a) elastic modulus ΔE and (b) Hardness ΔH when indentation temperature is increased from 25 °C to 400 °C.

Next, we look at how T_{Gr} affects the *rate of change* in the elastic modulus and in hardness with respect to T_{In}. In Fig.4.6a, we see that when T_{In} changes from 25 °C to 400 °C, the resulting change in the elastic modulus is the largest for the film grown with the lowest T_{Gr} and it decreases as T_{Gr} increases. The bulk a-SiO_2 sample shows the smallest increase in the elastic modulus. As explained earlier, the increase in the elastic modulus with the indentation temperature can be attributed to the local reversible transitions that lead to changes in the ring geometry. These transitions resemble the alpha to beta transformation in cristobalite silica and involve the rotation of Si-O-Si bonds in the silica rings. We hypothesize that the rotation of the Si-O-Si bonds becomes more constrained as the silica network becomes more compact and this results in fewer transitions in the structure and therefore a smaller increase in elastic modulus.

To verify our hypothesis, we analyzed thermally induced evolution of a-SiO_2 structures with different ring size distributions using MD simulations. We started with simulated quenching of molten SiO_2 over a range of quench rates from 0.385 K/ps to 7700 K/ps. We found that the potential energy per atom increased with the quench rate, resulting in structures with a lower stability (Fig.4.7a). However, the density of the melt quenched structures did not seem to show any dependance on the quench rate in the regime between 0.385 K/ps and 77 K/ps (Fig.4.7b). In fact, the densities in this regime were quite close to the experimentally measured density of bulk a-SiO_2. However, at quench rates beyond 77 K/ps, the density began to decrease and at 7700 K/ps, it became comparable to the experimentally measured density of the films grown at 600 °C and 800 °C. We then used the RINGS code [101] to compare the ring size distributions in the structures quenched at 77 K/ps and 7700 K/ps and found that the structure that had a higher density had fewer rings with 8 members or more (Fig.4.8a). These two structures are therefore suitable to test out our hypothesis regarding the effect of the network ring sizes on the thermally induced local reversible transitions in a-SiO_2. To study this effect, we heated the two melt-quenched structures up to a temperature of 800 °C and we tracked the rotation of the Si-O-Si bonds about the Si-Si axis using the plane normal correlation defined in Ref.[64]. The plane normal correlation is defined as the dot product between the normal to the plane of the Si-O-Si bond at a reference temperature and any other temperature. For example, if we take the reference temperature to be 25 °C, the plane normal correlation at 25 °C will be equal to 1. As the temperature increases and the Si-O-Si bonds start to rotate, the plane normal correlation will start decreasing. The changes in the plane normal correlation, while going from 25 °C to 800 °C for the structures quenched at

77 K/ps and 7700 K/ps, are shown in Fig.4.8b. We can see that the plane normal correlation drops at a much faster rate with increasing temperature in the case of the 7700 K/ps quenched structure than for the sample quenched at 77 K/ps. That is, the structure which has a lower density and larger network rings has a higher propensity to undergo the local reversible transitions involving the rotation of Si-O-Si bonds. As a result, such a structure is bound to exhibit a larger increase in elastic and shear moduli. This finding from MD simulations confirms our initial hypothesis that the rotation of the Si-O-Si bonds becomes more constrained as the silica network becomes denser and this results in fewer transitions in the structure and therefore a smaller increase in the elastic modulus.

When we look at how T_{Gr} affects the rate of the change in hardness with respect to T_{In} in our experiments (Fig.4.6b), we can see that the change in hardness in going from T_{In}=25 °C to T_{In}=400 °C is the smallest for the film grown with the lowest T_{Gr} and it increases as T_{Gr} increases. The bulk a-SiO_2 sample shows the largest drop in hardness. This is the opposite trend to what we found for the elastic modulus (Fig.4.6a). To explain this trend in hardness, we need to go back to the discussion of the competing effects of densification and the local reversible transitions on the deformation of a-SiO_2. The thermally activated densification process accelerates plastic deformation while the local reversible transitions that is most pronounced at higher temperatures result in stiffer network rings, which are more resistant to elastic deformation. When discussing the decrease of hardness with an increasing nanoindentation temperature T_{In} (Fig.4.5), we concluded that the effect of densification on the overall deformation of the samples was larger than the effect of local reversible transitions. However, we have just shown through MD simulations (Fig.4.8a and Fig.4.8b) how the local reversible transitions take place to varying degrees in the glasses depending on their density and ring size distribution. This means that the propensity for undergoing these reversible transitions will be higher in the a-SiO_2 films grown at lower temperatures due to the larger network rings. This in turn implies that the increase in stiffness of the network rings due to the reversible transitions is higher in the films with lower T_{Gr} and compensates for the drop in hardness that would arise from the increased rate of densification. On the other hand, the increase in stiffness of the network rings in films with higher T_{Gr} is not sufficient to compensate for the increased rate of densification and we see a larger drop in their experimentally measured hardness.

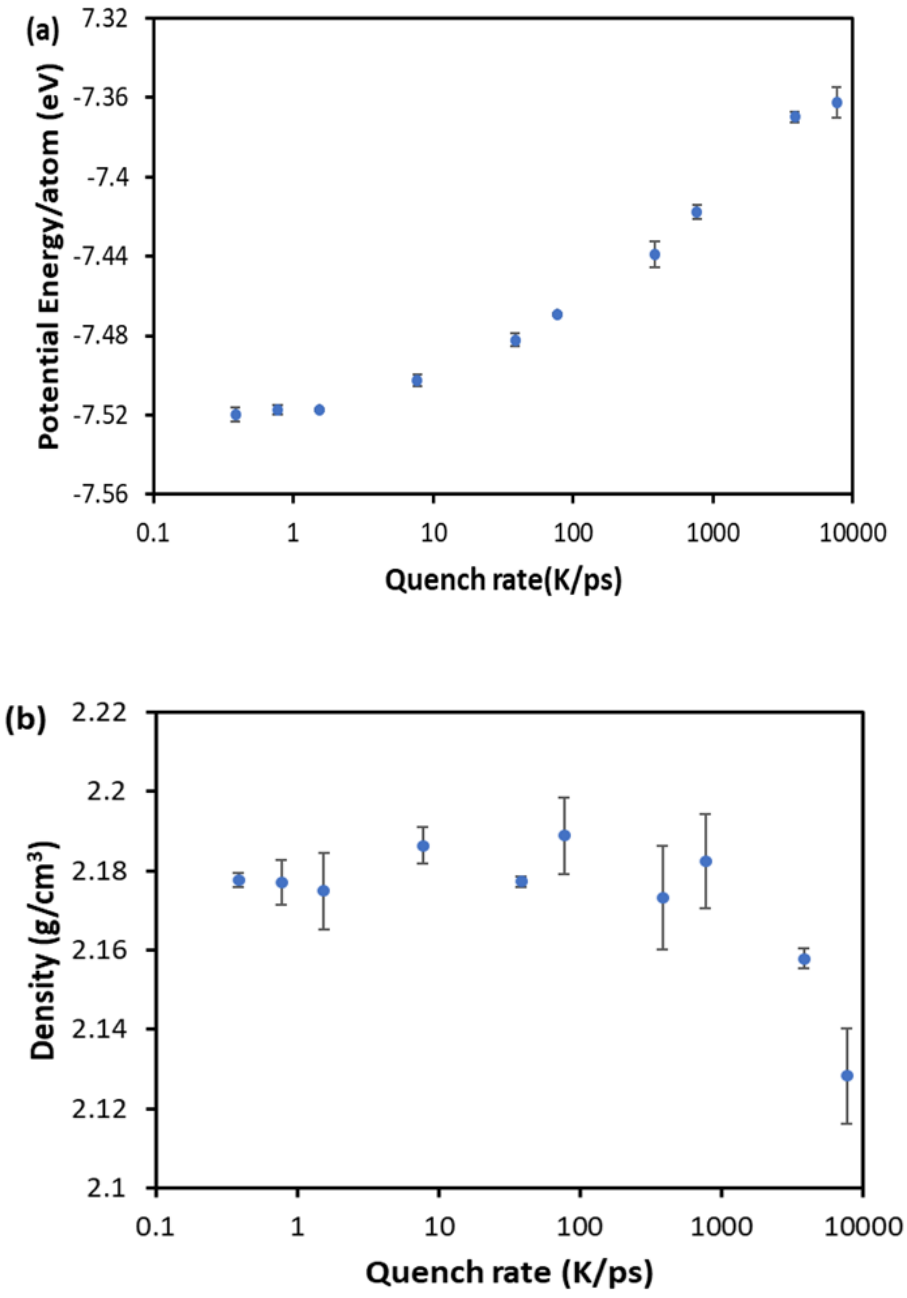

Fig. 4.7 (a) Potential energy per atom and (b) density of melt-quenched a-SiO_2 as a function of the quench rate from MD simulations.

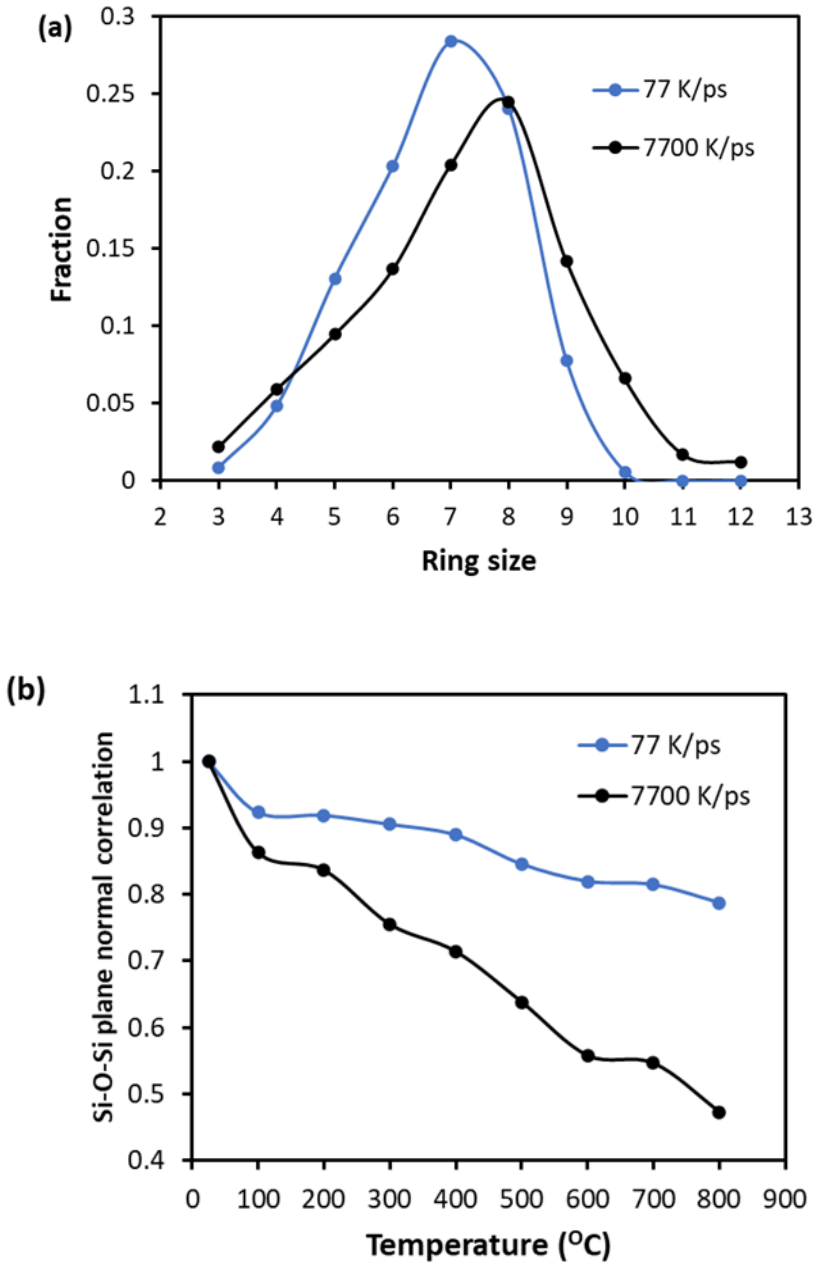

Fig.4.8 (a) Ring size distributions for melt-quenched a-SiO_2 structures from MD simulations, determined by R.I.N.G.S code. (b) Si-O-Si plane normal correlation as a function of temperatures for melt quenched structures with different cooling rates from MD simulations.

4.4 Conclusions and Outlook

We have used physical vapor deposition to access a range of different structures in a-SiO_2 and shown the relationships between structure and mechanical properties, which is supported by MD simulations. We have shown that there are nanovoids present in the films whose size and overall porosity increase with increasing growth temperature. This finding combined with the observed increase in density suggests that the a-SiO_2 network may become more compact with smaller rings as the growth temperature increases. We have also shown that the above changes in the structure of a-SiO_2 with increasing growth temperature result in higher elastic and shear moduli and higher hardness. These changes in mechanical properties have been attributed to the increase in density of the a-SiO_2 films. Furthermore, we have demonstrated that the vapor deposited a-SiO_2 films exhibit an anomalous increase in the elastic modulus with increasing indentation temperature similar to bulk a-SiO_2. However, the rate of change in the elastic modulus is found to depend on the growth temperature. We attribute this trend to the effect that the increase in density of the a-SiO_2 network has on the local structural transitions, which in turn are responsible for the anomalous increase in elastic and shear moduli with temperature.

While this study provides fundamental insights into the structure-mechanical property correlations in a-SiO_2, it does not consider the influence of the growth temperature on the stability of the a-SiO_2 films. It has been demonstrated that molecular glasses and metallic glasses deposited at high substrate temperatures close to T_g exhibit higher density and stability than quenched glasses [26,27]; however, a-SiO_2 films, despite being deposited at temperatures as high as $0.8T_g$, show lower density than the quenched glass. This discrepancy could be attributed to the fact that a-SiO_2 is a strong glass with surface mobility comparable to its bulk mobility [102]. As the increased stability in vapor-deposited glasses is believed to originate from higher surface atom mobility, it is logical to conclude that the stability of strong glasses like a-SiO_2 will not be significantly affected by the vapor deposition process. In essence, vapor deposition in strong glasses is akin to quenching at extremely high rates, which explains the observed lower densities in the vapor-deposited a-SiO_2 films when compared to bulk a-SiO_2 samples cooled more slowly from the liquid state.

However, as established in the previous chapter, ion beam assisted deposition (IBAD) can effectively enhance surface mobility without altering the substrate temperature or deposition rate during the vapor deposition process. This raises the intriguing question of whether IBAD could be utilized to improve surface atom mobility in a-SiO_2. The challenge lies in overcoming the higher threshold displacement energies in a-SiO2 without implanting ions in the film. A potential approach may involve using high ion beam energies at grazing incidence. If successful, this process could mark a significant breakthrough in the synthesis of a-SiO2 coatings with low room temperature internal friction, which is crucial for mirrors in gravitational wave interferometers where internal friction acts as a primary source of noise and limits sensitivity [103].

5. Minor alloying of metallic glasses: Role of topology and chemical bonding

This chapter is adapted from the paper: V. Jambur, C. Tangpatjaroen, J. Xi, J. Tarnsangpradit, M. Gao, H. Sheng, J.H. Perepezko, I. Szlufarska, Effect on minor alloying on the mechanical properties of Al based metallic glasses, Journal of Alloys and Compounds, 854, p.157266 (2020).

5.1 Introduction

The unique combination of high strength and elasticity of metallic glasses (MGs) has attracted a lot of attention since the discovery of these materials [2,104]. Several MGs with a wide range of compositions have been synthesized to date [105] and minor alloying has emerged as common way to manipulate their mechanical properties [106–115]. It is therefore important to understand how small amounts of alloying elements can have such a strong influence on the mechanical behavior of MGs.

Unlike crystalline metals, the mechanical response of MGs is not controlled by discernible structural features such as dislocations, stacking faults, and grain boundaries. The carriers of deformation in metallic glasses are called shear transformation zones (STZ) [116]. These are local clusters of atoms that undergo an inelastic shear distortion to accommodate plastic strains during deformation. STZs percolate along the planes of the maximum shear stress in the sample and eventually form regions of localized deformation called shear bands [104,117]. The activation of STZs and formation of shear bands is influenced by the atomic level structure in the MGs.

Even though MGs lack long-range structural order, they possess short- and medium-range orders, which can influence mechanical properties. Shi and Falk [118] studied the mechanical response of a binary metallic glass using the Lennard-Jones potential and proposed that metallic glasses derived their strength from a backbone of atoms with local short-range order (SRO). This report was followed by several other studies that investigated the influence of the atomic structure on the mechanical behavior of a more realistic system such as Cu-Zr and confirmed that indeed these MGs derived their mechanical strength from local SRO [108,119–128]. Atoms arranged in icosahedral clusters were shown to be more resistant to shear transformations than other groups of atoms with geometrically unfavored motifs (GUMs). The GUMs are disordered regions with liquid like structure and act as soft spots with a lower resistance to shear

transformations and fertile sites for activation of STZs [129,130]. A higher fraction of icosahedral clusters in the structure was therefore associated with a higher resistance to plastic deformation.

The effects of chemical bonding on the mechanical behavior of metallic glasses have been studied in the context of MGs with significant fractions (~20% or more) of metalloids [131–133]. For example, in Pd-Si MGs, the covalent bonds associated with Si atoms were found to be more difficult to break than metallic bonds associated with Pd atoms. Since the fraction of Si atoms is significant in these alloys, Si atoms can suppress cavitation in Pd-Si, promoting a larger fracture toughness [131].

The effects of minor (i.e., on the order of a few percent) alloying elements on mechanical properties of MGs have been typically explained in terms of the effect that minor elements have on the atomic configurations and the topological order [107–111,113,114]. For instance, the addition of small amounts of Al to Cu-Zr MGs has been shown to increase the resistance to plastic flow due to the strong, covalent-like bonding between Cu and Al atoms, which in turn leads to shortening of Al-Cu bond lengths and an increase in the icosahedral order [108]. In other words, the effect of the chemical bonding has been conflated with the increased topological order.

The goal of this work is to understand the role of minor alloying in the strengthening of Al rich MGs. Our interest in these MGs is motivated by their light weight, high specific strength [134,135], good corrosion resistance [136], and thermoplastic forming ability [137], which makes them excellent candidates for applications in such areas as micro- and nano-scale devices [137], wear and corrosion resistant coatings [138], composites with excellent mechanical and tribological properties [139]. We have chosen Al-Sm based glasses alloyed with different transition metals (TM = Cu, Ag, Au) for this study. The Al-Sm based glasses serve as a good model system since they are one of the better understood Al-based glasses [137,140–143] and have been previously shown to possess good GFA and good stability due to the icosahedral SRO [142]. We have found that minor alloying of Al-Sm with TMs increases the strength of the MG, but this effect is due to the change in the chemical bond strength alone and cannot be explained by changes in topological order. In fact, we found that the effects of topology and the chemical bond strength are independent of each other in controlling the mechanical response of MGs subjected to minor alloying. Mechanical properties of the Al-Sm based glasses have been investigated experimentally using nanoindentation. The experiments

are complemented by a detailed analysis of the atomic level structure using classical as well as *ab initio* molecular dynamics (MD).

5.2 Materials and Methods

Classical molecular dynamics (MD) simulations were carried out with LAMMPS software package [22]. Embedded Atom Method (EAM) potential for Al-Sm-Cu ternary system was developed specifically for this study. Amorphous structures of $Al_{92}Sm_8$ and $Al_{90}Sm_8Cu_2$ were obtained by starting out with an FCC crystal lattice containing ~11000 atoms with periodic boundary conditions in all three directions. The atoms were assigned random initial velocities from a Gaussian distribution and equilibrated in the constant energy – constant volume (NVE) ensemble at a temperature of 300K for 20ps. The system was then equilibrated in the constant pressure – constant temperature (NPT) ensemble at 300K for another 200ps. This was followed by heating to a temperature of 2000K in the NPT ensemble followed by equilibration for 2ns. The melted sample was then quenched down to a temperature of 50K in the NPT ensemble. The quenching was carried out in steps of 50K with a cooling rate of 10^{10}K/s. The melt quenched samples with dimensions of ~ 6nm x 6nm x 6nm were replicated to obtain larger samples with dimensions ~ 120nm x 120nm x 6nm, containing ~4.5 million atoms. The replicated samples were then equilibrated at 50K for 100ps. This was followed by uniaxial tensile deformation at a constant strain rate of $2x10^7$/s at 50K. OVITO [144] software was used for Voronoi analysis and, calculation of atomic strains and non-affine displacements in the classical MD samples.

Ab initio molecular dynamics (AIMD) simulations were performed in the framework of the density functional theory (DFT) using the Vienna Ab-Initio Simulation Package (VASP) [145]. Projector-augmented-wave (PAW) potentials [146] were used to mimic the ionic cores, while the generalized gradient approximation (GGA) in the Perdew-Burke-Ernzerhof (PBE) [147] approach was employed for the exchange and correlation functional. The integration over the Brillouin zone was performed using the Γ point for AIMD simulations. To prepare a model of glassy alloys for the AIMD simulations, we first created a glassy $Al_{92}Sm_8$ system with 256 atoms using classical MD simulations; the settings of the classical MD simulations are discussed elsewhere[148]. After that, we substituted Al with X=Ag, Au, and Cu by randomly replacing atoms in the liquid phase to obtain the exact composition, up to 2% of the minor alloying elements.

The resulting configurations were further equilibrated in AIMD at 1300 K for 3 ps in the constant volume – constant temperature (NVT) ensemble with the Nose-Hoover thermostat and a time step of 3 fs. Afterwards, the systems were subsequently cooled down to 300 K. The equilibrium volume at particular temperature was obtained by constructing pressure-volume (*P-V*) equation of state [149]. After determining the volume, the samples were equilibrated for 15 ps at 300 K with their equilibrium volumes. 20 melt quenched samples with different initial atomic configurations were prepared for each sample to obtain statistically relevant results. In order to improve statistics, in these isothermal simulations, the first 12 ps of the simulation had been treated as the equilibration period run, whereas the remaining steps were treated as the production run to calculate the average values of icosahedral fraction using the Voronoi analysis tool in OVITO [144].

We used DFT calculations to determine the force constant for one specific atom with its surrounding environment. Based on the harmonic approximation, the force constant can be described through the equation of $k = m_X f^2$, here k is the force constant, $m_X$is the atomic mass of the doping atom (X=Cu, Au, and Ag), and f is the vibrational frequency. Vacancy formation energy for atom X is calculated through the equation of $E_f^X = E_{defect} - E_{perfect} + \mu_{atom,X}$. Here, E_f^X is the energy cost for the formation of one isolated X atom, and E_{defect} and $E_{perfect}$ are the system with and without X vacancy, respectively. $\mu_{atom,X}$ is the isolated atomic energy, which is calculated by inserting one X atom into a vacuum box. Ab initio MD and DFT calculations were performed by Dr. Jianqi Xi.

Four Al-Sm based metallic glass compositions were selected for this study - $Al_{92}Sm_8$, $Al_{90}Sm_8Cu_2$, $Al_{90}Sm_8Ag_2$, and $Al_{90}Sm_8Au_2$. All precursors were prepared using arc melter method in an argon atmosphere. The pure elements for each composition were melted and stirred together at least five times to ensure homogeneity. The chemical composition of the ingots was confirmed by Energy Dispersive Analysis (EDS, scanning electron microscope Zeiss LEO 1530). Following this, the precursors were subjected to melt spinning on a copper wheel at the wheel speed of 55m/s, in an argon atmosphere to produce MG ribbons. The chemical composition of the ribbons was also confirmed by EDS. The amorphous structure of the as-spun ribbons was ascertained by X-ray diffraction (Bruker D8 Discover Diffraction with Cu Kα radiation). The ribbon samples were prepared by Dr. Meng Gao.

For nanomechanical testing, the MG ribbons were placed in a custom-made aluminum mount and polished mechanically using abrasive SiC grit paper followed by 1 μm diamond suspension. The hardness

of the samples was evaluated using the Hysitron TI 950 TriboIndenter equipped with a diamond Berkovich tip probe. A series of indents (120 – 130 for each composition) were performed, with a 200 μN/s loading rate, a 2 s hold at the maximum load, and a 200 μN/s unloading rate, with the maximum loads ranging from 900 to 2400 μN. Continuous stiffness measurement using Bruker nanoDMA III transducer in CMX mode was done to measure the hardness as a function of the indentation depth. The measurement was done at a constant strain rate and a frequency of 220Hz. The sample was loaded to a peak load of 10mN.

5.3 Results and Discussion

Before looking into the effects of minor alloying on the mechanical properties of Al-Sm MGs, we determine what controls the mechanical behavior of binary Al-Sm glasses using classical MD simulations. Melt quenched samples with compositions $Al_{90}Sm_{10}$, $Al_{92}Sm_{8}$, and $Al_{94}Sm_{6}$ were prepared using the procedure described in section 5.2 and the structure was studied using Voronoi analysis. In this technique, each atom is considered as a center of a Voronoi polyhedron (VP) and assigned Voronoi indices that describe shapes of the VP faces. In all three Al-Sm samples considered in our study, the majority of VPs that are centered on Al atoms were found to have indices <0,0,12,0> and <0,1,10,2>. While VPs with indices <0,0,12,0> represent full icosahedral SRO, <0,1,10,2> can be considered distorted icosahedral SRO. Distorted icosahedra refer to VPs with a large number of fivefold bonds with coordination numbers close to 12, such as <0,1,10,2>, <0,2,8,2>, and <0,2,8,1> [7]. We calculated the fraction of VPs with more than 8 pentagonal faces and coordination numbers in the range 11-13 as a measure of the degree of icosahedral order and found that it increases monotonically with the atomic fraction of Sm in the alloys.

The three alloys were then subjected to uniaxial tensile deformation to obtain tensile stress – strain curves (Fig.5.1a). The peak stress in these curves corresponds to the resistance to the initiation of plastic flow. We can see that the peak stress increases with the increasing degree of icosahedral order (Fig.5.1b). After the stress reaches its peak value, it drops to a relatively constant flow stress in all the samples. The flow stress corresponds to the resistance to plastic flow offered by the rejuvenated/disordered structure in the shear bands. The difference between the peak stress and the flow stress represents the difference in the strengths of the initial structure with icosahedral order and the rejuvenated structure in the shear bands. This difference is an indicator of the propensity for localization of deformation [108]. As shown in Fig.5.1a,

the drop in the stress value is the largest in the case of $Al_{90}Sm_{10}$, followed by $Al_{92}Sm_8$. The change from the peak stress to the flow stress in $Al_{94}Sm_6$ seems more gradual. This indicates that $Al_{90}Sm_{10}$ has the largest propensity for localization of deformation, followed by $Al_{92}Sm_8$, and then $Al_{94}Sm_6$. The difference in the degree of localized deformation in $Al_{90}Sm_{10}$ and $Al_{94}Sm_6$ can be seen in Fig5.2. These results show that a higher degree of icosahedral order leads to a higher resistance to plastic flow and a higher propensity for localized deformation in binary Al-Sm alloys, consistent with what has been previously reported in Cu-Zr alloys [108,124].

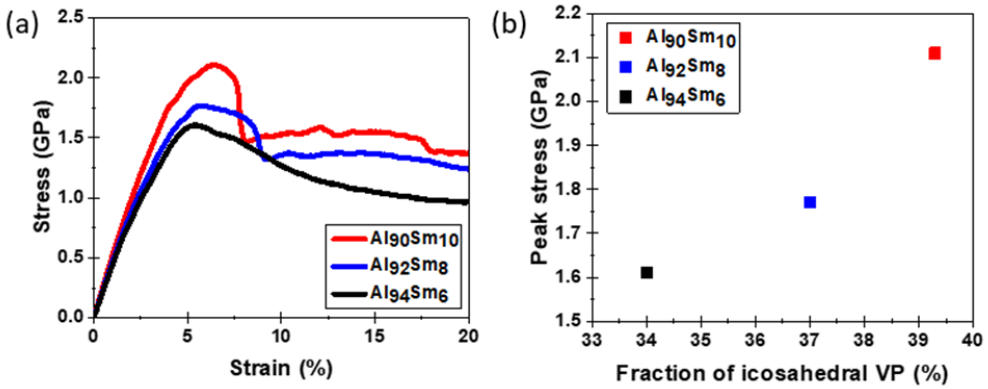

Fig. 5.1 Mechanical response of binary Al-Sm MGs. (a) Simulated tensile stress strain curves for binary Al-Sm MGs at 50K. (b) Correlation between peak stress and the fraction of icosahedral VP in the binary Al-Sm alloys.

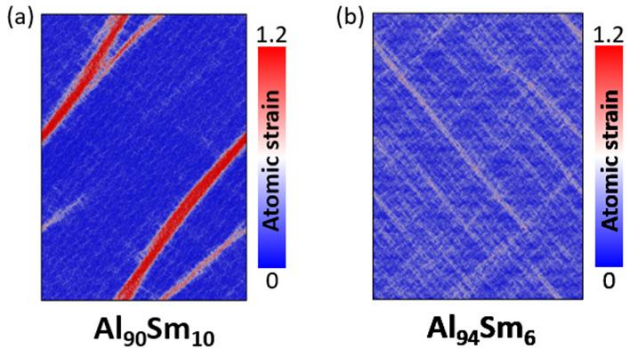

Fig. 5.2 Atomic strains during tensile deformation of (a)$Al_{90}Sm_{10}$ and (b)$Al_{94}Sm_6$.

The effects of minor alloying with TM on mechanical properties have been first studied experimentally. Three different TMs (Cu, Ag, Au) were substituted in place of Al in $Al_{92}Sm_8$ to obtain alloys with compositions $Al_{90}Sm_8Cu_2$, $Al_{90}Sm_8Ag_2$, and $Al_{90}Sm_8Au_2$. Experimental ribbon samples with the above

compositions were prepared by melt spinning and the presence of amorphous structure was confirmed using x-ray diffraction. Nanoindentation experiments were performed on the melt – spun ribbon samples to determine hardness and elastic modulus using the Oliver – Pharr method [16] (Fig5.3a). The hardness of the ternary compositions with minor amounts of TMs was significantly higher than that of the binary alloy. However, the elastic modulus appeared to be lowered after minor alloying. Measurement of the elastic modulus as a function of the indentation depth using the continuous stiffness method (CSM) [150] revealed that the elastic moduli of the ternary compositions were initially slightly higher than that of the binary alloy. However, the modulus decreases rapidly with an increasing indentation depth and eventually crosses over with the elastic modulus of the binary alloy (Fig.5.3b). This means that the ternary alloys experience more strain-induced softening than the binary alloy. The same behavior was also seen in the hardness measured using the CSM method, but the initial difference in hardness between the ternary alloys and the binary was too large for them to cross over due to softening (Fig.5.3c). The large hardness in the ternary alloys is indicative of a higher resistance to plastic flow, whereas the more pronounced softening means that there is more localized deformation. The effect of minor alloying appears similar to the effect of increasing the degree of icosahedral order in the binary Al-Sm alloys and our first hypothesis is that the TMs increase the icosahedral order in the Al-Sm alloys. This hypothesis can be tested using atomistic simulations.

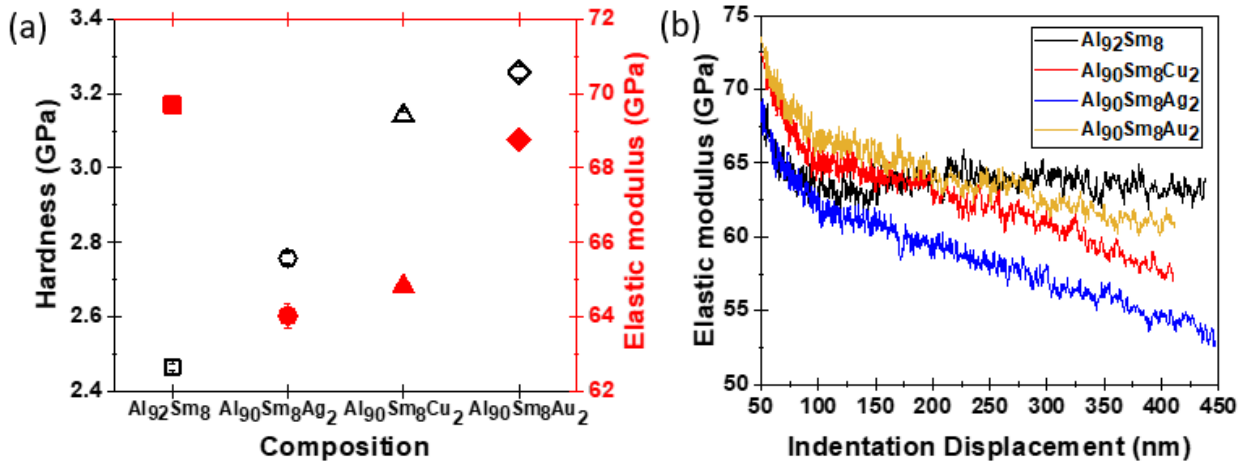

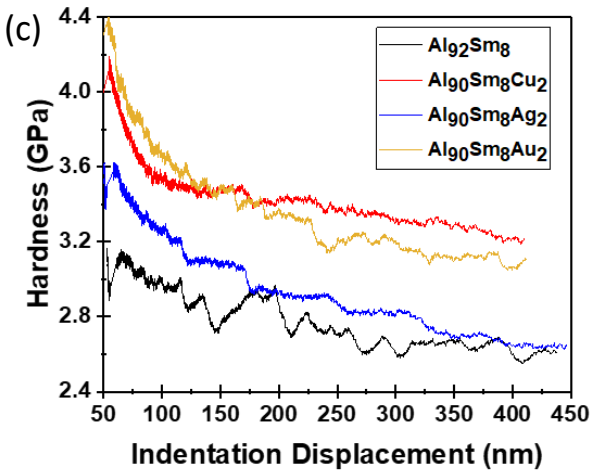

Fig 5.3 Effect of TM addition on mechanical response of Al-Sm MGs. (a) Experimentally measured nanoindentation hardness (black, open symbols) and elastic modulus (red, closed symbols) for $Al_{92}Sm_8$, $Al_{90}Sm_8Ag_2$, $Al_{90}Sm_8Cu_2$, and $Al_{90}Sm_8Au_2$ ribbon samples (b) Elastic modulus and (c) Hardness as a function of the indentation depth measured using the continuous stiffness method (CSM).

To investigate the effect of the TMs on the atomic-level structure of Al-Sm MGs, we prepared melt-quenched structures of $Al_{92}Sm_8$, $Al_{90}Sm_8Ag_2$, $Al_{90}Sm_8Cu_2$ and $Al_{90}Sm_8Au_2$ alloys using *ab initio* MD simulations based on the density functional theory (DFT). After quenching to 300K, we performed Voronoi analysis to find the most common VP in the four alloys (Fig.5.4a). We observed that minor alloying did not have a large effect on the atomic level structure of the MGs. We then calculated the degree of icosahedral ordering in the four alloys using the same criteria as we have used earlier to analyze binary Al-Sm alloys prepared in classical MD simulations. We found that the increase in hardness with minor alloying could not be explained based on the changes in the amount of icosahedral ordering in the structure (Fig.5.4b). In addition, the local topological order around the different TM atoms was found to vary, depending on the size of the TM atoms but this trend still does not explain the measured changes in mechanical properties of the MGs. To understand the effect of minor alloying, it is therefore necessary to analyze the mechanical behavior of these MGs at the atomic level.

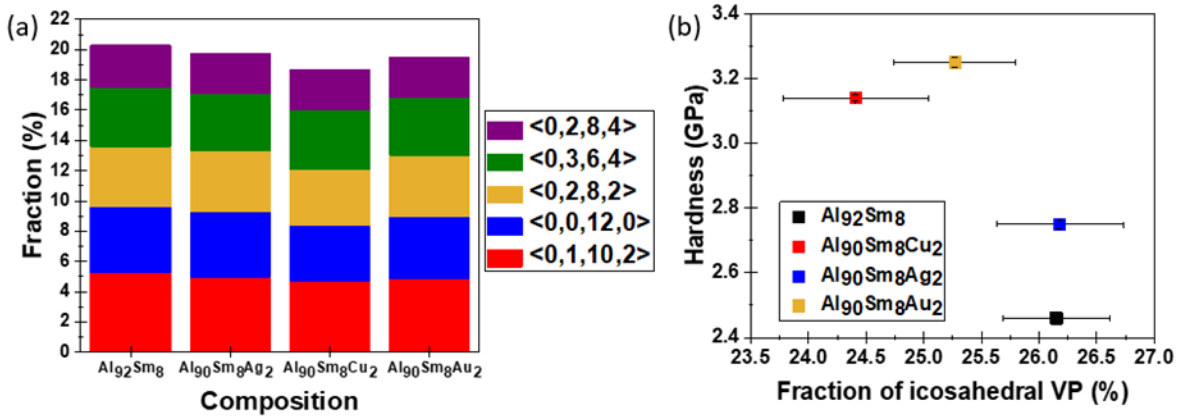

Fig.5.4 Effect of TM addition on topological short-range order in Al-Sm MGs. (a) Most common VP in the Al-Sm-TM MGs at 300K obtained from ab initio MD simulations. (b) Experimental nanoindentation hardness plotted against the fraction of icosahedral VP at 300K.

Classical MD simulations of tensile deformation were carried out on melt-quenched $Al_{90}Sm_8Cu_2$ to study the effect of TM atoms on the mechanical response of the Al-Sm-TM MGs. The tensile stress – strain curves of the binary $Al_{92}Sm_8$ and $Al_{90}Sm_8Cu_2$ are plotted in Fig.5.5a and they show that $Al_{90}Sm_8Cu_2$ has a higher peak stress and a higher drop in stress from peak stress to the flow stress than the binary. This means that the ternary has more resistance to plastic flow and more localized deformation, which is consistent with the conclusion drawn from the nanoindentation experiments. This agreement between MD simulations and experiments further validates the use of our EAM potential for analysis of the role of TM in deformation of Al-Sm-TM glasses. Furthermore, we have performed the Voronoi analysis on samples generated from classical MD simulations and found that while the icosahedral order was still dominant in the ternary $Al_{90}Sm_8Cu_2$ alloy, the degree of icosahedral order was lower than that in the binary $Al_{92}Sm_8$ alloy. This trend is consistent with the results from *ab initio* calculations shown in Fig.5.3b.

At the atomic scale, a higher resistance to plastic flow can be attributed to a higher resistance to the activation of STZs, which are the carriers of plastic deformation. In order to determine the reason for a higher resistance to the activation of STZs in the $Al_{90}Sm_8Cu_2$ system, we used the non–affine squared displacement (D^2_{min})[116] parameter to identify those atoms that underwent local irreversible shear transformations to form STZs. We have subsequently identified the 5% of atoms in the sample that have

the highest and the lowest D^2_{min} at various stages during tensile deformation. We found that the atoms with the highest D^2_{min} were all concentrated along a single plane that constituted the shear band (Fig.5.5a inset), whereas the atoms with the lowest D^2_{min} were distributed uniformly outside the shear bands. Among the 5% of atoms with the highest D^2_{min}, the fraction of Cu atoms was found to be lower than the overall fraction of 2%. At the same time, among the 5% of atoms with the lowest D^2_{min}, the fraction of Cu atoms was found to be significantly higher than the overall fraction of 2% (Fig.5.5b). These results indicate that Cu atoms have a lower propensity to undergo local shear transformations as compared to Al and Sm atoms. Therefore, clusters of atoms containing Cu offer more resistance to the activation and percolation of STZs to form shear bands, which in turn leads to higher strength and hardness.

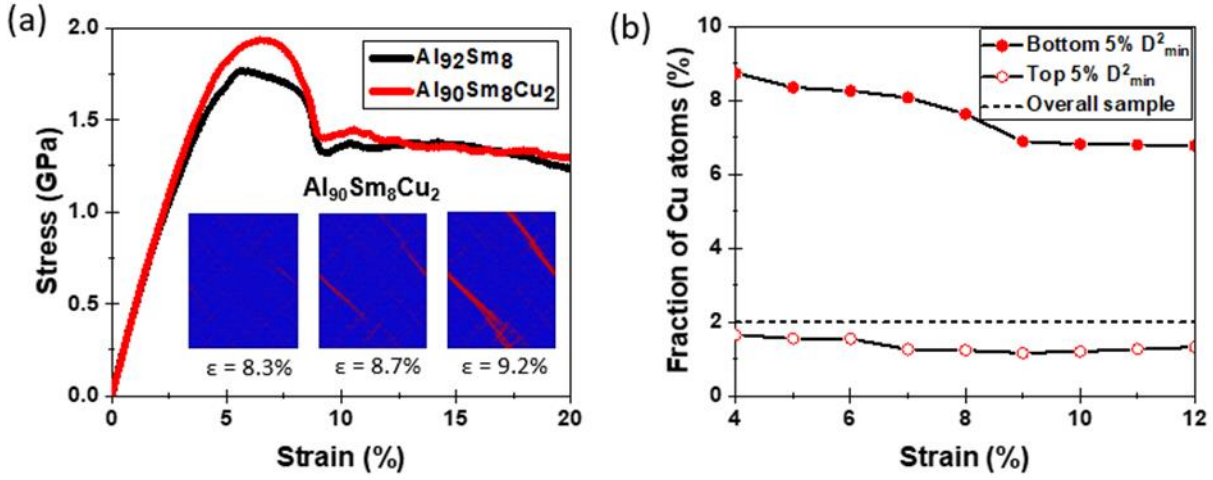

Fig.5.5 Role of Cu in mechanical behavior of Al-Sm MGs. (a) Tensile stress – strain curves for $Al_{92}Sm_8$ and $Al_{90}Sm_8Cu_2$ from MD simulation at 50K; Inset: Non affine squared displacement (D^2_{min}) map showing formation of shear band in $Al_{90}Sm_8Cu_2$ (Red atoms are the 5% of atoms with the highest D^2_{min} values). (b) Fraction of Cu among the 5% of atoms with the lowest and highest D^2_{min} values compared with the overall fraction of Cu.

To answer the question of why Cu atoms provided more resistance to shear transformations, we first considered the influence of topological order around the Cu atoms. The most common types of VPs around Cu atoms are shown in Fig.5.6a. Unlike Al atoms, the smaller Cu atoms are dominated by distorted icosahedral VP with indices <0,2,8,1>, followed by VPs with indices <0,2,8,0>, which are sometimes referred to as bi-capped square Archimedean antiprism (BSAP) [7]. The two most common VPs centered

on Cu atoms have coordination numbers of 11 and 10, respectively. The distorted icosahedral VP with indices <0,2,8,1> and BSAP with indices <0,2,8,0> are known to be the most stable and efficiently packed VP for their respective coordination numbers [7]. We next looked at the mechanical response of these two types of VPs to see if they had any influence on the propensity of Cu atoms to undergo local shear transformations. For this purpose, we compared the fractions of these VPs among Cu atoms that were part of the bottom 5% of D^2_{min} values with the overall fraction of these VP among all the Cu atoms in the samples and we found these fractions to be almost the same (Fig.5.6b). In contrast, a similar comparison for dominant Al centered VPs (with indices <0,0,12,0> and <0,1,10,2>) showed that their fraction among the bottom 5% of D^2_{min} values was significantly higher than the overall fraction of these VPs in the sample. This means that while the Al atoms with icosahedral SRO were more resistant to shear transformations than other Al atoms (Fig.5.6c), the SRO does not play the same role in the case of Cu atoms. In other words, the topological order does not have any significant influence on the resistance to deformation provided by Cu atoms in $Al_{90}Sm_8Cu_2$, but the topological order plays a key role in determining the resistance to deformation provided by Al atoms in this MG.

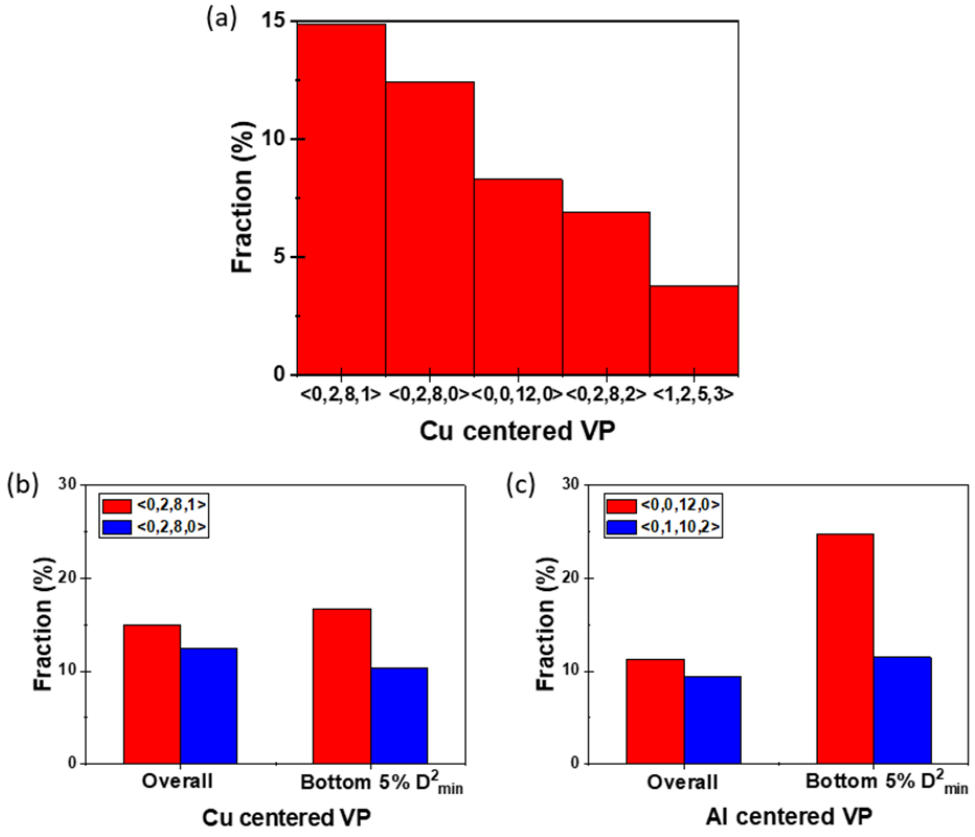

Fig.5.6 Effect of topological order in mechanical response of Cu and Al atoms. (a) Most common VP around Cu atoms in $Al_{90}Sm_8Cu_2$. The fraction on the vertical axis indicates the fraction of each type of VP among all the Cu atoms in the system. The overall fractions of the dominant clusters around (b) Cu atoms and (c) Al atoms are compared with their fractions among the 5% of atoms with the lowest D^2_{min} (as determined by classical MD). Overall fractions are normalized to the total number of each type of atom in the entire sample while fractions in the bottom 5% of D^2_{min} are normalized to the number of each type of atom in the bottom 5% of D^2_{min}.

So far, we have demonstrated that Cu atoms provide a higher resistance to local shear transformations as compared to Al atoms and that the resistance of Cu atoms to deformation is independent of their topological environment. This finding suggests that the nature of bonding between Cu atoms and the surrounding Al atoms could be the main reason for their higher resistance to local shear transformations. We hypothesize that the mechanical strength of Al-Sm-TM alloys is correlated with the strength of the Al-TM bond and that this correlation is strong enough to break the correlation between mechanical response and the dominant topological SRO in the MG.

To test this hypothesis, we calculated the force constant of the atomic vibrations of TM atoms as well as the formation energy of a TM vacancy in the melt quenched samples, as two measures of the Al-TM bond strength. Here, vacancy formation energy is defined as the energy cost of isolating a TM atom by breaking the bonds between the atom and its neighbors. These calculations were carried out using *ab initio* calculations on amorphous samples that were also prepared using *ab initio* methods. In Fig.5.7a and 5.7b we plot the experimentally measured hardness against the calculated force constant and the vacancy formation energy, respectively. We see that the hardness increases monotonically with the force constant and with the vacancy formation energy. The difference in the Al-TM bond strengths is also reflected in the relative shortening of the Al-TM bond lengths for the different TMs due to the partially covalent nature of the bond [151–154]. We have used pair distribution functions from the *ab initio* MD simulations of $Al_{90}Sm_8Cu_2$, $Al_{90}Sm_8Ag_2$, and $Al_{90}Sm_8Au_2$ MGs to calculate the Al-TM bond lengths and compared them with the bond lengths calculated theoretically by assuming purely metallic bonding between the Al and TM atoms (as explained in Table 5.1). We found that Al-Au bonds had the largest percentage shortening in bond length (7.7%) and therefore the strongest bonds, followed by Al-Cu (6%), and then Al-Ag (4.2%), which is in agreement with the trends in the force constants and in the vacancy formations energies

determined from *ab initio* calculations. This analysis confirms that the mechanical properties of Al-Sm-TM alloys are correlated with the strength of the Al-TM bonds.

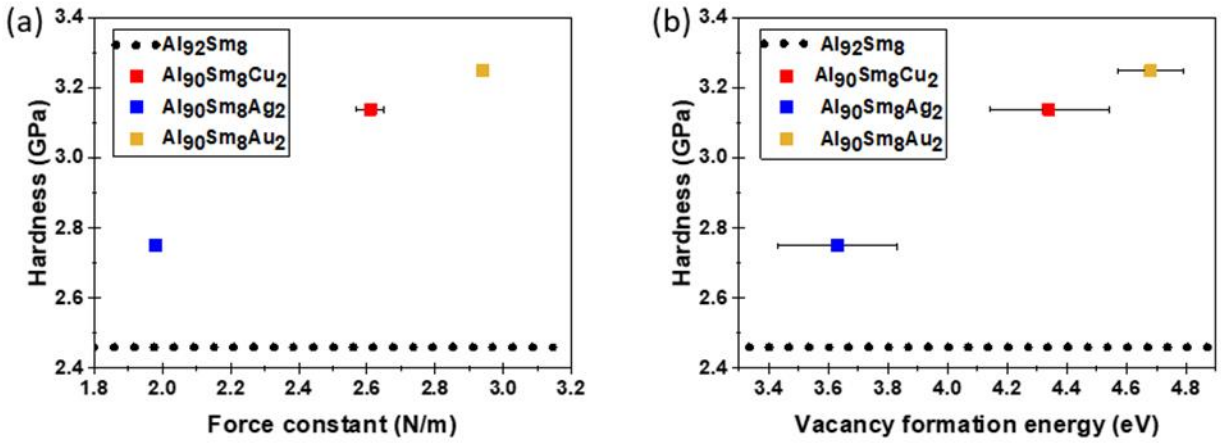

Fig. 5.7 Relation between hardness and Al-TM bond strength. Trends between the experimentally measured hardness and (a) force constants of Al-TM bonds along x normal direction (the force constants of Al-Tm bonds along the other two normal directions have the similar trend) and (b) TM vacancy formation energies determined from ab initio simulations. The dotted line is added to show the hardness of $Al_{92}Sm_8$. Calculations by Dr. Jiaqi Xi.

Al metallic radius[1] (Å)	**TM**	**TM metallic radius**[155] **(Å)**	**Sum of metallic radii (Å)**	**Al-TM RDF peak (Å)**	**% shortening in bond length**
1.43	Cu	1.28	2.71	2.55	6.0
1.43	Ag	1.44	2.87	2.75	4.2
1.43	Au	1.44	2.87	2.65	7.7

Table 5.1 Al-TM bond lengths calculated from ab initio PDF compared with the bond length obtained as sum of metallic radii.

5.4 Conclusions and Outlook

In conclusion, we have shown that the strengthening of Al-Sm MGs with minor alloying is due to strong chemical bonds between Al and TM atoms rather than due to changes in the atomic configurations and the topological order. Further, our results show that stronger chemical bonding between atoms does not necessarily result in a more ordered structure and that the effect of chemical bonding and the effect of topology may sometimes compete with each other in controlling the mechanical properties of the MG. This is in contrast to Cu-Zr MGs alloyed with Al where the effect of chemical bonding between Cu and Al is conflated with increased icosahedral order[108]. Our results therefore point to the importance of studying chemical and topological effects separately in MGs and also highlight the necessity of studying alloy systems other than the commonly studied Cu-Zr system to provide understanding of the structure-property relations in MGs.

6. Plasticity in metallic glasses: Correlations with structure and heterogeneity

This chapter is based on ongoing work.

6.1 Introduction

Bulk metallic glasses (BMGs) have attracted considerable attention due to their exceptional mechanical properties, offering great promise as structural materials for engineering applications [2]. However, most BMGs are incapable of accommodating plastic strain and thus undergo catastrophic fracture when strains exceed their elastic limit. The brittle nature of BMGs has severely limited their widespread use. Therefore, enhancing the ductility of BMGs is crucial to exploit their potential as structural materials. Various approaches have been explored to enhance the ductility of monolithic BMGs, which can be broadly categorized into two groups: rejuvenation and alloying.

Rejuvenation refers to the process of moving the glass to less stable thermodynamic states in the potential energy landscape by increasing their enthalpy through processes such as ion irradiation, severe plastic deformation, or cryo-thermal cycling [156]. Another way to obtain a rejuvenated glass is by rapid quenching of the liquid such that it gets frozen in a high enthalpy state. Either way, the rejuvenated glass structure is more disordered compared to more stable, relaxed structures and contains excess free volume. The local structures that contain this excess free volume are referred to as soft spots or geometrically unfavorable motifs (GUMs) and act as fertile sites for the activation of shear transformation zones (STZs) [130]. The presence of the soft spots or GUMs results in a heterogeneous glass structure with uniform activation of STZs across the sample, leading to homogenous plastic flow. As a result, the rejuvenated glass can accommodate larger plastic strains and will be more ductile.

On the other hand, the impact of alloying, more specifically minor alloying on the structure of BMGs is more intricate. Minor additions of alloying elements influence multiple atomic-level properties, such as bond strengths or local topological and chemical ordering [9,157–159]. Consequently, the precise nature of structural changes responsible for altering the plasticity of BMGs remains poorly understood. Sometimes, improved ductility with minor alloying is attributed to increased structural heterogeneity. However, unlike the process of rejuvenation where heterogeneity is increased by the means of soft spots, minor alloying can

also increase heterogeneity by introducing so-called hard spots in the glass structure [160]. These hard spots, which could either be regions with increased topological order or stronger chemical bonds, are stiffer than their neighboring regions and act as barriers to shear band propagation, encouraging the branching of shear bands [161] again resulting in more homogeneous plastic flow. While one way to think about structural heterogeneity is in terms of the diversity in the local structure and composition, it can also arise from the spatial distribution of the same local properties. Spatial heterogeneity characterized in terms of correlation lengths, can be altered by rejuvenation as well as minor alloying and has been also shown to influence the mechanical response of BMG [162–164].

There still remains a significant obstacle in designing ductile BMGs due to the lack of a universal correlation between the material's atomic-level structure and its plastic deformation. Parameters such as free volume [161] and structural heterogeneity defined in terms of spatial correlation lengths or in terms of the diversity or spread in local properties such as topological short-range order, local stiffness, etc., have been suggested as key measures of plasticity [163–165]. However, the applicability of these measures over different compositions and thermodynamic states of BMGs has not been tested simultaneously to obtain generalized correlations.

In this chapter, we aim to explore and establish correlations between plasticity and structural parameters characterizing atomic level structure and heterogeneity in BMGs. Our investigation encompasses various compositions and thermodynamic states to determine the general applicability of these correlations. By thoroughly examining these relationships, we aim to identify universal guidelines in the design of ductile BMGs.

6.2 Materials and Methods

We have conducted classical molecular dynamics (MD) simulations of Zr-Cu based MGs using the LAMMPS package [22] and EAM potentials [166]. We quench the liquid with varying rates (10^{10}K/s and 10^{12}K/s) to access different thermodynamic states of the glass. The glass obtained from a higher quenching rate (10^{12}K/s) is the equivalent of a rejuvenated state with respect to the glass made at a lower quenching rate (10^{10}K/s). For the purpose of minor alloying, we have chosen Al and Ag, which are known to have opposite effects on the ductility of Zr-Cu based BMGs [108,157,167]. We start with a binary composition of

$Zr_{50}Cu_{50}$ and substitute equal parts of Zr and Cu with 5% and 10% (atomic) of Al and Ag. This approach allows us to explore a wide range of structural states and mechanical responses in the Zr-Cu system and then identify valid correlations between them. The procedure for the melt-quench process and subsequent tensile deformation is described in [9]. The visualization of the glass structures, Voronoi analysis, and calculation of atomic strains was done using Ovito [108]. The procedure for MD simulations of dynamic mechanical analysis (DMA) was adopted from [168].

6.3 Results and Discussion

The tensile stress-strain curves for the two quenching rates and five different compositions are shown in Fig.6.1. All the samples reach a maximum tensile stress which is followed by a sudden drop in stress. This maximum corresponds to the point where the STZs percolate through the entire sample and marks the beginning of localized deformation within narrow shear bands. The peak stress in the stress-strain curve can be considered to be the tensile strength of the sample (σ_T) changes with composition and quenching rate. We see that the tensile strength decreases with rejuvenation (higher quenching rate) and with the addition of Ag while it increases with Al addition.

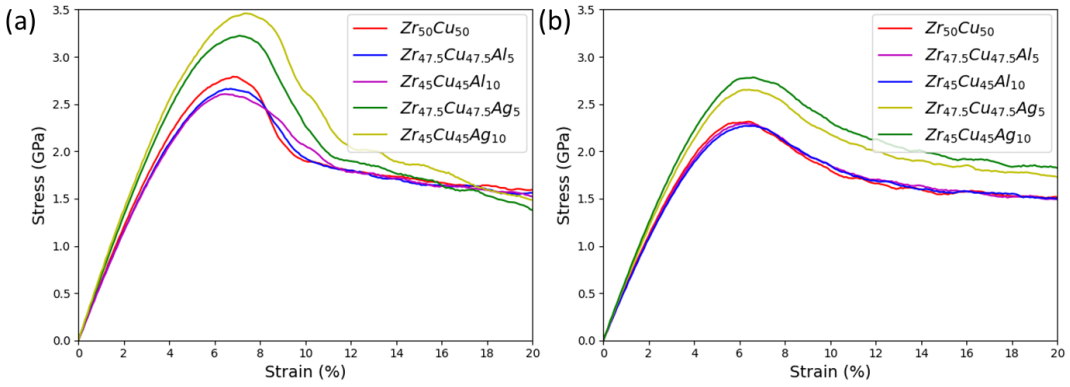

Fig.6.1 Tensile stress strain curves for samples with quenching rate of (a) 10^{10}K/s and (b) 10^{12}K/s.

The distribution of atomic strains in the different samples is shown in Fig.6.2. It is clear that strain is more uniformly distributed in multiple shear bands in the case of the rejuvenated samples and the samples containing Ag allowing the samples to accommodate larger strains without undergoing fracture. On the other hand, the low quenching rate samples containing Al show that the strains are highly localized

in a single dominant shear band where shear instabilities arise leading to fracture (in-plane shear/ mode-II fracture) [169]. It can also be seen that in the rejuvenated state, all the samples appear to have uniformly distributed strains with the minor alloying elements not causing any significant changes.

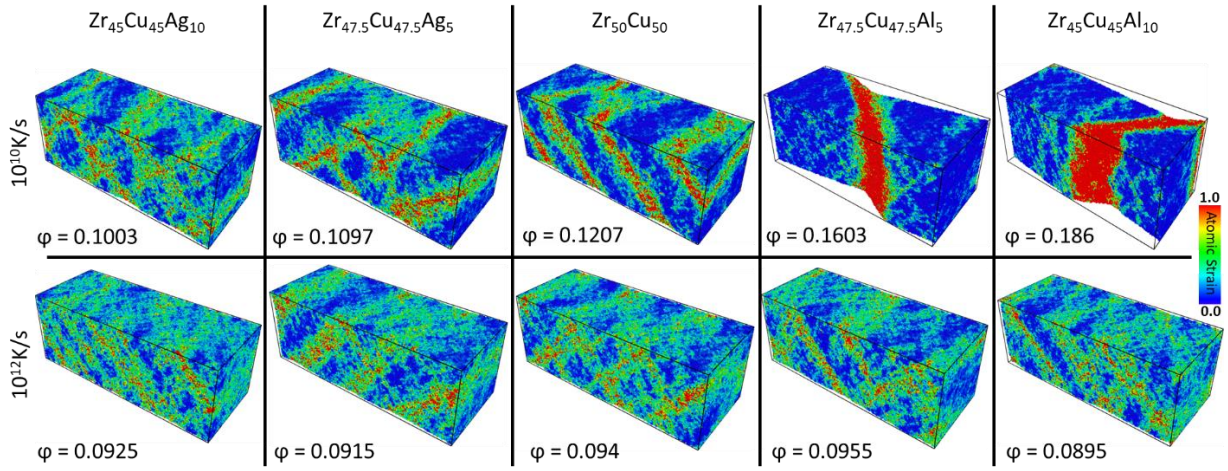

Fig. 6.2 Distribution of atomic strains at 20% overall tensile strain.

While Fig.6.2 displays the qualitative differences in the plastic deformation of the various samples, we need a quantitative measure of ductility in order to establish meaningful correlations with structural features. In experimental studies, the tensile strain at fracture serves as a direct measure ductility. However, the MD simulated samples are much more ductile compared to experimental samples due to the following reasons. First, the quenching rates used in MD simulations are several orders of magnitude higher than experimental quenching rates, resulting in highly rejuvenated structures that are relatively very ductile compared to experimental samples. Second, the MD simulated glasses do not possess any extrinsic defects like micro cracks that can act as stress concentrators and reduce ductility as in the case of experimentally synthesized samples. As a result, the samples in MD simulations rarely undergo fracture. We therefore use an indirect measure based on the localization of atomic strains to quantify the ductility of the samples in our study. It is known that localization of strain is the root cause of brittle fracture in metallic glasses [169], and that a more uniform distribution of strain increases ductility. Based on this we can use the strain localization parameter, defined as $\varphi = \sqrt{\frac{1}{N}\sum_{i=1}^{N}(\eta_i - \eta_{average})^2}$ (where N is the system size and η is the atomic strain) as an indirect measure of ductility. A higher value of φ means that the atomic strains

are more localized and *vice versa* (Fig.6.2). The addition of Al increases φ (makes the glass more brittle) and the addition of Ag decreases it (makes the glass more ductile), while rejuvenation also decreases φ. These results confirm that our simulations reproduce the changes expected in the mechanical response of Zr-Cu based MGs with rejuvenation and minor additions of Al and Ag based on literature [108,157,167]. With this, we move forward with further analysis to identify the structural changes responsible for the varying mechanical responses.

To characterize the atomic level structure of the different samples, we have used a structural parameter called the flexibility volume [130]. Defined as $v_{flex} = \langle r \rangle^2 . \sqrt[3]{\Omega_a}$, the flexibility volume is the product of the vibrational mean squared displacement of an atom ($\langle r \rangle^2$) with the cube root of its Voronoi volume (Ω_a). At the atomic scale, v_{flex} has been shown to correlate with microscopic properties such as activation energies for thermally activated relaxations and propensity for stress driven shear transformations. At the same time the average flexibility volume of system V_{flex} has been shown to correlate with macroscopic properties like the shear modulus. This parameter not only considers the influence of local topology through the atomic volume, but also incorporates information about local bond strengths and dynamics through the vibrational mean squared displacement. Ding *et al.* [130] therefore deemed the flexibility volume to be a universal structural parameter, capable of predicting macroscopic as well as microscopic properties of metallic glasses irrespective of composition and processing history.

We have used the average flexibility volume V_{flex} as a structural parameter to correlate with the deformation behavior of our samples in terms of the ultimate tensile strength (σ_T) and strain localization parameter (φ). σ_T appears to decrease linearly with increasing V_{flex} (Fig.6.3a) with different quenching rates having slightly different slopes. The inverse relationship between V_{flex} and σ_T is not surprising considering the fact that at the atomic scale, atoms with higher v_{flex} have a higher propensity to undergo shear transformations and for STZs. However, σ_T is not only affected by the activation of STZs, but also their percolation through the sample to form shear bands which can be influenced by the spatial heterogeneity in the samples. This means that σ_T also depends on structural features at a longer length scale which are not captured by V_{flex}, which only considers properties like atomic volume and vibrational MSD that are only influenced by the nearest neighbors. In BMGs, local structures can be correlated beyond the nearest

neighbors up to length scales of a few nanometers, resulting in spatial heterogeneity. This can be probed using spatial autocorrelation functions of local properties like v_{flex}. The spatial autocorrelation function is defined as $C(r) = \frac{\sum_{r_0,r_0+r}(\mu_{r_0}-\bar{\mu})(\mu_{r_0+r}-\bar{\mu})}{\sqrt{\sum_{r_0,r_0+r}(\mu_{r_0}-\bar{\mu})^2}\sqrt{\sum_{r_0,r_0+r}(\mu_{r_0+r}-\bar{\mu})^2}}$ [163], where r separation distance and μ is a local property, which in this case is v_{flex}. The spatial correlation functions show exponential decay with increasing distance in all the samples (Fig.6.4). The decay can be described by a function of the form $C(r) = e^{-3r/l}$, where *l* is the correlation length defined as the smallest distance beyond which the correlation function is lower than 0.05. The correlation lengths for all the samples are in a range of 6Å to 8Å which is around the second nearest neighbor distance. The dependence of σ_T on the correlation length is shown in Fig.6.3b. We see that the peak stress shows a decreasing trend with increasing correlation length similar to the Hall-Petch relationship between hardness and length scale of spatial heterogeneity reported by Zhu *et al.* [162]. However, the relationship between the correlation length and σ_T is only valid for a fixed quenching rate while the correlation length doesn't seem to be sensitive to changes in the quenching rate for a fixed composition. We then measure the structural heterogeneity in terms of the diversity in local structure and dynamics by looking at the variance v_{flex}. Here, we see an inverse relationship between σ_T and the variance in v_{flex} for changing composition as well as changing quenching rates (Fig.6.3c). However, σ_T and the variance also don't appear to have a universal correlation applicable across quenching rates and compositions. These findings demonstrate that the examined structural parameters (V_{flex}, it's correlation length, and variance) exert some influence on the tensile strength of Bulk Metallic Glasses (BMGs). However, it is evident that individual parameters do not solely account for the observed effects of minor alloying and rejuvenation on tensile strength of BMGs

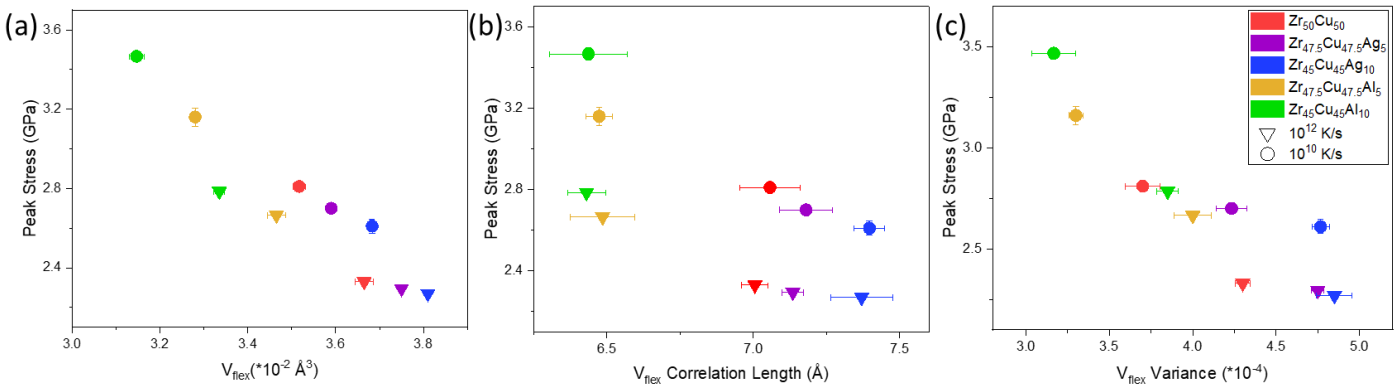

Fig. 6.3 Dependence of tensile strength on (a) average flexibility volume, (b) correlation length of flexibility volume, and (c) variance in flexibility volume.

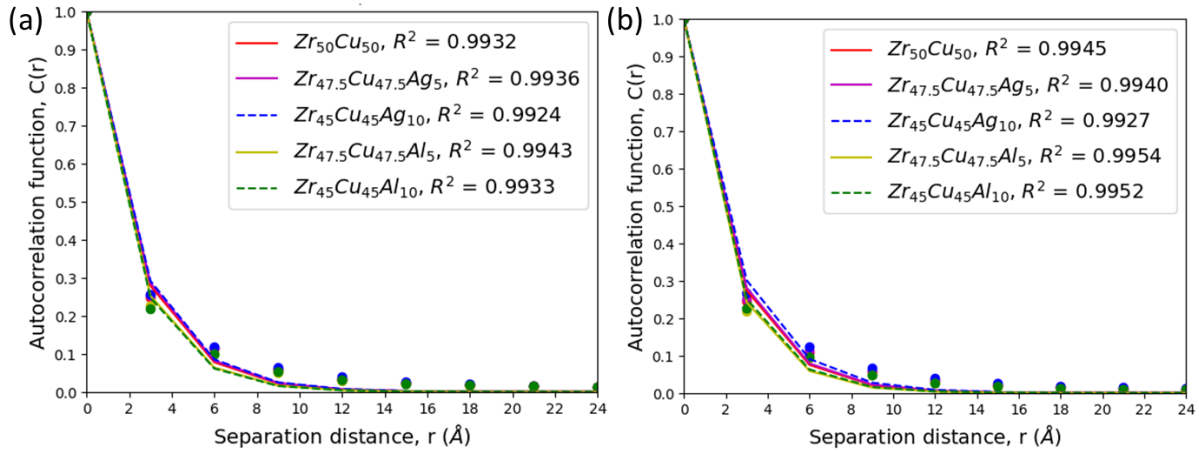

Fig. 6.4 Spatial autocorrelation functions for quenching rate of (a) 10^{10}K/s and (b) 10^{12}K/s showing exponential decay with increasing separation distance.

Next, we look at the dependence of ductility (measured by the strain localization parameter, φ) on the same structural features. At the lower cooling rate, φ shows the same inverse dependence on V_{flex} (Fig.6.5a), correlation length (Fig.6.5b), and variance (Fig.6.5c) as the tensile strength. However, unlike σ_T, φ does not seem to have any correlation with the same structural parameters in the case of the rejuvenated samples (higher quenching rate). This means that there is something that is making the rejuvenated samples more ductile that is not accounted for by the structural parameters considered here.

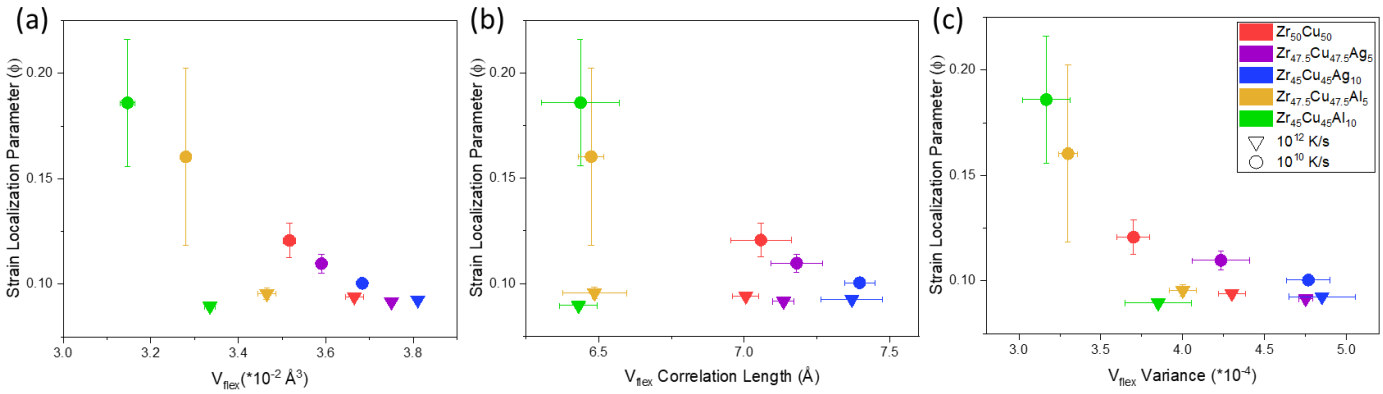

Fig. 6.5 Dependence of strain localization parameter on (a) average flexibility volume, (b) correlation length of flexibility volume, and (c) variance in flexibility volume.

To understand the lack of correlation between φ and the structural parameters in the rejuvenated samples, we adopt another approach to understanding ductility in BMGs that involves examining thermally activated relaxations. Similar to the stress-induced activation and percolation of Shear Transformation Zones (STZs), elevated temperatures also activate flow units in the glass, leading to percolation within the structure and eventual glass transition. This thermal activation of flow units occurs at low temperatures and is referred to as a fast secondary relaxation process, denoted as β' or γ relaxation. The activation energy for the γ relaxation process has been found to be similar to the activation energy of STZs [170]. Upon further heating, BMGs exhibit a slow secondary relaxation process known as β relaxation. Similar to the percolation of STZs during plastic deformation, the β relaxation process is governed by the percolation of flow units, and its activation energy, representing the barrier to the percolation of flow units, correlates with the strength of the BMG [158]. Probing thermally induced relaxations can, therefore, provide useful insights into the deformation behavior of BMGs.

Dynamic mechanical analysis (DMA) is a commonly used experimental tool to study thermal relaxations in BMGs. We have performed MD simulated DMA and measured the storage modulus and the loss modulus as a function of temperature. We observe that the storage modulus exhibits a similar dependence on temperature for all the samples irrespective of quenching rate (Fig.6.6a, b). The storage modulus is the highest at 300K and goes on decreasing gradually with increasing temperature until the sample reaches its glass transition temperature where there is a sudden drop in the storage modulus over a small temperature range. On the other hand, the dependence of loss modulus on temperature reveals the secondary β relaxation along with the primary α relaxation for the samples with the lower quenching rate (Fig.6.6c). In the binary $Zr_{50}Cu_{50}$ sample, the beta relaxation occurs in the form of an excess wing to the primary relaxation peak. In the $Zr_{45}Cu_{45}Al_{10}$ sample, the β relaxation is more pronounced and appears as a shoulder prior to the alpha relaxation peak, while $Zr_{45}Cu_{45}Ag_{10}$ sample has a distinct beta relaxation peak. Overall, this result demonstrates that the samples made at the lower quenching rate exhibit thermal relaxations analogous to stress driven percolation of STZs during plastic deformation. One the other hand the rejuvenated samples made with a higher quenching rate appear to have a relatively high loss modulus

even at room temperature and don't show clear signs of a secondary relaxation process prior to the glass transition (Fig.6.6d). This suggests that the high quenching rate samples might be trapped in a highly disordered state that undergoes homogenous plastic flow like a supercooled liquid. However, the underlying structural features that enable the rejuvenated glasses to undergo homogenous plastic flow are not captured by the structural parameters considered in this study. For instance, the samples made with the low quenching rate may possess structural features at longer length scales like medium range ordering, which could be absent in the rejuvenated samples. Such differences in the medium range order are not captured by the flexibility volume and could influence the strain localization and plastic deformation of the samples.

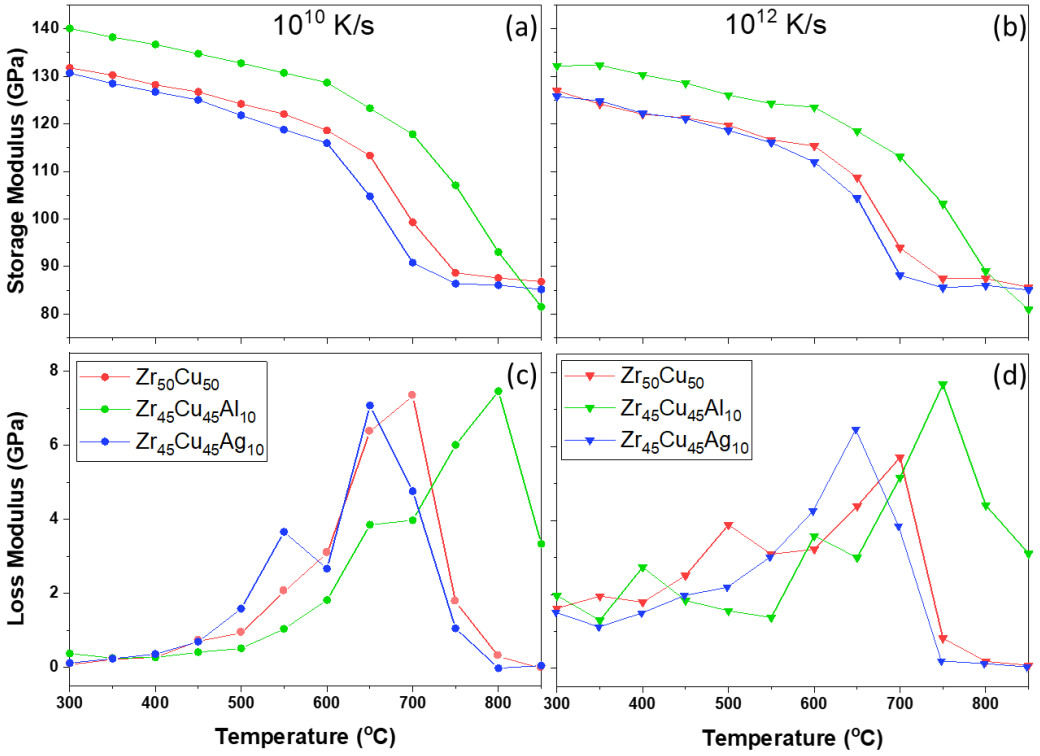

Fig. 6.6 Temperature dependance of (a), (b) storage modulus and (c), (d) loss modulus for quenching rates of (a), (c) 10^{10}K/s and (b), (d) 10^{12}K/s.

6.4 Conclusions and Outlook

Through this study we have attempted to identify universal correlations between the mechanical properties of BMGs, specifically those related to plastic deformation and different structural features. Unlike the elastic modulus which shows a universal correlation with a structural parameter like the flexibility volume, we show that properties related to the plastic deformation like the tensile strength and ductility are influenced by multiple structural features that may span across different length scales. Moving forward, the goal for this study will be to find ways to characterize the structure of the different samples at longer length scales such that the effects of medium range order are also considered while looking for correlations with the strain localization behavior. Ultimately, any model that is capable of predicting the ductility of BMGs will have to consider features describing the glass structure at multiple length scales.

References

[1] W. Klement, R.H. Willens, P. Duwez, Non-crystalline structure in solidified Gold-Silicon alloys, Nature. 187 (1960) 869–870. https://doi.org/10.1038/187869b0.

[2] M. Telford, The case for bulk metallic glass, Mater. Today. 7 (2004) 36–43. https://doi.org/10.1016/S1369-7021(04)00124-5.

[3] J. Schroers, Processing of Bulk Metallic Glass, Adv. Mater. 22 (2010) 1566–1597. https://doi.org/10.1002/adma.200902776.

[4] Y. Li, S. Zhao, Y. Liu, P. Gong, J. Schroers, How Many Bulk Metallic Glasses Are There?, ACS Comb. Sci. 19 (2017) 687–693. https://doi.org/10.1021/acscombsci.7b00048.

[5] H. Bei, S. Xie, E.P. George, Softening caused by profuse shear banding in a bulk metallic glass, Phys. Rev. Lett. 96 (2006) 105503. https://doi.org/10.1103/PhysRevLett.96.105503.

[6] P. Yiu, W. Diyatmika, N. Bönninghoff, Y.-C. Lu, B.-Z. Lai, J.P. Chu, Thin film metallic glasses: Properties, applications and future, J. Appl. Phys. 127 (2020) 30901. https://doi.org/10.1063/1.5122884.

[7] Y.Q. Cheng, E. Ma, Atomic-level structure and structure-property relationship in metallic glasses, Prog. Mater. Sci. 56 (2011) 379–473. https://doi.org/10.1016/j.pmatsci.2010.12.002.

[8] H.S. Chen, B.K. Park, Role of chemical bonding in metallic glasses, Acta Metall. 21 (1973) 395–400. https://doi.org/10.1016/0001-6160(73)90196-X.

[9] V. Jambur, C. Tangpatjaroen, J. Xi, J. Tarnsangpradit, M. Gao, H. Sheng, J.H. Perepezko, I. Szlufarska, Effects of minor alloying on the mechanical properties of Al based metallic glasses, J. Alloys Compd. 854 (2021) 157266. https://doi.org/10.1016/j.jallcom.2020.157266.

[10] A. Heuer, Properties of a glass-forming system as derived from its potential energy landscape, Phys. Rev. Lett. 78 (1997) 4051–4054. https://doi.org/10.1103/PhysRevLett.78.4051.

[11] F. Sciortino, Potential energy landscape description of supercooled liquids and glasses, J. Stat. Mech. Theory Exp. 2005 (2005) 311–345. https://doi.org/10.1088/1742-5468/2005/05/P05015.

[12] P.G. Debenedetti, F.H. Stillinger, Supercooled liquids and the glass transition, Nature. 410 (2001) 259–267. https://doi.org/10.1038/35065704.

[13] D.M. Mattox, Introduction, in: Handb. Phys. Vap. Depos. Process., Elsevier, 2010: pp. 1–24. https://doi.org/10.1016/b978-0-8155-2037-5.00001-0.

[14] D.M. Mattox, Physical Sputtering and Sputter Deposition (Sputtering), in: Handb. Phys. Vap. Depos. Process., Elsevier, 2010: pp. 237–286. https://doi.org/10.1016/b978-0-8155-2037-5.00007-1.

[15] F.A. Smidt, Use of ion beam assisted deposition to modify the microstructure and properties of thin films, Int. Mater. Rev. 35 (1990) 61–128. https://doi.org/10.1179/095066090790323975.

[16] W.C. Oliver, G.M. Pharr, An improved technique for determining hardness and elastic modulus using load and displacement sensing indentation experiments, J. Mater. Res. 7 (1992) 1564–1583. https://doi.org/10.1557/JMR.1992.1564.

[17] C.A. Schuh, Nanoindentation studies of materials, Mater. Today. 9 (2006) 32–40. https://doi.org/10.1016/S1369-7021(06)71495-X.

[18] S. Takeuchi, K. Edagawa, Atomistic simulation and modeling of localized shear deformation in metallic glasses, in: Prog. Mater. Sci., Pergamon, 2011: pp. 785–816. https://doi.org/10.1016/j.pmatsci.2011.01.007.

[19] D. Hossain, M.A. Tschopp, D.K. Ward, J.L. Bouvard, P. Wang, M.F. Horstemeyer, Molecular dynamics simulations of deformation mechanisms of amorphous polyethylene, Polymer (Guildf). 51 (2010) 6071–6083. https://doi.org/10.1016/j.polymer.2010.10.009.

[20] A. Kedharnath, R. Kapoor, A. Sarkar, Classical molecular dynamics simulations of the deformation of metals under uniaxial monotonic loading: A review, Comput. Struct. 254 (2021) 106614. https://doi.org/10.1016/j.compstruc.2021.106614.

[21] J.L. Finney, Random packings and the structure of simple liquids. I. The geometry of random close packing, Proc. R. Soc. London. A. Math. Phys. Sci. 319 (1970) 479–493. https://doi.org/10.1098/rspa.1970.0189.

[22] S. Plimpton, Fast Parallel Algorithms for Short-Range Molecular Dynamics, J. Comput. Phys. 117 (1997) 1–42. https://doi.org/10.1006/jcph.1995.1039.

[23] J.P. Chu, J.C. Huang, J.S.C. Jang, Y.C. Wang, P.K. Liaw, Thin film metallic glasses: Preparations, properties, and applications, Jom. 62 (2010) 19–24. https://doi.org/10.1007/s11837-010-0053-3.

[24] J.P. Chu, J.S.C. Jang, J.C. Huang, H.S. Chou, Y. Yang, J.C. Ye, Y.C. Wang, J.W. Lee, F.X. Liu, P.K. Liaw, Y.C. Chen, C.M. Lee, C.L. Li, C. Rullyani, Thin film metallic glasses: Unique properties and potential applications, Thin Solid Films. 520 (2012) 5097–5122. https://doi.org/10.1016/j.tsf.2012.03.092.

[25] R.B. Schwarz, W.L. Johnson, Formation of an amorphous alloy by solid-state reaction of the pure polycrystalline metals, Phys. Rev. Lett. 51 (1983) 415–418. https://doi.org/10.1103/PhysRevLett.51.415.

[26] S.F. Swallen, K.L. Kearns, M.K. Mapes, Y.S. Kim, R.J. McMahon, M.D. Ediger, T. Wu, L. Yu, S. Satija, Organic glasses with exceptional thermodynamic and kinetic stability, Science (80-.). 315 (2007) 353–356. https://doi.org/10.1126/SCIENCE.1135795/SUPPL_FILE/SWALLEN_SOM.PDF.

[27] H. Bin Yu, Y. Luo, K. Samwer, Ultrastable metallic glass, Adv. Mater. 25 (2013) 5904–5908. https://doi.org/10.1002/ADMA.201302700.

[28] D.P.B. Aji, A. Hirata, F. Zhu, L. Pan, K.M. Reddy, S. Song, Y. Liu, T. Fujita, S. Kohara, M. Chen, Ultrastrong and Ultrastable Metallic Glass, ArXiv Prepr. (2013). http://arxiv.org/abs/1306.1575 (accessed January 1, 2021).

[29] D.J. Magagnosc, G. Feng, L. Yu, X. Cheng, D.S. Gianola, Isochemical control over structural state and mechanical properties in Pd-based metallic glass by sputter deposition at elevated temperatures, APL Mater. 4 (2016) 086104. https://doi.org/10.1063/1.4960388.

[30] P. Luo, C.R. Cao, F. Zhu, Y.M. Lv, Y.H. Liu, P. Wen, H.Y. Bai, G. Vaughan, M. Di Michiel, B. Ruta, W.H. Wang, Ultrastable metallic glasses formed on cold substrates, Nat. Commun. 9 (2018) 1–7. https://doi.org/10.1038/s41467-018-03656-4.

[31] Q. Sun, D.M. Miskovic, K. Laws, H. Kong, X. Geng, M. Ferry, Transition towards ultrastable metallic glasses in Zr-based thin films, Appl. Surf. Sci. 533 (2020) 147453. https://doi.org/10.1016/J.APSUSC.2020.147453.

[32] S. V Muley, C. Cao, D. Chatterjee, C. Francis, F.P. Lu, M.D. Ediger, J.H. Perepezko, P.M. Voyles, Varying kinetic stability, icosahedral ordering, and mechanical properties of a model Zr-Cu-Al metallic glass by sputtering, Phys. Rev. Mater. 5 (2021) 33602. https://doi.org/10.1103/PhysRevMaterials.5.033602.

[33] L. Zhu, C.W. Brian, S.F. Swallen, P.T. Straus, M.D. Ediger, L. Yu, Surface Self-Diffusion of an Organic Glass, Phys. Rev. Lett. 106 (2011) 256103–256104. https://doi.org/10.1103/PhysRevLett.106.256103.

[34] W. Zhang, L. Yu, Surface Diffusion of Polymer Glasses, Macromolecules. 49 (2016) 731–735.

https://doi.org/10.1021/acs.macromol.5b02294.

[35] Y. Zhang, R. Potter, W. Zhang, Z. Fakhraai, Using tobacco mosaic virus to probe enhanced surface diffusion of molecular glasses, Soft Matter. 12 (2016) 9115. https://doi.org/10.1039/c6sm01566b.

[36] C.R. Cao, Y.M. Lu, H.Y. Bai, W.H. Wang, High surface mobility and fast surface enhanced crystallization of metallic glass, Appl. Phys. Lett. 107 (2015) 141606. https://doi.org/10.1063/1.4933036.

[37] K.L. Ngai, S. Capaccioli, C.R. Cao, H.Y. Bai, W.H. Wang, Quantitative explanation of the enhancement of surface mobility of the metallic glass Pd40Cu30Ni10P20 by the Coupling Model, J. Non. Cryst. Solids. 463 (2017) 85–89. https://doi.org/10.1016/J.JNONCRYSOL.2017.03.002.

[38] C.R. Cao, L. Yu, J.H. Perepezko, Surface dynamics measurement on a gold based metallic glass, Appl. Phys. Lett. 116 (2020) 231601. https://doi.org/10.1063/5.0007838.

[39] L. Berthier, P. Charbonneau, E. Flenner, F. Zamponi, Origin of Ultrastability in Vapor-Deposited Glasses, (2017). https://doi.org/10.1103/PhysRevLett.119.188002.

[40] J.M.E. Harper, J.J. Cuomo, R.J. Gambino, H.R. Kaufman, Modification of thin film properties by ion bombardment during deposition, Nucl. Instruments Methods Phys. Res. Sect. B Beam Interact. with Mater. Atoms. 7–8 (1985) 886–892. https://doi.org/10.1016/0168-583X(85)90489-6.

[41] J. Kobata, K. ichi Miura, Effects of Ar ion bombardment by unbalanced magnetron sputtering on mechanical and thermal properties of Ti-Cu-Zr-Ni-Hf-Si thin film metallic glass, Mater. Des. 111 (2016) 271–278. https://doi.org/10.1016/J.MATDES.2016.09.005.

[42] J. Ding, Y.-Q. Cheng, H. Sheng, E. Ma, Short-range structural signature of excess specific heat and fragility of metallic-glass-forming supercooled liquids, Phys. Rev. B. 85 (2012) 060201. https://doi.org/10.1103/PhysRevB.85.060201.

[43] J.F. Ziegler, M.D. Ziegler, J.P. Biersack, SRIM - The stopping and range of ions in matter (2010), Nucl. Instruments Methods Phys. Res. Sect. B Beam Interact. with Mater. Atoms. 268 (2010) 1818–1823. https://doi.org/10.1016/j.nimb.2010.02.091.

[44] A.G. Shard, Practical guides for x-ray photoelectron spectroscopy: Quantitative XPS, J. Vac. Sci. Technol. A. 38 (2020) 041201. https://doi.org/10.1116/1.5141395.

[45] A. Guinier, X-ray Diffraction in Crystals, Imperfect Crystals, and Amorphous Bodies, 1994.

[46] M. Wu, J. Cheng, J.S. Tse, Y. Pan, L. Zhang, Density power law and structures of metallic glasses, Acta Mater. 141 (2017) 75–82. https://doi.org/10.1016/j.actamat.2017.09.014.

[47] A.G. Dirks, H.J. Leamy, Columnar microstructure in vapor-deposited thin films, Thin Solid Films. 47 (1977) 219–233. https://doi.org/10.1016/0040-6090(77)90037-2.

[48] S.G. Mayr, K. Samwer, Tailoring the surface morphology of amorphous thin films by appropriately chosen deposition conditions, J. Appl. Phys. 91 (2002) 2779–2784. https://doi.org/10.1063/1.1446235.

[49] P. Denis, S.Y. Liu, H.J. Fecht, Growth mode transition in Au-based thin film metallic glasses, Thin Solid Films. 665 (2018) 29–35. https://doi.org/10.1016/j.tsf.2018.08.006.

[50] J.E. Greene, Thin Film Nucleation, Growth, and Microstructural Evolution: An Atomic Scale View, in: Handb. Depos. Technol. Film. Coatings Sci. Appl. Technol., Elsevier, 2009: pp. 554–620. https://doi.org/10.1016/B978-0-8155-2031-3.00012-0.

[51] W. Yao, Q.P. Cao, S.Y. Liu, X.D. Wang, H.J. Fecht, A. Caron, D.X. Zhang, J.Z. Jiang, Tailoring nanostructured Ni-Nb metallic glassy thin films by substrate temperature, Acta Mater. 194 (2020) 13–26. https://doi.org/10.1016/j.actamat.2020.04.046.

[52] C.A. Schuh, T.G. Nieh, A nanoindentation study of serrated flow in bulk metallic glasses, Acta Mater. 51 (2003) 87–99. https://doi.org/10.1016/S1359-6454(02)00303-8.

[53] H. Bei, Z.P. Lu, E.P. George, Theoretical Strength and the Onset of Plasticity in Bulk Metallic Glasses Investigated by Nanoindentation with a Spherical Indenter, Phys. Rev. Lett. 93 (2004). https://doi.org/10.1103/PhysRevLett.93.125504.

[54] J.H. Perepezko, S.D. Imhoff, M.-W. Chen, J.-Q. Wang, S. Gonzalez, Nucleation of shear bands in amorphous alloys, Proc. Natl. Acad. Sci. 111 (2014) 3938–3942. https://doi.org/10.1073/pnas.1321518111.

[55] Z.P. Lu, H. Tan, Y. Li, S.C. Ng, Correlation between reduced glass transition temperature and glass forming ability of bulk metallic glasses, Scr. Mater. 42 (2000) 667–673. https://doi.org/10.1016/S1359-6462(99)00417-0.

[56] D. Janovszky, M. Sveda, A. Sycheva, F. Kristaly, F. Zámborszky, T. Koziel, P. Bala, G. Czel, G. Kaptay, Amorphous alloys and differential scanning calorimetry (DSC), J. Therm. Anal. Calorim. 2021 14713. 147 (2021) 7141–7157. https://doi.org/10.1007/S10973-021-11054-0.

[57] C. Yildirim, M. Kutsal, R.T. Ott, M.F. Besser, M.J. Kramer, Y.E. Kalay, The role of amorphous precursor in phase selection hierarchy in marginal metallic glasses, Mater. Des. 112 (2016) 479–484. https://doi.org/10.1016/j.matdes.2016.09.060.

[58] M.T. Myers, S. Charnvanichborikarn, C.C. Wei, Z.P. Luo, G.Q. Xie, S.O. Kucheyev, D.A. Lucca, L. Shao, Phase transition, segregation and nanopore formation in high-energy heavy-ion-irradiated metallic glass, Scr. Mater. 67 (2012) 887–890. https://doi.org/10.1016/j.scriptamat.2012.08.015.

[59] J. Carter, E.G. Fu, M. Martin, G. Xie, X. Zhang, Y.Q. Wang, D. Wijesundera, X.M. Wang, W.K. Chu, S.M. McDeavitt, L. Shao, Ion irradiation induced nanocrystal formation in amorphous Zr55Cu30Al10Ni5 alloy, Nucl. Instruments Methods Phys. Res. Sect. B Beam Interact. with Mater. Atoms. 267 (2009) 2827–2831. https://doi.org/10.1016/j.nimb.2009.05.068.

[60] V.M. Giordano, B. Ruta, Unveiling the structural arrangements responsible for the atomic dynamics in metallic glasses during physical aging, Nat. Commun. 7 (2016). https://doi.org/10.1038/ncomms10344.

[61] M. Fukuhara, A. Sanpei, High temperature-elastic moduli and internal dilational and shear frictions of fused quartz, Jpn. J. Appl. Phys. 33 (1994) 2890–2893. https://doi.org/10.1143/JJAP.33.2890/XML.

[62] C. Meade, R. Jeanloz, Frequency-dependent equation of state of fused silica to 10 GPa, Phys. Rev. B. 35 (1987).

[63] Y. Kikuchi, H. Sudo, N. Kuzuu, Thermal expansion of vitreous silica: Correspondence between dilatation curve and phase transitions in crystalline silica ARTICLES YOU MAY BE INTERESTED IN, J. Appl. Phys. 82 (1997) 4121. https://doi.org/10.1063/1.366279.

[64] L. Huang, J. Kieffer, Amorphous-amorphous transitions in silica glass. I. Reversible transitions and thermomechanical anomalies, Phys. Rev. B - Condens. Matter Mater. Phys. 69 (2004). https://doi.org/10.1103/PhysRevB.69.224203.

[65] K. Trachenko, M.T. Dove, Densification of silica glass under pressure, J. Phys. Condens. Matter. 14 (2002) 7449–7459. https://doi.org/10.1088/0953-8984/14/32/304.

[66] C. Meade, R.J. Hemley, H.K. Mao, High-pressure x-ray diffraction of SiO2 glass, Phys. Rev. Lett. 69 (1992) 1387–1390. https://doi.org/10.1103/PhysRevLett.69.1387.

[67] A. Perriot, D. Vandembroucq, E. Barthel, V. Martinez, L. Grosvalet, C.H. Martinet, B. Champagnon, Raman Microspectroscopic Characterization of Amorphous Silica Plastic Behavior, J. Am. Ceram. Soc. 89 (2006) 596–601. https://doi.org/10.1111/J.1551-2916.2005.00747.X.

[68] R. Guido, D. Valle, E. Venuti, High-pressure densification of silica glass: A molecular-dynamics simulation, (1996).

[69] S. Takashima, Z. Li, T.P. Chow, Metal-oxide-semiconductor interface and dielectric properties of atomic layer deposited SiO2 on GaN, Jpn. J. Appl. Phys. 52 (2013) 08JN24. https://doi.org/10.7567/JJAP.52.08JN24/XML.

[70] M. Mazur, D. Wojcieszak, J. Domaradzki, D. Kaczmarek, S. Song, F. Placido, TiO2/SiO2 multilayer as an antireflective and protective coating deposited by microwave assisted magnetron sputtering, Opto-Electronics Rev. 21 (2013) 233–238. https://doi.org/10.2478/S11772-013-0085-7/MACHINEREADABLECITATION/RIS.

[71] H.K. Raut, A.S. Nair, S.S. Dinachali, V.A. Ganesh, T.M. Walsh, S. Ramakrishna, Porous SiO2 anti-reflective coatings on large-area substrates by electrospinning and their application to solar modules, Sol. Energy Mater. Sol. Cells. 111 (2013) 9–15. https://doi.org/10.1016/J.SOLMAT.2012.12.023.

[72] K.H. Nielsen, D.K. Orzol, S. Koynov, S. Carney, E. Hultstein, L. Wondraczek, Large area, low cost anti-reflective coating for solar glasses, Sol. Energy Mater. Sol. Cells. 128 (2014) 283–288. https://doi.org/10.1016/J.SOLMAT.2014.05.034.

[73] H. Jeong, J. Cho, Fabrication and evaluation of protective SiOx layers using plasma-enhanced chemical vapor deposition, Surf. Coatings Technol. 330 (2017) 71–76. https://doi.org/10.1016/J.SURFCOAT.2017.09.074.

[74] L. Šimurka, R. Čtvrtlík, J. Tomaštík, G. Bektaş, J. Svoboda, K. Bange, Mechanical and optical properties of SiO2 thin films deposited on glass, Chem. Pap. 72 (2018) 2143–2151. https://doi.org/10.1007/s11696-018-0420-z.

[75] L. Berthier, P. Charbonneau, E. Flenner, F. Zamponi, Origin of Ultrastability in Vapor-Deposited Glasses, Phys. Rev. Lett. 119 (2017) 188002. https://doi.org/10.1103/PHYSREVLETT.119.188002/FIGURES/5/MEDIUM.

[76] C. Tangpatjaroen, K. Bagchi, R.A. Martínez, D. Grierson, I. Szlufarska, Mechanical Properties of Structure-Tunable, Vapor-Deposited TPD Glass, J. Phys. Chem. C. 122 (2018). https://doi.org/10.1021/acs.jpcc.8b09718.

[77] G. Greczynski, I. Petrov, J.E. Greene, Al capping layers for nondestructive x-ray photoelectron spectroscopy analyses of transition-metal nitride thin films, J. Vac. Sci. Technol. A. 33 (2015) 5–101. https://doi.org/10.1116/1.4916239.

[78] Y.C. Jean, J. David, V. Horn, W.-S. Hung, K.-R. Lee, Perspective of Positron Annihilation Spectroscopy in Polymers, (2013). https://doi.org/10.1021/ma401309x.

[79] J.N. Sun, Y.F. Hu, W.E. Frieze, D.W. Gidley, Characterizing porosity in nanoporous thin films using positronium annihilation lifetime spectroscopy, Radiat. Phys. Chem. 68 (2003) 345–349. https://doi.org/10.1016/S0969-806X(03)00182-8.

[80] H.G. Peng, R.S. Vallery, M. Liu, M. Skalsey, D.W. Gidley, Depth-profiled positronium annihilation lifetime spectroscopy on porous films, Colloids Surfaces A Physicochem. Eng. Asp. 300 (2007) 154–161. https://doi.org/10.1016/J.COLSURFA.2006.10.072.

[81] Y.Y. Wang, H. Nakanishi, Y.C. Jean, T.C. Sandreczki, Positron annihilation in amine-cured epoxy polymers—pressure dependence, J. Polym. Sci. Part B Polym. Phys. 28 (1990) 1431–1441. https://doi.org/10.1002/POLB.1990.090280902.

[82] R.B. Gregory, Y. Zhu, Analysis of positron annihilation lifetime data by numerical laplace inversion with the program CONTIN, Nucl. Instruments Methods Phys. Res. Sect. A Accel. Spectrometers, Detect. Assoc. Equip. 290 (1990) 172–182. https://doi.org/10.1016/0168-9002(90)90358-D.

[83] D.W. Gidley, W.E. Frieze, T.L. Dull, J. Sun, A.F. Yee, C. V. Nguyen, D.Y. Yoon, Determination of pore-size distribution in low-dielectric thin films, Appl. Phys. Lett. 76 (2000) 1282. https://doi.org/10.1063/1.126009.

[84] X. Liu, R.O. Pohl, Low-energy excitations in amorphous films of silicon and germanium, (1998).

[85] X. Liu, M.R. Abernathy, T.H. Metcalf, B. Jugdersuren, J.C. Culbertson, M. Molina-Ruiz, F. Hellman, Comparing amorphous silicon prepared by electron-beam evaporation and sputtering toward eliminating atomic tunneling states, J. Alloys Compd. 855 (2021) 157431. https://doi.org/10.1016/J.JALLCOM.2020.157431.

[86] F. Ebrahem, F. Bamer, B. Markert, The influence of the network topology on the deformation and fracture behaviour of silica glass: A molecular dynamics study, Comput. Mater. Sci. 149 (2018) 162–169. https://doi.org/10.1016/j.commatsci.2018.03.017.

[87] A. Nakano, R.K. Kalia, P. Vashishta, First sharp diffraction peak and intermediate-range order in amorphous silica: finite-size effects in molecular dynamics simulations, J. Non. Cryst. Solids. 171 (1994) 157–163. https://doi.org/10.1016/0022-3093(94)90351-4.

[88] J.P. Rino, I. Ebbsjo, R.K. Kalia, A. Nakano, P. Vashishta, Structure of rings in vitreous SiO2, Phys. Rev. B. 47 (1993).

[89] P. Vashishta, R.K. Kalia, A. Nakano, Large-scale atomistic simulations of dynamic fracture, Comput. Sci. Eng. 1 (1999) 56–65. https://doi.org/10.1109/5992.790588.

[90] C.L. Rountree, S. Prades, D. Bonamy, E. Bouchaud, R. Kalia, C. Guillot, A unified study of crack propagation in amorphous silica: Using experiments and simulations, J. Alloys Compd. 434–435 (2007) 60–63. https://doi.org/10.1016/J.JALLCOM.2006.08.336.

[91] P. Koziatek, J.L. Barrat, D. Rodney, Short- and medium-range orders in as-quenched and deformed SiO2 glasses: An atomistic study, J. Non. Cryst. Solids. 414 (2015) 7–15. https://doi.org/10.1016/J.JNONCRYSOL.2015.01.009.

[92] Q. Zhou, Y. Shi, B. Deng, J. Neuefeind, M. Bauchy, Experimental method to quantify the ring size distribution in silicate glasses and simulation validation thereof, Sci. Adv. 7 (2021). https://doi.org/10.1126/SCIADV.ABH1761/ASSET/EE6245B1-9AED-41BC-87EF-F15E299E1283/ASSETS/GRAPHIC/ABH1761-F9.JPEG.

[93] Y. Shi, J. Neuefeind, D. Ma, K. Page, L.A. Lamberson, N.J. Smith, A. Tandia, A.P. Song, Ring size distribution in silicate glasses revealed by neutron scattering first sharp diffraction peak analysis, J. Non. Cryst. Solids. 516 (2019) 71–81. https://doi.org/10.1016/J.JNONCRYSOL.2019.03.037.

[94] M. Zanatta, G. Baldi, R.S. Brusa, W. Egger, A. Fontana, E. Gilioli, S. Mariazzi, G. Monaco, L. Ravelli, F. Sacchetti, Structural Evolution and Medium Range Order in Permanently Densified Vitreous SiO 2, (2014). https://doi.org/10.1103/PhysRevLett.112.045501.

[95] N.P. Bansal, R.H. Doremus, Handbook of Glass Properties, Handb. Glas. Prop. (2013) 1–680. https://doi.org/10.1016/C2009-0-21785-5.

[96] M. Ono, K. Hara, M. Fujinami, S. Ito, Void structure in silica glass with different fictive temperatures observed with positron annihilation lifetime spectroscopy, Appl. Phys. Lett. 101 (2012) 164103. https://doi.org/10.1063/1.4761982.

[97] A.E. Geissberger, F.L. Galeener, Raman studies of vitreous SiO2 versus fictive temperature, Phys. Rev. B. 28 (1983) 3266. https://doi.org/10.1103/PhysRevB.28.3266.

[98] T. Deschamps, J. Margueritat, C. Martinet, A. Mermet, B. Champagnon, Elastic Moduli of Permanently Densified Silica Glasses, Sci. Reports 2014 41. 4 (2014) 1–7. https://doi.org/10.1038/srep07193.

[99] S. Takada, N. Hata, Y. Seino, N. Fujii, T. Kikkawa, Dependences of Young's modulus of porous

silica low dielectric constant films on skeletal structure and porosity, J. Appl. Phys. 100 (2006) 123512. https://doi.org/10.1063/1.2401660.

[100] T. Rouxel, H. Ji, J.P. Guin, F. Augereau, B. Ruffĺ, Indentation deformation mechanism in glass: Densification versus shear flow, J. Appl. Phys. 107 (2010) 094903. https://doi.org/10.1063/1.3407559.

[101] S. Le Roux, P. Jund, Ring statistics analysis of topological networks: New approach and application to amorphous GeS2 and SiO2 systems, Comput. Mater. Sci. 49 (2010) 70–83. https://doi.org/10.1016/J.COMMATSCI.2010.04.023.

[102] Y. Li, A. Annamareddy, D. Morgan, Z. Yu, B. Wang, C. Cao, J.H. Perepezko, M.D. Ediger, P.M. Voyles, L. Yu, Surface Diffusion Is Controlled by Bulk Fragility across All Glass Types, (2022). https://doi.org/10.1103/PhysRevLett.128.075501.

[103] L. Yang, G. Vajente, M. Fazio, A. Ananyeva, G.L. Billingsley, A. Markosyan, R. Bassiri, K. Prasai, M.M. Fejer, M. Chicoine, F. Schiettekatte, C.S. Menoni, Enhanced medium-range order in vapor-deposited germania glasses at elevated temperatures, Sci. Adv. 7 (2021). https://doi.org/10.1126/sciadv.abh1117.

[104] C.A. Schuh, T.C. Hufnagel, U. Ramamurty, Mechanical behavior of amorphous alloys, Acta Mater. 55 (2007) 4067–4109. https://doi.org/10.1016/j.actamat.2007.01.052.

[105] D.C. Hofmann, Bulk Metallic Glasses and Their Composites: A Brief History of Diverging Fields, J. Mater. 2013 (2013) 1–8. https://doi.org/10.1155/2013/517904.

[106] N. Chen, L. Martin, D. V. Luzguine-Luzgin, A. Inoue, Role of Alloying Additions in Glass Formation and Properties of Bulk Metallic Glasses, Materials (Basel). 3 (2010) 5320–5339. https://doi.org/10.3390/ma3125320.

[107] J. Kong, D.S. Xiong, Q.X. Yuan, Z.T. Ye, Strengthening bulk metallic glasses with minor alloying additions, Trans. Nonferrous Met. Soc. China (English Ed. 16 (2006) s598–s602. https://doi.org/10.1016/S1003-6326(06)60263-X.

[108] Y.Q. Cheng, A.J. Cao, H.W. Sheng, E. Ma, Local order influences initiation of plastic flow in metallic glass: Effects of alloy composition and sample cooling history, Acta Mater. 56 (2008) 5263–5275. https://doi.org/10.1016/J.ACTAMAT.2008.07.011.

[109] J.L. Zhang, Y.M. Wang, J.X. Lu, C.H. Shek, Q. Wang, C. Dong, Formation and mechanical properties of minor-Sb alloyed Ni8Nb5 bulk metallic glasses, J. Alloys Compd. 491 (2010) 513–516. https://doi.org/10.1016/j.jallcom.2009.10.259.

[110] Z.B. Jiao, H.X. Li, J.E. Gao, Y. Wu, Z.P. Lu, Effects of alloying elements on glass formation, mechanical and soft-magnetic properties of Fe-based metallic glasses, Intermetallics. 19 (2011) 1502–1508. https://doi.org/10.1016/j.intermet.2011.05.020.

[111] L. Deng, B. Zhou, H. Yang, X. Jiang, B. Jiang, X. Zhang, Roles of minor rare-earth elements addition in formation and properties of Cu-Zr-Al bulk metallic glasses, J. Alloys Compd. 632 (2015) 429–434. https://doi.org/10.1016/j.jallcom.2015.01.036.

[112] N. Chen, D. V. Louzguine-Luzgin, G.Q. Xie, T. Wada, A. Inoue, Influence of minor Si addition on the glass-forming ability and mechanical properties of Pd40Ni40P20 alloy, Acta Mater. 57 (2009) 2775–2780. https://doi.org/10.1016/j.actamat.2009.02.028.

[113] L.Y. Chen, Z.D. Fu, G.Q. Zhang, X.P. Hao, Q.K. Jiang, X.D. Wang, Q.P. Cao, H. Franz, Y.G. Liu, H.S. Xie, S.L. Zhang, B.Y. Wang, Y.W. Zeng, J.Z. Jiang, New class of plastic bulk metallic glass, Phys. Rev. Lett. 100 (2008) 075501. https://doi.org/10.1103/PhysRevLett.100.075501.

[114] N. Nollmann, I. Binkowski, V. Schmidt, H. Rösner, G. Wilde, Impact of micro-alloying on the plasticity of Pd-based bulk metallic glasses, Scr. Mater. 111 (2016) 119–122.

https://doi.org/10.1016/j.scriptamat.2015.08.030.

[115] B.J. Yang, J.H. Yao, J. Zhang, H.W. Yang, J.Q. Wang, E. Ma, Al-rich bulk metallic glasses with plasticity and ultrahigh specific strength, Scr. Mater. 61 (2009) 423–426. https://doi.org/10.1016/j.scriptamat.2009.04.035.

[116] M.L. Falk, J.S. Langer, Dynamics of viscoplastic deformation in amorphous solids, Phys. Rev. E. 57 (1998) 7192–7205. https://doi.org/10.1103/PhysRevE.57.7192.

[117] S. Ogata, F. Shimizu, J. Li, M. Wakeda, Y. Shibutani, Atomistic simulation of shear localization in Cu-Zr bulk metallic glass, Intermetallics. 14 (2006) 1033–1037. https://doi.org/10.1016/j.intermet.2006.01.022.

[118] Y. Shi, M.L. Falk, Does metallic glass have a backbone? The role of percolating short range order in strength and failure, Scr. Mater. 54 (2006) 381–386. https://doi.org/10.1016/J.SCRIPTAMAT.2005.09.053.

[119] M. Wakeda, Y. Shibutani, S. Ogata, J. Park, Relationship between local geometrical factors and mechanical properties for Cu-Zr amorphous alloys, Intermetallics. 15 (2007) 139–144. https://doi.org/10.1016/j.intermet.2006.04.002.

[120] G.B. Bokas, A.E. Lagogianni, G.A. Almyras, C.E. Lekka, D.G. Papageorgiou, G.A. Evangelakis, On the role of Icosahedral-like clusters in the solidification and the mechanical response of Cu–Zr metallic glasses by Molecular Dynamics simulations and Density Functional Theory computations, Intermetallics. 43 (2013) 138–141. https://doi.org/10.1016/J.INTERMET.2013.07.022.

[121] K.W. Park, J. il Jang, M. Wakeda, Y. Shibutani, J.C. Lee, Atomic packing density and its influence on the properties of Cu-Zr amorphous alloys, Scr. Mater. 57 (2007) 805–808. https://doi.org/10.1016/j.scriptamat.2007.07.019.

[122] Y.Q. Cheng, H.W. Sheng, E. Ma, Relationship between structure, dynamics, and mechanical properties in metallic glass-forming alloys, Phys. Rev. B. 78 (2008) 014207. https://doi.org/10.1103/PhysRevB.78.014207.

[123] A.J. Cao, Y.Q. Cheng, E. Ma, Structural processes that initiate shear localization in metallic glass, Acta Mater. 57 (2009) 5146–5155. https://doi.org/10.1016/J.ACTAMAT.2009.07.016.

[124] Y.Q. Cheng, A.J. Cao, E. Ma, Correlation between the elastic modulus and the intrinsic plastic behavior of metallic glasses: The roles of atomic configuration and alloy composition, Acta Mater. 57 (2009) 3253–3267. https://doi.org/10.1016/j.actamat.2009.03.027.

[125] M. Wakeda, Y. Shibutani, Icosahedral clustering with medium-range order and local elastic properties of amorphous metals, Acta Mater. 58 (2010) 3963–3969. https://doi.org/10.1016/j.actamat.2010.03.029.

[126] M. Lee, C.-M. Lee, K.-R. Lee, E. Ma, J.-C. Lee, Networked interpenetrating connections of icosahedra: Effects on shear transformations in metallic glass, Acta Mater. 59 (2011) 159–170. https://doi.org/10.1016/J.ACTAMAT.2010.09.020.

[127] J. Ding, Y.Q. Cheng, E. Ma, Correlating local structure with inhomogeneous elastic deformation in a metallic glass, Appl. Phys. Lett. 101 (2012) 121917. https://doi.org/10.1063/1.4754121.

[128] Y.Q. Cheng, J. Ding, E. Ma, Local Topology *vs.* Atomic-Level Stresses as a Measure of Disorder: Correlating Structural Indicators for Metallic Glasses, Mater. Res. Lett. 1 (2013) 3–12. https://doi.org/10.1080/21663831.2012.722759.

[129] J. Ding, S. Patinet, M.L. Falk, Y. Cheng, E. Ma, Soft spots and their structural signature in a metallic glass., Proc. Natl. Acad. Sci. U. S. A. 111 (2014) 14052–6. https://doi.org/10.1073/pnas.1412095111.

[130] J. Ding, Y.-Q. Cheng, H. Sheng, M. Asta, R.O. Ritchie, E. Ma, Universal structural parameter to

quantitatively predict metallic glass properties, Nat. Commun. 7 (2016) 13733. https://doi.org/10.1038/ncomms13733.

[131] Q. An, K. Samwer, M.D. Demetriou, M.C. Floyd, D.O. Duggins, W.L. Johnson, W.A.G. Iii, How the toughness in metallic glasses depends on topological and chemical heterogeneity, Proc. Natl. Acad. Sci. U. S. A. 113 (2016) 7053–7058. https://doi.org/10.1073/pnas.1607506113.

[132] W. Yang, H. Liu, Y. Zhao, A. Inoue, K. Jiang, J. Huo, H. Ling, Q. Li, B. Shen, Mechanical properties and structural features of novel fe-based bulk metallic glasses with unprecedented plasticity, Sci. Rep. 4 (2014) 1–6. https://doi.org/10.1038/srep06233.

[133] F. Moitzi, D. Şopu, D. Holec, D. Perera, N. Mousseau, J. Eckert, Chemical bonding effects on the brittle-to-ductile transition in metallic glasses, Acta Mater. 188 (2020) 273–281. https://doi.org/10.1016/j.actamat.2020.02.002.

[134] Y. He, G.. Shiflet, S.. Poon, Synthesis and properties of aluminum-based metallic glasses containing rare earths, J. Alloys Compd. 207–208 (1994) 349–354. https://doi.org/10.1016/0925-8388(94)90238-0.

[135] A. Inoue, H. Kimura, Fabrications and mechanical properties of bulk amorphous, nanocrystalline, nanoquasicrystalline alloys in aluminum-based system, J. Light Met. 1 (2001) 31–41. https://doi.org/10.1016/S1471-5317(00)00004-3.

[136] S.D. Zhang, Z.W. Liu, Z.M. Wang, J.Q. Wang, In situ EC-AFM study of the effect of nanocrystals on the passivation and pit initiation in an Al-based metallic glass, Corros. Sci. 83 (2014) 111–123. https://doi.org/10.1016/j.corsci.2014.02.005.

[137] M. Gao, J.H. Perepezko, Al-Based Amorphous Metallic Plastics, Adv. Eng. Mater. 21 (2019) 1800930. https://doi.org/10.1002/adem.201800930.

[138] J. Henao, A. Concustell, I. G.Cano, S. Dosta, N. Cinca, J.M. Guilemany, T. Suhonen, Novel Al-based metallic glass coatings by Cold Gas Spray, Mater. Des. 94 (2016) 253–261. https://doi.org/10.1016/J.MATDES.2016.01.040.

[139] K.G. Prashanth, S. Kumar, S. Scudino, B.S. Murty, J. Eckert, Fabrication and response of Al70Y16Ni 10Co4 glass reinforced metal matrix composites, Mater. Manuf. Process. 26 (2011) 1242–1247. https://doi.org/10.1080/10426914.2010.544824.

[140] W. Zalewski, J. Antonowicz, R. Bacewicz, J. Latuch, Local atomic order in Al-based metallic glasses studied using XAFS method, J. Alloys Compd. 468 (2009) 40–46. https://doi.org/10.1016/j.jallcom.2008.01.037.

[141] Y.E. Kalay, L.S. Chumbley, M.J. Kramer, I.E. Anderson, Local structure in marginal glass forming Al–Sm alloy, Intermetallics. 18 (2010) 1676–1682. https://doi.org/10.1016/J.INTERMET.2010.05.005.

[142] G.B. Bokas, L. Zhao, J.H. Perepezko, I. Szlufarska, On the role of Sm in solidification of Al-Sm metallic glasses, Scr. Mater. 124 (2016) 99–102. https://doi.org/10.1016/j.scriptamat.2016.06.045.

[143] Y. Shen, J.H. Perepezko, Al-based amorphous alloys: Glass-forming ability, crystallization behavior and effects of minor alloying additions, J. Alloys Compd. (2017). https://doi.org/10.1016/j.jallcom.2016.11.079.

[144] A. Stukowski, Visualization and analysis of atomistic simulation data with OVITO-the Open Visualization Tool, Model. Simul. Mater. Sci. Eng. 18 (2010). https://doi.org/10.1088/0965-0393/18/1/015012.

[145] G. Kresse, J. Furthmüller, Efficient iterative schemes for ab initio total-energy calculations using a plane-wave basis set, Phys. Rev. B - Condens. Matter Mater. Phys. 54 (1996) 11169–11186. https://doi.org/10.1103/PhysRevB.54.11169.

[146] D. Joubert, From ultrasoft pseudopotentials to the projector augmented-wave method, Phys. Rev. B - Condens. Matter Mater. Phys. 59 (1999) 1758–1775. https://doi.org/10.1103/PhysRevB.59.1758.

[147] J.P. Perdew, K. Burke, M. Ernzerhof, Generalized gradient approximation made simple, Phys. Rev. Lett. 77 (1996) 3865–3868. https://doi.org/10.1103/PhysRevLett.77.3865.

[148] J. Xi, G. Bokas, L.E. Schultz, M. Gao, L. Zhao, Y. Shen, J.H. Perepezko, D. Morgan, I. Szlufarska, Microalloying effect in ternary Al-Sm-X (X = Ag, Au, Cu) metallic glasses studied by ab initio molecular dynamics, Comput. Mater. Sci. 185 (2020) 109958. https://doi.org/10.1016/j.commatsci.2020.109958.

[149] S.K. Saxena, Pressure-volume equation of state for solids, in: J. Phys. Chem. Solids, Pergamon, 2004: pp. 1561–1563. https://doi.org/10.1016/j.jpcs.2004.02.003.

[150] X. Li, B. Bhushan, A review of nanoindentation continuous stiffness measurement technique and its applications, Mater. Charact. 48 (2002) 11–36. https://doi.org/10.1016/S1044-5803(02)00192-4.

[151] T. Egami, The atomic structure of aluminum based metallic glasses and universal criterion for glass formation, J. Non. Cryst. Solids. 205–207 (1996) 575–582. https://doi.org/10.1016/S0022-3093(96)00277-3.

[152] K. Maiti, D. Sarma, Electronic structure and conductivity in a model approximant of the icosahedral quasicrystal Al-Cu-Fe, Phys. Rev. B - Condens. Matter Mater. Phys. 54 (1996) 7816–7822. https://doi.org/10.1103/PhysRevB.54.7816.

[153] E. Belin-Ferré, V. Fournée, J.M. Dubois, Al 3p occupied states in Al-Cu-Fe intermetallics and enhanced stability of the icosahedral quasicrystal, J. Phys. Condens. Matter. 12 (2000) 8159–8177. https://doi.org/10.1088/0953-8984/12/37/314.

[154] H.W. Sheng, Y.Q. Cheng, P.L. Lee, S.D. Shastri, E. Ma, Atomic packing in multicomponent aluminum-based metallic glasses, Acta Mater. 56 (2008) 6264–6272. https://doi.org/10.1016/J.ACTAMAT.2008.08.049.

[155] A.F.Wells, Structural Inorganic Chemistry, Clarendon Press. Oxford. 5th ed (1984) 1288.

[156] E. Ma, J. Ding, Tailoring structural inhomogeneities in metallic glasses to enable tensile ductility at room temperature, Mater. Today. 19 (2016) 568–579. https://doi.org/10.1016/j.mattod.2016.04.001.

[157] K. Liang, X. Zhang, J. Qiao, S. Pan, S. Feng, Effects of minor addition of Al and Ag elements on the atomic structure and mechanical property of ZrCu-based metallic glasses, J. Non. Cryst. Solids. 550 (2020) 120385. https://doi.org/10.1016/J.JNONCRYSOL.2020.120385.

[158] L.S. Luo, B.B. Wang, F.Y. Dong, Y.Q. Su, E.Y. Guo, Y.J. Xu, M.Y. Wang, L. Wang, J.X. Yu, R.O. Ritchie, J.J. Guo, H.Z. Fu, Structural origins for the generation of strength, ductility and toughness in bulk-metallic glasses using hydrogen microalloying, Acta Mater. 171 (2019) 216–230. https://doi.org/10.1016/J.ACTAMAT.2019.04.022.

[159] N. Nollmann, I. Binkowski, V. Schmidt, H. Rösner, G. Wilde, Impact of micro-alloying on the plasticity of Pd-based bulk metallic glasses, Scr. Mater. 111 (2016) 119–122. https://doi.org/10.1016/J.SCRIPTAMAT.2015.08.030.

[160] Y. Wu, D. Cao, Y. Yao, G. Zhang, J. Wang, L. Liu, F. Li, H. Fan, X. Liu, H. Wang, X. Wang, H. Zhu, S. Jiang, P. Kontis, D. Raabe, B. Gault, Z. Lu, Substantially enhanced plasticity of bulk metallic glasses by densifying local atomic packing, Nat. Commun. 12 (2021) 1–9. https://doi.org/10.1038/s41467-021-26858-9.

[161] D. Şopu, F. Moitzi, N. Mousseau, J. Eckert, An atomic-level perspective of shear band formation and interaction in monolithic metallic glasses, Appl. Mater. Today. 21 (2020) 100828.

https://doi.org/10.1016/j.apmt.2020.100828.

[162] F. Zhu, S. Song, K.M. Reddy, A. Hirata, M. Chen, Spatial heterogeneity as the structure feature for structure–property relationship of metallic glasses, Nat. Commun. 2018 91. 9 (2018) 1–7. https://doi.org/10.1038/s41467-018-06476-8.

[163] N. Wang, J. Ding, F. Yan, M. Asta, R.O. Ritchie, L. Li, Spatial correlation of elastic heterogeneity tunes the deformation behavior of metallic glasses, Npj Comput. Mater. 4 (2018) 1–10. https://doi.org/10.1038/s41524-018-0077-8.

[164] N. Wang, J. Ding, P. Luo, Y. Liu, L. Li, F. Yan, Chemical variation induced nanoscale spatial heterogeneity in metallic glasses, Mater. Res. Lett. 6 (2018) 655–661. https://doi.org/10.1080/21663831.2018.1532465.

[165] S. Hilke, H. Rösner, G. Wilde, The role of minor alloying in the plasticity of bulk metallic glasses, Scr. Mater. 188 (2020) 50–53. https://doi.org/10.1016/J.SCRIPTAMAT.2020.06.070.

[166] Y.Q. Cheng, E. Ma, H.W. Sheng, Atomic Level Structure in Multicomponent Bulk Metallic Glass, Phys. Rev. Lett. 102 (2009) 245501. https://doi.org/10.1103/PhysRevLett.102.245501.

[167] H.-K. Kim, J.-P. Ahn, B.-J. Lee, K.-W. Park, J.-C. Lee, Role of atomic-scale chemical heterogeneities in improving the plasticity of Cu-Zr-Ag bulk amorphous alloys, Acta Mater. 157 (2018) 209–217. https://doi.org/10.1016/j.actamat.2018.07.040.

[168] H. Bin Yu, R. Richert, K. Samwer, Structural rearrangements governing Johari-Goldstein relaxations in metallic glasses, Sci. Adv. 3 (2017). https://doi.org/10.1126/sciadv.1701577.

[169] B.A. Sun, W.H. Wang, The fracture of bulk metallic glasses, Prog. Mater. Sci. 74 (2015) 211–307. https://doi.org/10.1016/j.pmatsci.2015.05.002.

[170] Q. Wang, J.J. Liu, Y.F. Ye, T.T. Liu, S. Wang, C.T. Liu, J. Lu, Y. Yang, Universal secondary relaxation and unusual brittle-to-ductile transition in metallic glasses, Mater. Today. 20 (2017) 293–300. https://doi.org/10.1016/j.mattod.2017.05.007.